MEASUREMENT OF INCLUSIVE CHARM PRODUCTION IN TWO-PHOTON COLLISIONS AT LEP

A Dissertation

Submitted to the Graduate Faculty of the
Louisiana State University and
Agricultural and Mechanical College
in partial fulfillment of the
requirements for the degree of
Doctor of Philosophy

in

The Department of Physics and Astronomy

by
Alan L. Stone Jr.
B.A., Boston University, 1993
August, 1999

To my parents,

Al and Dolly Stone

ACKNOWLEDGEMENTS

I need to begin by expressing my appreciation and gratitude to my thesis advisor Professor Roger McNeil for giving me the opportunity to prove myself. He provided me with the direction that I needed, and always challenged me to not only understand what I was doing but why I was doing it.

I would like to thank Professor Richard Imlay for my introduction into experimental particle physics, and Professor Bill Metcalf who indoctrinated me into the computing aspect of physics analysis, teaching me the basics of fortran, PAW and HBOOK. I am very grateful to Professor Mike Cherry for bringing me to LSU and for giving me a second chance.

My experience at CERN as part of the L3 Collaboration was very rewarding, in a large part due to Valery Andreev. I cannot thank him enough for his guidance and incredible patience which shaped me into a real physicist.

My time at LSU would not have been as worthwhile or as much fun without my best man, Parker. He is a good friend, and I wish him success in all of his future endeavors.

I am very grateful to Maria and John for accepting me into the Two-Photon Group, and for their help and useful discussions. I want to thank Cristoph and Hoorani without whom I might still be struggling with my analysis code. My gratitude goes out to Hortensia for solving all my computer problems at LSU, and to Mehnaz who did the same at CERN. I would be at fault if I did not thank my fellow members of L3. Without a collabora-

tive effort, none of this data would be available. My colleagues provided a stimulating and friendly work environment.

I want to thank my parents for all their time, efforts and love that helped me reach this point. And, finally, to Isabel, for waiting, loving, supporting and sacrificing, *je t'aime.*

TABLE OF CONTENTS

ACKNOWLEDGMENTS iii

LIST OF TABLES vii

LIST OF FIGURES viii

ABSTRACT xii

CHAPTER
1 INTRODUCTION 1
1.1 Two-Photon Interactions 2
1.2 LEP Collider 8
1.3 Event Definition 10
1.4 Luminosity Measurement 11
1.5 Heavy Flavor Production 12

2 CHARM PRODUCTION IN TWO-PHOTON PHYSICS 17
2.1 Photon Generation 18
2.2 Photon Structure 20
2.3 Direct and Resolved Processes 24
2.4 Renormalization Scale and the Charm Mass 26

3 THE L3 EXPERIMENT 30
3.1 Time Expansion Chamber 36
3.2 Electromagnetic Calorimeter 38
3.3 Hadron Calorimeter 41
3.4 Muon Chamber 42
3.5 Luminosity Monitor 44

4 L3 DATA TRIGGERING, RECONSTRUCTION AND SIMULATION 48
4.1 L3 Trigger System 48
4.1.1 Level 1 Trigger 48
4.1.2 Level 2 Trigger 52
4.1.3 Level 3 Trigger 53
4.2 Event Reconstruction 53
4.2.1 Tracks 54
4.2.2 Bumps in the ECAL 54
4.2.3 Clusters in the HCAL 56
4.2.4 Muons 56
4.3 Monte Carlo Simulation 57
4.3.1 Event Generation 57
4.3.2 Detector Simulation 58
4.4 Monte Carlo Reconstruction 59

5 ANALYSIS 60
5.1 Hadronic Two-Photon Events Selection 61
5.2 Electron Tag 73
5.3 Muon Tag 93
5.4 Inclusive Lepton Cross Section 97
5.4.1 Inclusive Electron Cross Section 97
5.4.2 Inclusive Muon Cross Section 100

6 RESULTS 101
6.1 Total Inclusive Charm Cross Section 101
6.2 Direct and Resolved Contributions 109

7 SUMMARY AND OUTLOOK 114

BIBLIOGRAPHY 118

APPENDIX - SCINTILLATORS 122
A.1 Introduction 122
A.2 Barrel and Endcap Counters 122
A.3 Event Selection 124
A.4 Barrel Calibration 124
A.5 Endcap Calibration 128
A.6 Efficiency 131
A.7 Acknowledgements 139

THE L3 COLLABORATION 141

PUBLICATIONS 150

VITA 156

LIST OF TABLES

1.1 Quarks. The abbreviation of each quark type 2

3.1 Properties of a BGO crystal. 40

5.1 Hadronic cut selection 62

5.2 Hadronic two-photon event summary 73

5.3 Electron candidate cut selection 75

5.4 Summary of the electron tag analysis 89

5.5 Background from sources other than two-photon hadronic interactions for electron tag analysis 89

5.6 Muon candidate cut selection 93

5.7 Summary of the muon tag analysis 95

5.8 Background from sources other than two-photon hadronic interactions for muon tag analysis 95

5.9 Inclusive electron cross section 98

5.10 Inclusive muon cross section 100

6.1 Summary of the charm analysis by the electron tag 103

6.2 Summary of the charm analysis by the muon tag 103

6.3 Total cross section values for the process $e^+e^- \rightarrow e^+e^-c\bar{c}X$ at four different energies 104

6.4 Systematic errors for the inclusive charm cross section measurement by the electron tag 106

6.5 Systematic errors for the inclusive charm cross section measurement by the muon tag 106

7.1 Total cross section values for the process $e^+e^- \rightarrow e^+e^-c\bar{c}X$ at $\sqrt{s} = 189$ GeV 115

7.2 Total cross section values for the process $e^+e^- \rightarrow e^+e^-b\bar{b}X$ at $\sqrt{s} = 189$ GeV 116

LIST OF FIGURES

1.1 Quantum fluctuation of a photon into a pair of electrons . . . 3

1.2 Kinematics of a two-photon interaction 6

1.3 Theoretical cross sections for several physics processes at e^+e^- colliders 7

1.4 Above and below ground view of the LEP tunnel and its relation to the four LEP experiments 8

1.5 The exchange of a photon at small angles for Bhabha scattering 12

1.6 Diagrams contributing to charm production in two-photon collisions at LEP 14

1.7 The charm production cross section in two-photon collisions prior to the measurements made by L3 at LEP 16

2.1 The allowed phase space for hadronic two-photon processes . 22

2.2 Next-to-leading order diagrams contributing to charm production in two-photon collisions at LEP. 25

2.3 The charm cross section to NLO accuracy for direct and QCD prediction for a charm mass of 1.3 and 1.7 GeV 27

2.4 The uncertainty to the charm production prediction due to the change in the renormalization scale from m_C to $2m_C$ . . . 29

3.1 Diagram for a general detector for an electron-positron collider. 31

3.2 The L3 detector. 34

3.3 A side view of the L3 detector. 35

3.4 A perspective view of the TEC. 37

3.5 Wire configuration in one inner TEC sector and in part of two outer sectors 38

3.6 A side view of central part of the L3 detector 39

3.7 A BGO crystal 40

3.8 R-z view of the L3 hadron calorimeter 41

3.9 View of an octant of the muon detector with its five chambers 43

3.10 Sagitta of a muon track 44

3.11 View of the forward-backward muon spectrometer 45

3.12 A Bhabha event in the luminosity monitor 46

4.1 L3 online trigger system 49

5.1 Invariant visible mass in the data at a) $\sqrt{s} = 91$ GeV and at b) $\sqrt{s} = 130 - 140$ GeV 63

5.2 Invariant visible mass in the data at a) $\sqrt{s} = 161 - 172$ GeV and at b) $\sqrt{s} = 183$ GeV 64

5.3 Total visible energy in the data at a) $\sqrt{s} = 91$ GeV and at b) $\sqrt{s} = 130 - 140$ GeV 66

5.4 Total visible energy in the data at a) $\sqrt{s} = 161 - 172$ GeV and at b) $\sqrt{s} = 183$ GeV 67

5.5 Ratio of the energy of the most energetic cluster in the luminosity monitor to the beam energy in the data at a) $\sqrt{s} = 91$ GeV and at b) $\sqrt{s} = 130 - 140$ GeV 68

5.6 Ratio of the energy of the most energetic cluster in the luminosity monitor to the beam energy in the data at a) $\sqrt{s} = 161 - 172$ GeV and at b) $\sqrt{s} = 183$ GeV 69

5.7 Display of the transverse view of a two-photon muon event . . 71

5.8 Display of the longitudinal view of a two-photon muon event 72

5.9 Variable cut is chosen by eye 74

5.10 Momentum of the electrons at $\sqrt{s} = 183$ GeV 76

5.11 Matching of the azimuthal angle of the electron candidate track in the TEC to the shower in the BGO at a) $\sqrt{s} = 91$ GeV and b) $\sqrt{s} = 183$ GeV 78

5.12 A χ^2 test to identify a shower in the BGO as an EM cluster at a) $\sqrt{s} = 91$ GeV and b) $\sqrt{s} = 183$ GeV 79

5.13 The distance of closest approach (DCA) of a track to its reconstructed vertex in the tranverse plane at $\sqrt{s} = 91$ and 183 GeV. 81

5.14 The shower shape variable E_1/E_9 at $\sqrt{s} = 91$ and 183 GeV. . 82

5.15 The shower shape variable E_9/E_{25} at a) $\sqrt{s} = 91$ GeV and b) $\sqrt{s} = 183$ GeV 83

5.16 The ratio, E_t/p_t, of the transverse energy measured by the electromagnetic calorimeter and the transverse momentum of the track for a) $\sqrt{s} = 91$ GeV and b) $\sqrt{s} = 130 - 140$ GeV . . 85

5.17 The ratio, E_t/p_t, of the transverse energy measured by the electromagnetic calorimeter and the transverse momentum of the track for a) $\sqrt{s} = 161 - 172$ GeV and b) $\sqrt{s} = 183$ GeV . . 86

5.18 Display of the transverse view of a two-photon electron event 87

5.19 Display of the longitudinal view of a two-photon electron event 88

5.20 Track multiplicity for the final event sample in the data at a) $\sqrt{s} = 91$ GeV and at b) $\sqrt{s} = 183$ GeV 91

5.21 The final event distributions of a) the visible mass and b) the ratio of the most energetic luminosity cluster to the beam energy for the data at $\sqrt{s} = 183$ GeV 92

5.22 Polar angle distribution of the events at $\sqrt{s} = 183$ GeV selected with the muon tag 94

5.23 Track multiplicity for the final event sample selected by the muon tag in the data at $\sqrt{s} = 183$ GeV 96

5.24 The differential cross section for inclusive electrons at $\sqrt{s} = 183$ GeV as a function of the electron transverse momentum 99

6.1 The charm production cross section in two-photon collisions . 108

6.2 Distributions of a) the visible mass spectrum and b) the track multiplicity for the inclusive electron data at $\sqrt{s} = 183$ GeV . 110

6.3 Distributions of a) the transverse momentum and b) the polar angle for the inclusive electron data at $\sqrt{s} = 183$ 111

6.4 Energy flow as a function of pseudorapidity η 112

7.1 The charm and beauty production cross section in two-photon collisions at $\sqrt{s} = 189$ GeV 117

A.1 A perspective view of the L3 detector 123

A.2 The corrected time resolution for barrel counter 6 129

A.3 Average corrected time resolution in the barrel counters . . . 130

A.4 The corrected time resolution for endcap counter 14 132

A.5 Average corrected time resolution in the endcap counters . . . 133

A.6 Barrel counter efficiency for 1998 data 135

A.7 Efficiency of barrel counters 24 and 25 from 1995 through 1998 136

A.8 Efficiency of barrel counters 23 and 26 from 1995 through 1998 137

A.9 Corrected time distributions for (a) barrel counter 23 and (b) barrel counter 24 138

A.10 Endcap counter efficiency for 1998 data 140

ABSTRACT

The cross section of inclusive charm production in two-photon collisions $\sigma(e^+e^- \rightarrow e^+e^-c\bar{c}X)$ is measured at the Large Electron Positron (LEP) collider at the European Center for Nuclear and Particle Physics (CERN). The data was obtained with the L3 detector at the center-of-mass energy of 91 GeV (LEP1) and for the first time at the center-of-mass energies from 130-183 GeV (LEP2). Charmed hadrons are identified by electrons and muons from semileptonic decays. The measured cross section agrees with next-to-leading order (NLO) QCD calculations. The direct process $\gamma\gamma \rightarrow c\bar{c}$ is found to be insufficient to describe the data. The measured cross section values and event distributions require contributions from resolved processes, which are sensitive to the gluon density in the photon.

CHAPTER 1

INTRODUCTION

Current research in high energy particle physics follows in two directions. The search for new particles provides the motivation to build larger experiments at higher energies. However, the rate of discovery of new particles has decreased significantly over the past two decades, while the competition for data remains high as most particle physicists aspire to discover something new and exciting. The other direction is in what is called the "bread-and-butter physics". The measurement of known particles in terms of mass, lifetime, decay channels, rate of production, etc. are performed with better accuracy and at higher energies. These measurements extend the world knowledge, and the new information will go towards refining the theoretical models.

The main cornerstone to the study of particle physics is a good understanding of hadrons and their interactions. Hadrons are made up of smaller constituent partons called quarks and gluons. Quarks have mass and carry fractional electric charges (Table 1.1). There are six flavors of quarks: up (u), down (d), strange (s), charm (c), beauty (b) and top (t). Corresponding to each quark is an antiquark with an opposite charge. There are two types of quark combinations which form hadrons. A meson is made up of a quark-antiquark pair; a baryon is comprised of three quarks. In the latter case, at least two of the three charges will have equal signs which introduces an electromagnetic repulsion. Therefore, there must be a *strong* force which

binds the quarks into a hadron. This strong force interaction between quarks is mediated by a gluon which is a massless particle analagous to the massless photon in electromagnetic interactions. In addition, there is a strong charge, called *color*. A quark of a specific flavor comes in three colors; gluons come in eight colors. The net quark and gluon content in a hadron must have a zero color charge. The strong interactions between quarks and gluons is well described by the theory of Quantum Chromodynamics (QCD).

Table 1.1: Quarks. The abbreviation of each quark type is given by the first letter of their name. The mass is in units of GeV/c^2. The charge is a fraction of the electron charge, e.

Quark	Mass	Charge
up	0.002-0.008	+2/3
down	0.005-0.015	-1/3
strange	0.1-0.3	-1/3
charm	1.2-1.9	+2/3
beauty	4.5-4.9	-1/3
top	168-192	+2/3

The focus of this thesis is to study the production of charm quarks in two-photon interactions. The measurements from experiment are compared to the predictions of QCD.

1.1 Two-Photon Interactions

In the classical theory of electrodynamics, electromagnetic waves pass by each other without interacting. The photon is considered structureless, and two-photon scattering can not occur. This picture of the photon is different in quantum mechanics. Photons can materialize as pairs of electrons through an interaction with a Coulomb field. From the uncertainty principle

($\Delta t \approx 1/\Delta E$)[1], the lifetime of this intermediate state is given by:

$$\Delta t \approx \frac{2E_\gamma}{m^2_{pair}} \tag{1.1}$$

As the scale of available energies increase, Δt becomes larger, and photon-

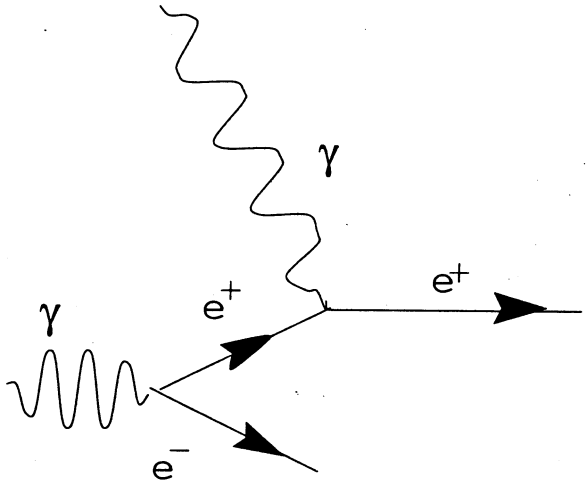

Figure 1.1: Quantum fluctuation of a photon into a pair of electrons. The other photon interacts with one of the electrons.

photon scattering becomes possible through the interaction of the intermediate particles (Figure 1.1). As the photon energies increase, high mass states can be produced including leptonic and hadronic final states revealing the structure of the photon.

The reaction, $\gamma\gamma \rightarrow X$, will produce two-photon final states of three different types.

1. Lepton pairs may be produced, $\gamma\gamma \rightarrow \ell^+\ell^-$, where ℓ = e, μ and τ. This reaction is a pure Quantum Electrodynamics (QED) process and exact Feynman diagram calculations can be made.

[1]The convention $c = \hbar = 1$ and $\frac{e^2}{4\pi} = \alpha = \frac{1}{137.05}$.

2. A photon has the same quantum numbers as a vector meson, so often a quantum fluctuation transforms a photon into a vector meson ($\rho, \omega, \phi, J/\Psi, \Upsilon$). Therefore, the photon can also be considered as an incoming hadron, interacting strongly through its quark and gluon constituents. This source of hadron interactions is described by the Vector Dominance Model (VDM) and is the largest contribution to $\gamma\gamma \rightarrow$ *hadrons*. Included in this is the production of meson resonances of positive charge conjugation such as η, $\eta\prime$ and A_2.

3. Through hard scattering, the two photons can interact directly to produce a quark-antiquark pair ($\gamma\gamma \rightarrow q\bar{q}$). Also, one of the photons (target) can resolve into quarks and gluons, and the other photon (probe) will interact with a resolved gluon to produce a quark-antiquark pair ($\gamma g \rightarrow q\bar{q}$). The final state quarks become jets of hadrons. Although the hard scattering processes make a smaller contribution to the overall $\gamma\gamma \rightarrow$ *hadrons* cross section, they are the primary source of heavy flavor (charm, beauty) quarks.

The potential between a $q\bar{q}$ pair can be expressed as

$$V = -\frac{\kappa}{r} + kr \tag{1.2}$$

where the first term arises from single gluon exchange and dominates at small distances, r. The second term is associated with confinement. As a quark-antiquark pair separate, the lines of force of the color field are pulled together by a strong gluon interaction, forming what is called a *string*. As the $q\bar{q}$ pair separate, stretching the string, the potential energy, kr, increases

until it is more favorable to create a new $q\bar{q}$ pair. The quark and antiquark continue on their way, with smaller kinetic energy, further stretching the lines of force. This stretching and breaking of strings to form new $q\bar{q}$ pairs is called *fragmentation.* The string fragmentation continues until all of the kinetic energy has been converted into clusters of quarks and gluons, where each cluster has zero net color. The strong color coupling turns the quarks and gluons into hadrons, forming two jets of particles in the directions of the original quark and antiquark.

Two-photon interactions, $e^+e^- \rightarrow e^+e^-\gamma\gamma$, are easily studied at high energy e^+e^- colliders. The collision of an electron and positron, each with the same mass, is viewed in a Lorentz frame in which they collide with momenta equal in magnitude but opposite in direction. The total energy of the system in this *center-of-mass* frame is called the center-of-mass energy which is commonly denoted by $\sqrt{s} = 2\,E_{Beam}$. As the beams of electrons and positrons circulate and interact with the Coulomb field of the other charged particle, large numbers of bremsstrahlung photons are radiated, usually at very small angles with respect to the beam direction. The basic diagram of a two-photon reaction at e^+e^- colliders in shown in Figure 1.2. A radiated photon from each incoming electron[2] will interact, producing a final state X with an invariant mass $W_{\gamma\gamma}$. The two-photon invariant mass is defined as

$$W_{\gamma\gamma} = \sqrt{(\mathbf{q_1} + \mathbf{q_2})^2} = \sqrt{(\sum_x E_x)^2 - (\sum_x \vec{p}_x)^2}, \qquad (1.3)$$

where the energies and momentums are summed over all particles in the final state X. The energy spectrum of bremsstrahlung photons is proportional to

[2]The term *electron* will be used for both electrons and positrons.

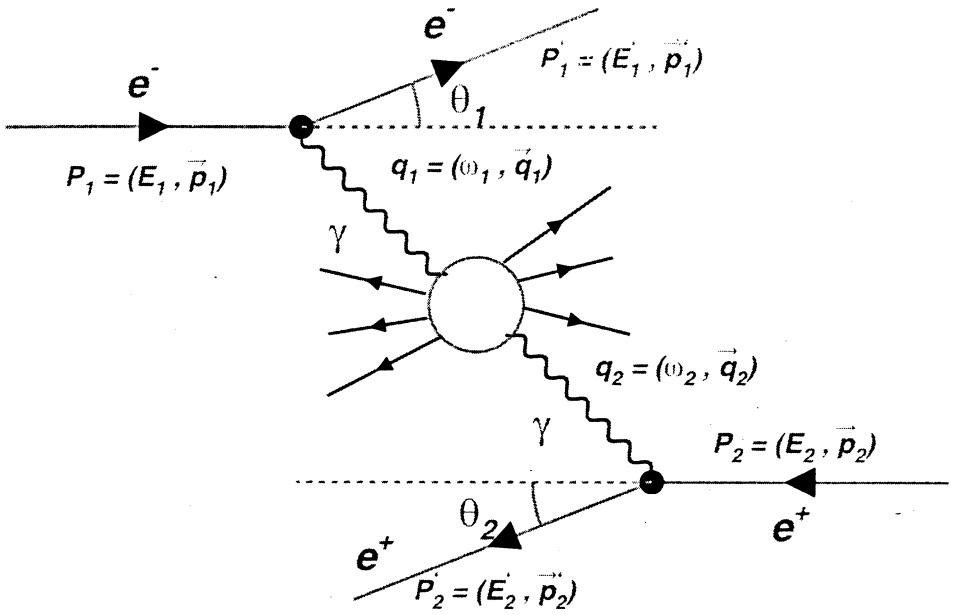

Figure 1.2: Kinematics of a two-photon interaction.

dE_γ/E_γ, therefore $W_{\gamma\gamma}$ is typically small in a e^+e^- collision compared to the center-of-mass energy $\sqrt{s}$.

The momentum transfer to the photons is dependent on the angle and the energy of the scattered electron. The transverse momentum, or photon *virtuality*, is defined by:

$$Q_i^2 = -q_i^2 \cong 2E_iE_i'(1 - \cos\theta_i). \tag{1.4}$$

When both electrons have a small scattering angle and continue down the beam pipe undetected, or *untagged*, then the photons are referred to as real or quasi-real. This *anti-tag* condition means the photons have a small transverse momemtum, or small virtuality.

The cross section for e^+e^- annihilation processes, $\sigma(e^+e^- \to X)$, at e^+e^- colliders, falls as $1/s$, except for resonance production such as Z^0. On the

other hand, the cross section for two-photon processes, $\sigma(e^+e^- \rightarrow e^+e^-X)$, grows as $(\ln (s/m^2_{electron}))^2$. This is illustrated in Figure 1.3 where the theo-

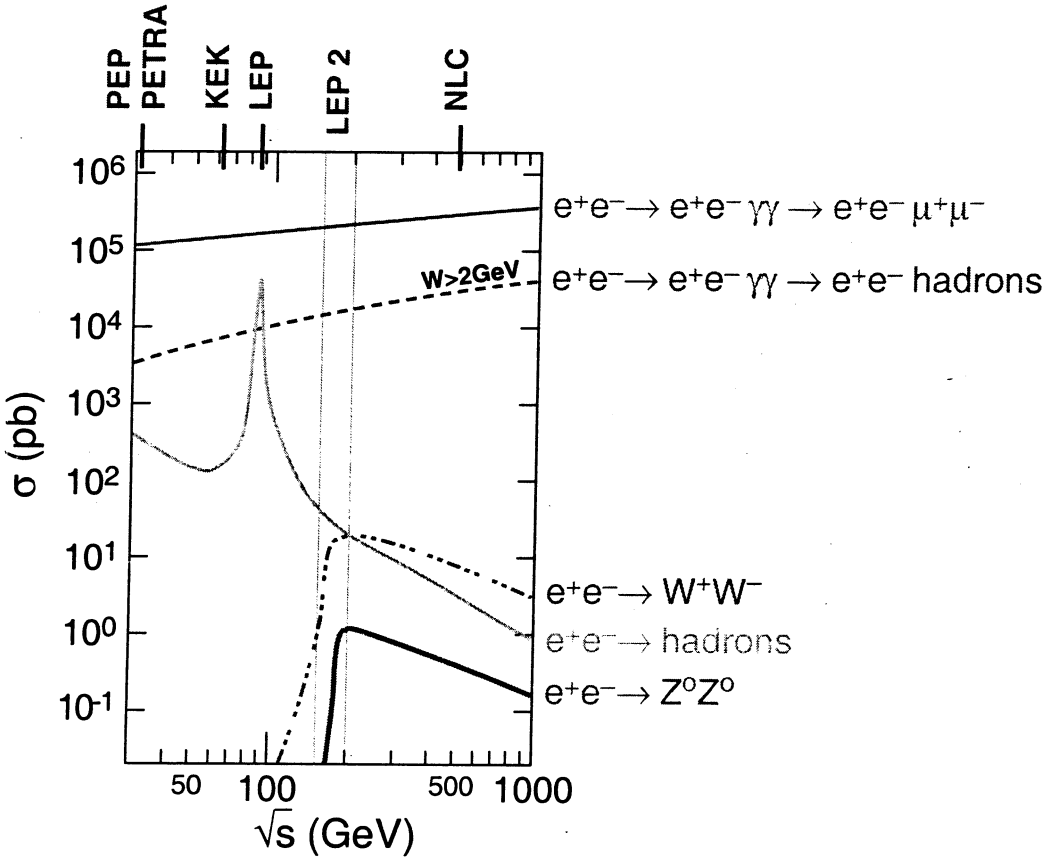

Figure 1.3: Theoretical cross sections for several physics processes at e^+e^- colliders. Two-photon interactions are the primary source of hadrons except at the Z^0 resonance.

retical cross sections of several main physics processes are given over a wide range of center-of-mass energies. At LEP2 energies, two-photon processes dominate. The two-photon process $\gamma\gamma \rightarrow$ *hadrons* is the main contribution to hadron production at LEP2. The rich hadronic structure of the photon can be studied in two-photon interactions at LEP2. Also, a good under-

standing of two-photon physics is important for those studying other physics channels at e^+e^- colliders in order to remove the non-neglible two-photon background.

1.2 LEP Collider

The Large Electron Positron (LEP) Collider [1] at the European Laboratory for Nuclear and Particle Physics (CERN) resides in a 26.7 km long underground tunnel at a depth from 50 to 150 meters and straddles the French-Swiss border near Geneva, Switzerland (Figure 1.4). The LEP Col-

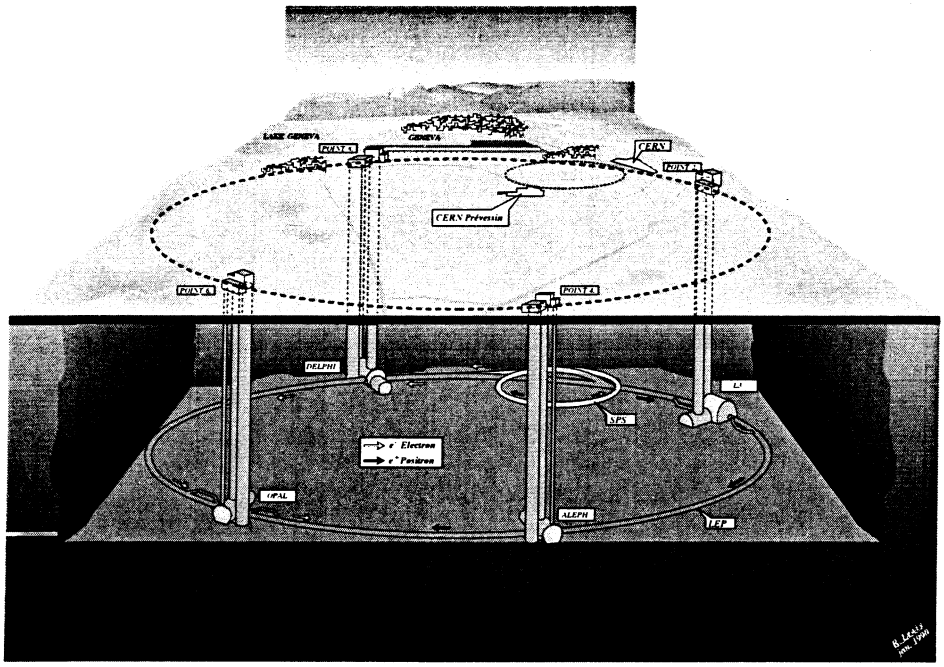

Figure 1.4: Above and below ground view of the LEP tunnel and its relation to the four LEP experiments.

lider consists of eight straight and eight curved sections which are symmetrically arranged in the shape of an octagon. After the electrons and positrons

are delivered to LEP, they are concentrated in equidistant bunches circulating in opposite directions. Radio frequency (RF) cavities provide the energy to accelerate the particles to the final beam energy as well as to compensate for losses due to synchrotron radiation. In the middle of four of the straight sections, there are four detectors, ALEPH [2], DELPHI [3], L3 [4] and OPAL [5], where the e^+e^- beams collide.

Each of the four detectors are operated by large collaborations with representatives from all around the world. The collaborators include professors, research scientists, post-doctorals, graduate students and even some undergraduates. At the date of the paper in which the analysis of this thesis is reported (see **Publications**), L3 was comprised of over 400 collaborators from 50 different institutes and universities (see **The L3 Collaboration**). Louisiana State University shares the responsiblity for the maintenance of the scintillation subdetector (see **Appendix**). The LSU members include Prof. Roger McNeil, Dr. Valery Andreev, Alan L. Stone and Sepehr Saremi.

LEP was originally designed to produce and study Z^0 bosons. From September 1989 through October 1995, LEP operated at the Z^0 resonance at the $\sqrt{s} = 91$ GeV. The LEP run at the Z-peak is commonly referred to as LEP1. Above this energy, the label LEP2 is used. In November 1995, the LEP energy went above the Z-peak for the first time ($\sqrt{s} = 130 - 140$ GeV). In 1996 LEP ran at $\sqrt{s} = 161 - 172$ GeV, the threshold for W pair production. In 1997 LEP increased to $\sqrt{s} = 183$ GeV, the threshold for Z^0 pair production [6, 7, 8, 9, 10].

1.3 Event Definition

In e^+e^- colliders, the electron beams circulate in opposing directions. If the beams are not focused and colliding, then anything recorded by the detectors is simply noise or background. The noise can originate from an old wire or faulty connection, a bad crystal in the calorimeters, a high voltage ramped too high, etc. The background comes primarily from electrons interacting with the beam gas or the wall of the beam pipe. Once the beams collide, interesting physics interactions can take place. The beams are not continuous streams of particles but instead concentrated equidistant bunches. At each bunch crossing, the e^+e^- interaction can produce one of a multitude of possible final states, and more than one e^+e^- interaction can occur at each bunch crossing. The L3 trigger system, which is discussed in Chapter 4, selects the interactions which are both interesting and well recorded by the detector.

An e^+e^- interaction which is recorded onto tape is called an *event*. The combination of events forms a data sample. The choice of which physics process to analyze will determine how to classify a given event: signal or background. The strategy for selecting a data sample is the same regardless of which physics process is analyzed. One needs to minimize the number of background events while maintaining as much signal as possible. This is done with the use of event characteristics, or *variables*, such as energy, momentum or position. A threshold, or *cut*, for a given variable is chosen in order to maximize the loss of background events while minimizing the loss of signal events.

1.4 Luminosity Measurement

The integrated luminosity is an essential parameter in any cross section measurement. The number of events, N_{events}, for a given physical process is related to the cross section, σ, and the integrated luminosity[3], $\mathcal{L}$, by the equation

$$N_{events} = \epsilon \cdot \sigma \cdot \mathcal{L}, \tag{1.5}$$

where ϵ is the selection efficiency for the process. An accurate measurement of the integrated luminosity is necessary in order to determine the absolute normalization of the event rates for the detector. The instantaneous luminosity is determined by the characteristics of colliding beams: how many particles in the bunches, how well focused are the beams, how well the beams are positioned to collide, etc. Although the beams may be colliding, an experiment may not be able to take data because of a computer software crash, down time from a change in the data aquisition tape, a fault in some component of a subdetector, etc. Therefore, the integrated luminosity must be measured by each experiment.

The luminosity is measured using Eq. 1.5 for a physical process with a large and extremely well known cross section. At LEP the ideal process is the low-angle Bhabha scattering, $e^+e^- \rightarrow e^+e^-$. The Bhabha cross section at low polar angles is very large, and it is dominated by the exchange of a photon as shown in Figure 1.5.

To the lowest order at small angles, the total cross section of the Bhabha scattering, integrated over the azimuthal angle, ϕ, in a detector with a polar

[3]To simplify the notation, I will use $\mathcal{L}$, instead of $\int \mathcal{L}$ dt, to denote the integrated luminosity.

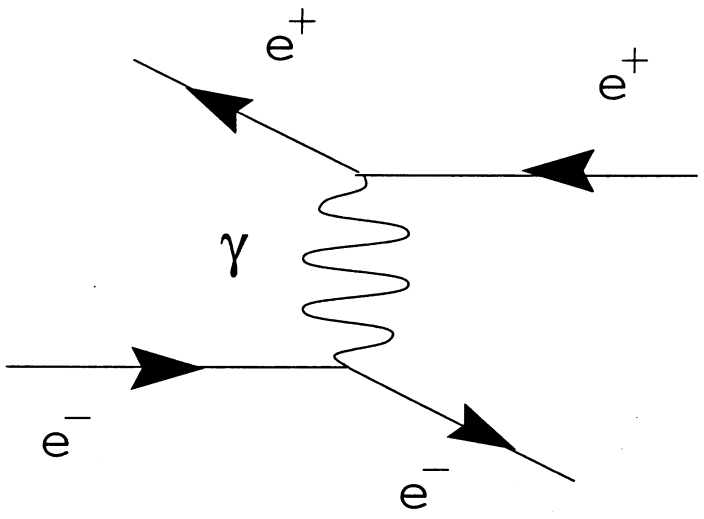

Figure 1.5: The exchange of a photon at small angles for Bhabha scattering $e^+e^- \rightarrow e^+e^-$.

angle coverage from θ_{min} to θ_{max} is given by:

$$\sigma \simeq \frac{1065.6 \text{ nb GeV}^2}{s} \left(\frac{1}{\theta^2_{min}} - \frac{1}{\theta^2_{max}} \right), \tag{1.6}$$

where s is the square of the center-of-mass energy. In the L3 experiment, we detect low-angle Bhabhas using the Luminosity Monitor (see **Chapter 3**).

1.5 Heavy Flavor Production

Heavy flavor in two-photon collisions is produced in the reaction $\gamma\gamma \rightarrow Q\bar{Q}$ where Q is a heavy mass quark (c, b and t). The total cross section for heavy flavor production is mainly limited to the charm quark contribution. The cross section is proportional to e^4_Q/m^2_Q. Because of their smaller electric charge and larger mass, the production of beauty is expected to be suppressed by more than two orders of magnitude relative to the production of charm quarks [11]. There is not enough energy at LEP, where $\sqrt{s} < 200$ GeV, in order to produce a top quark pair.

The first evidence of charm came in November 1974 with the measurement of a new particle with a mass of 3.1 GeV, the heaviest known particle at the time. The discovery of the new particle, called J/Ψ, was made by two different groups of researchers led by Samuel Ting at Brookhaven and Burton Richter at the Stanford Linear Accelerator (SLAC). The J/Ψ is a bound state of a quark and antiquark with a quantum number designated by C (for charm), which must be conserved in strong and electromagnetic interactions. A bound state of a charm and anticharm quark is called *charmonium.* Further experimentation over the following years has led to the discovery of charmed hadrons ($C = \pm 1$) and excited states of charmonium ($C = 0$). The lightest charmed hadron is called the D meson where $D^+ = c\bar{d}$ and $D^0 = c\bar{u}$. Charmonium and charmed hadrons are highly unstable particles with very short lifetimes. Therefore, they cannot be measured directly, but instead, they are detected and their masses determined through their decay products. The charm quarks are confined to a bound state. The mass of a charmonium state or a charmed hadron is not simply the sum of its constituent quarks. Therefore, the charm quark mass currently has a very large uncertainty, $m_c = 1.45 \pm 0.45$.

Two main mechanisms contribute to the charm production in two-photon collisons. A photon can interact as a point-like particle, where the two photons couple directly to the charm quarks (Figure 1.6a). If a photon resolves into a flux of light quarks and gluons, one of the gluons may "fuse" with the second photon to form the $c\bar{c}$ pair (Figure 1.6b). The remaining light quarks and gluons produce a remnant jet in the direction of the resolved photon.

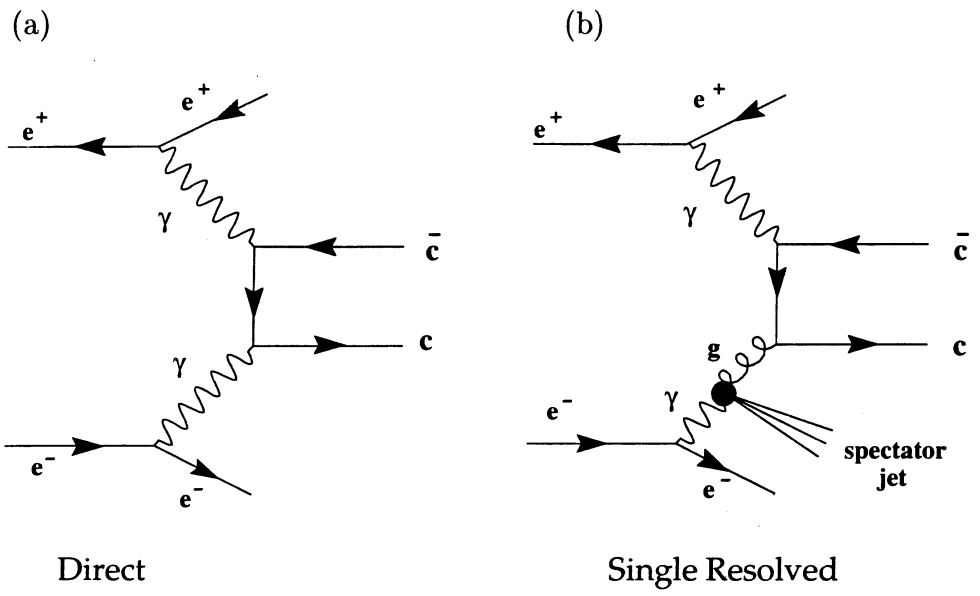

Figure 1.6: Diagrams contributing to charm production in two-photon collisions at LEP.

This process where the resolved photon is probed by the other point-like photon is called *single-resolved.* The gluon content, or density, of the photon is not well established or measured experimentally. In addition to understanding the charm quark, one of the primary reasons to study charm production in two-photon collisions is to learn about the gluon content of the photon.

Below the LEP1 beam energy, the *direct* process is expected to be dominant. As the center-of-mass energy increases, the cross section for resolved processes is expected to rise, becoming comparable to the direct process at LEP2 energies.

Charm production in two-photon collisions has been measured at PEP, PETRA, TRISTAN and LEP [12, 13, 14, 15, 16, 17, 18], where charm quarks were identified by charged D^* mesons and inclusive leptons (Figure 1.7). D^{*+} mesons were detected by their decay to $D^0\pi^+$, where the available kinetic en-

ergy is only 6 MeV. The D^0 decays to a variety of final statess and usually only a few are considered. The signal for charm is typically seen by plotting $\Delta M = M_{D^{*+}} - M_{D^0}$ for all the reconstructed decay product candidates (kaons and pions). Charmed hadrons were also identified by their semileptonic decays to electrons and muons. The lepton tag method is used in this thesis; this is described in more detail in Chapter 5.

All but one of these cross section measurements were made at center-of-mass energies below 60 GeV, where they do not clearly discriminate between the QCD predictions to next-to-leading order (NLO) accuracy of the direct process and the sum of the direct and resolved processes. Only one measurement has been made at a center-of-mass energy above 60 GeV. All the measurements shown in Figure 1.7 were performed by experiments at a single value of $\sqrt{s}$ and suffer from poor statistics. In this analysis, the inclusive charm cross sections are measured with higher statistics at four different center-of-mass energies. The cross sections presented by this thesis are the first measured at LEP2 energies, where the resolved contribution to the charm production is predicted to be comparable to the direct. Thus, the data should provide evidence for the gluon content of the photon.

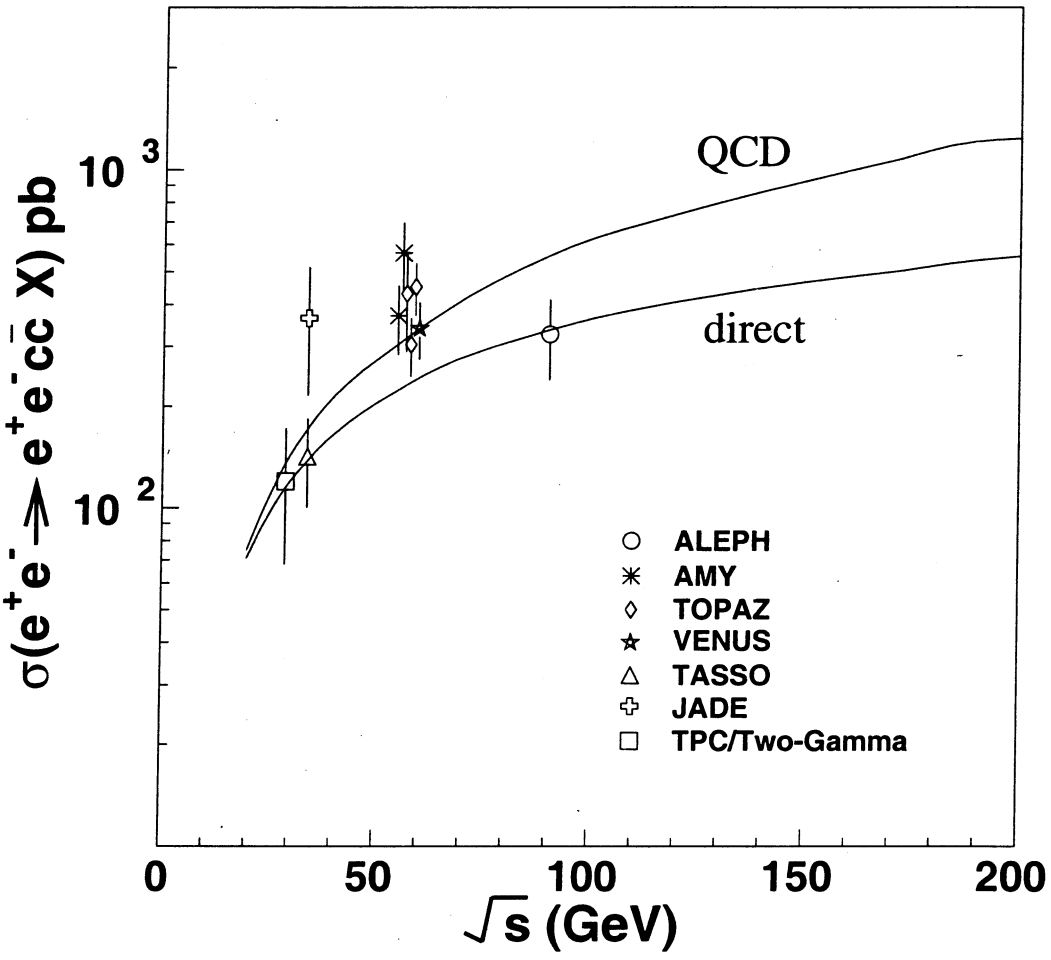

Figure 1.7: The charm production cross section in two-photon collisions prior to the measurements made by L3 at LEP. Calculated to NLO accuracy, the dashed line corresponds to the direct process prediction while the solid line shows the QCD prediction for the sum of the direct and the resolved processes [11].

CHAPTER 2

CHARM PRODUCTION IN TWO-PHOTON PHYSICS

The measurement of a physical process is more meaningful when there is a theory in which to compare. The selection criteria for the data, the rejection of background and the comparison to prediction is developed through the use of a well-tested Monte Carlo simulation. There are several general purpose Monte Carlo codes which simulate charm production in two-photon interactions [19]. These generators are adapted from hadron-hadron and electron-positron studies, and they have been tuned to HERA [20] data for γp scattering, thus incorporating all the physics constraints necessary to reliably describe two-photon interactions. For the description of hard scattering processes by perturbative QCD, the theoretical predictions need to be reliable to at least the NLO logarithmic order in perturbation theory.

The Monte Carlo PYTHIA [21] is used by the L3 experiment for the measurement of the inclusive charm production at LEP. PYTHIA simulates the full range of hadronic two-photon reactions: $e^+e^- \rightarrow e^+e^-q\bar{q}$. However, the luminosity function generates only real incoming photons. Also, the leading order parameterization of the parton distribution of the photon includes low mass (soft) VDM contributions and high mass (hard) quark pair fluctuations. The hard scattering processes are expected to be the dominant source of charm production. The emphasis of this chapter is to review the theoretical elements utilized in PYTHIA.

2.1 Photon Generation

The spectrum of photons emitted from an electron $e \rightarrow e + \gamma$ is:

$$d^2N_e = \frac{\alpha_{em}}{\pi}\frac{d\omega}{\omega}\frac{dQ^2}{Q^2}\left[\frac{\mathbf{q_T^2}}{Q^2} + \frac{\omega^2}{2E^2}\right] \tag{2.1}$$

$$\frac{\mathbf{q^2}}{Q^2} = \left(1 - \frac{\omega}{E}\right)\left(1 - \frac{Q^2_{min}}{Q^2}\right). \tag{2.2}$$

E is the energy of the electron, ω is the photon energy and Q^2 is the photon virtuality (Eq. 1.4).

$$\begin{aligned} Q^2_{min} &= Q^2_0 \equiv \tfrac{m_e^2\omega^2}{E(E-\omega)} \quad (\theta_{min} = 0) \\ &= E(E-\omega)\theta^2_{min} \quad (\theta_{min} \neq 0) \end{aligned} \tag{2.3}$$

The electromagnetic interaction of particle A with another particle B can be approximated by the interaction of the radiated photon with B:

$$d^2\sigma[A + B \rightarrow A' + X](E) = \sigma[\gamma + B \rightarrow X](w, Q^2 = 0)d^2N_A \tag{2.4}$$

This is known as the equivalent photon approximation (EPA) [22]. The photo-absorption cross section $\sigma[\gamma B \rightarrow X]$ describes the cross section for the absorption of a real photon, $Q^2 = 0$, which is purely transversely polarized. The EPA ignores effects such as when the exchanged photon is off mass-shell and contains a longitudinal polarization component. The fast fall-off with Q^2 in Eq. 2.1 suggests that these effects are small. The EPA is implemented in PYTHIA to generate hadronic two-photon interactions.

We now consider the specific case of photon radiation from electrons. After introducing the scaled photon energy $x = \omega/E$, the photon spectrum can be rewritten as:

$$d^2N_e = \frac{\alpha_{em}}{\pi}\frac{dx}{x}\frac{dQ^2}{Q^2}\left[S(x) + \frac{m_e^2x^2}{Q^2}\right] \tag{2.5}$$

where

$$S(x) = 1 - x + \frac{x^2}{x}. \tag{2.6}$$

Integrating over Q^2, the resulting equation is:

$$dN(x) = \frac{\alpha_{em}}{\pi}\frac{dx}{x}\left(S(x)\ \ln\frac{Q^2_{max}}{Q^2_{min}} - m_e^2x^2\left[\frac{1}{Q^2_{min}} - \frac{1}{Q^2_{max}}\right]\right). \tag{2.7}$$

The Q^2 range depends on the experimental set-up. For the anti-tag condition, there is a maximum scattering angle defined for the scattering electron:

$$Q^2_{max} = Q^2_0 + 4(1-x)E^2\sin^2\frac{\theta^2_{max}}{2} \approx (1-x)E^2\theta^2_{max} \tag{2.8}$$

Typically, no minimum tagging angle is applied so that $Q^2_{min} = Q^2_0$.

In analogy to Eq. 2.4, the cross section of $e^+e^- \to e^+e^-X$ at $\sqrt{s} = 2$ E, where E is the beam energy, is expressed as the convolution of the cross section for $\gamma\gamma \to X$ and the two-photon luminosity function, $L_{\gamma\gamma}$,

$$d\sigma_{ee}(s) = dL_{\gamma\gamma}\sigma_{\gamma\gamma}(W^2 = x_1x_2s) \tag{2.9}$$

where $dL_{\gamma\gamma} = dN_1dN_2$ and $N_i = N(x = x_i, Q^2 = Q_i^2)$. The two-photon cross section describes the scattering of two *real* photons. The two-photon center-of-mass energy is commonly denoted as $\sqrt{s_{\gamma\gamma}} = W$.

The analytical expression for the two-photon luminosity function is:

$$dL_{\gamma\gamma} = \frac{dz}{z}\left(\frac{\alpha_{em}}{\pi}\right)^2\left(L^2\left[(z^2+2)^2\ln\frac{1}{z} - (1-z^2)(3+z^2)\right] - \frac{16}{3}\ln^3\frac{1}{z}\right) \tag{2.10}$$

where

$$z = \frac{W}{\sqrt{s}}, \quad L = \ln\frac{E^2\theta^2_{max}}{m_e^2z^2} - 1. \tag{2.11}$$

$L_{\gamma\gamma}$ may be written as a function of $W = z\sqrt{s}$:

$$\frac{dL_{\gamma\gamma}}{dW} = \frac{1}{\sqrt{s}}\frac{dL_{\gamma\gamma}}{dz}. \tag{2.12}$$

$L_{\gamma\gamma}/dz$ is dimensionless, while $L_{\gamma\gamma}/dW$ has the dimension of inverse mass (GeV^{-1}). The dominant behavior of the luminosity function can be determined from Eq. 2.10:

$$\frac{dL_{\gamma\gamma}}{dW} \approx \left(\frac{\alpha_{em}}{\pi}\right)^2 \frac{4}{W} L^2 \ln\frac{1}{z} \approx \left(\frac{\alpha_{em}}{\pi}\right)^2 \frac{16}{W} \ln\frac{\sqrt{s}}{W} \ln^2\frac{\sqrt{s}}{2m_e}. \tag{2.13}$$

$L_{\gamma\gamma}$ increases as $\ln^3 s$ with e^+e^- center-of-mass energy $\sqrt{s}$, and decreases quickly for larger two-photon invariant masses W. This is demonstrated in Figure 1.3.

2.2 Photon Structure

The photon wave function may be written as [23]:

$$|\gamma\rangle = c_{bare}|\gamma_{bare}\rangle + \sum_{V=\rho^0,\omega,\phi,J/\psi} c_V|V\rangle + \sum_{q=u,d,s,c,b} c_q|q\bar{q}\rangle + \sum_{\ell=e,\mu,\tau} c_\ell|\ell^+\ell^-\rangle. \tag{2.14}$$

This representation is analogous to the main event classes in γp events:

- In the direct events, the bare photon interacts directly with a parton from the proton.
- In the VDM events, the photon fluctuates into a vector meson, predominantly a ρ^0. All processes allowed in hadron-hadron interactions may occur.
- In anomalous events, the photon fluctuates into a $q\bar{q}$, and one of these or a daughter parton thereof interacts with a parton from the proton.

- The $|\ell^+\ell^-\rangle$ states can only interact strongly with partons inside the hadron at higher orders, therefore they contribute negligibly to the total hadronic cross section. The leptonic fluctuations are perturbatively calculable, with a cut-off provided by the lepton mass.

In order that the above classification is continuous and free of double counting, Eq. 2.14 assumes there exists a cut-off k_0. Above k_0, the $\gamma \to q\bar{q}$ fluctuations can be described perturbatively, while below k_0 the fluctuations are assumed to give vector meson states. An additional cut-off, $p_{\perp\min}^{\text{anom}}$, is needed to separate low-$p_\perp$ and high-$p_\perp$ physics. This sets the scale for anomalous photon partons to interact in a hard process. Both scales have been parameterized [24] where $k_0 \approx 0.5$ GeV and

$$p_{\perp\min}^{\text{anom}}(s) \approx 0.6 + 0.125\ (\ln(1 + \sqrt{s}/10))^2\ \ [\text{GeV}]. \tag{2.15}$$

In Figure 2.1, the allowed phase space is represented by a two-dimensional plane with two transverse momentum scales, $k_\perp$ and $p_\perp$. The region $k_\perp < k_0$ corresponds to a small transverse momentum at the $\gamma \to q\bar{q}$ vertex, and thus to VDM processes. For $k_\perp > k_0$, the events split along the diagonal $k_\perp = p_\perp$. If $k_\perp > p_\perp$, the hard process $\gamma g \to q\bar{q}$ occurs, and the lower part of the graph is part of the leading log QCD evolution of the gluon distribution inside the proton. These events are direct ones. If $p_\perp > k_\perp$, the hard process is $\bar{q}q' \to \bar{q}q'$ (where q' may also represent an antiquark), and the $\gamma \to q\bar{q}$ vertex builds up the quark distribution inside a photon. These events are thus anomalous ones.

In conventional notation, $c_V^2 = 4\pi\alpha_{\text{em}}/f_V^2$ which gives the probability for the transition $\gamma \to V$. The coefficients for $f_V^2/4\pi$ are determined from data

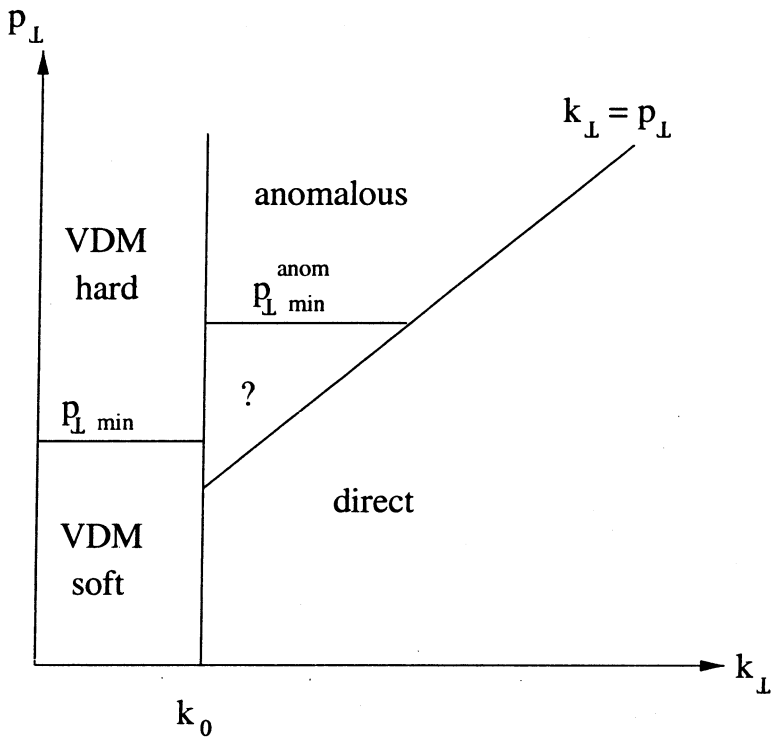

Figure 2.1: The allowed phase space for hadronic two-photon processes. The different event classes are subdivided in the two-dimensional plane defined by two transverse momentum scales.

to be 2.20 for ρ_0, 23.5 for ω, 18.4 for ϕ and 11.5 for J/ψ. The contribution from the anomalous high mass fluctuations depends on the scale $\mu \sim p_{\perp min}^{anom}$ used to probe the photon

$$c_q^2 \approx \frac{\alpha_{em}}{2\pi}\left(2\sum_q e_q^2\right)\ln\left(\frac{\mu^2}{k_0^2}\right), \tag{2.16}$$

where q runs over the quarks that can be taken as massless compared with μ. A similar expression can be obtained for the lepton component. When properly normalized, c_{bare} describes the probability distribution of a photon to remain a photon

$$c_{\text{bare}}^2 = 1 - \sum c_V^2 - \sum c_q^2 - \sum c_\ell^2. \tag{2.17}$$

In practice, $c_{\text{bare}} \approx 1$ is a sufficiently good approximation for all applications.

In two-photon events, the superposition described in Eq. 2.14 applies separately to each of the incoming photons. In total there are three times three event classes. By symmetry, the combinations are reduced to six distinct classes.

1. VDM × VDM. Both photons fluctuate into vector mesons, and the processes are the same as hadron-hadron interactions.

2. VDM × direct. A bare photon interacts with the partons of the VDM photon.

3. VDM × anomalous. The anomalous photon perturbatively branches into a $q\bar{q}$, and one of these interacts with a parton from the VDM photon.

4. Direct × direct. The two photons directly give a quark pair, $\gamma\gamma \to q\bar{q}$.

5. Direct × anomalous. The anomalous photon perturbatively branches into a $q\bar{q}$ pair, and one of these interacts with the other photon.

6. Anomalous × anomalous. Both photons perturbatively branch into $q\bar{q}$ pairs, and subsequently one parton from each photon undergoes a hard interaction.

The main parton-level processes that occur in the six classes are:

- The *direct* processes $\gamma\gamma \to q\bar{q}$ only occur in class 4.

- The *single-resolved* processes $\gamma q \to qg$ and $\gamma g \to q\bar{q}$ occur in classes 2 and 5.

- The *double-resolved* processes $qq' \to qq'$, $q\bar{q} \to q'\bar{q}'$, $q\bar{q} \to gg$, $qg \to qg$, $gg \to q\bar{q}$ and $gg \to gg$ occur in classes 1, 3 and 6.

- Low-$p_\perp$ events occur in class 1.

The notation of direct, single-resolved and double-resolved is the conventional subdivision of two-photon interactions. The rest is then called soft-VDM.

2.3 Direct and Resolved Processes

The direct and resolved processes are the main mechanisms for the production of heavy quarks in two-photon collisions. The J/ψ produced through VDM are highly suppressed relative to lighter vector mesons [24]. The contribution from the double-resolved process is expected to be negligible at LEP center-of-mass energies [11]. In Figure 1.7, the previous measurements of charm production are plotted against the prediction to NLO accuracy of the direct process and the sum of the direct and single-resolved processes. The diagrams contributing to this NLO QCD prediction are illustrated in Figure 2.2.

In the case of direct production, the photons couple directly to the heavy quarks. QCD corrections include the virtual plus soft gluon corrections and hard gluon radiation (Figures 2.2a-c). The direct production channel may be summarized as

$$\sigma(\gamma\gamma \to Q\bar{Q}(g)) = \frac{\alpha_{em}^2 e_Q^4}{m_Q^2}(c_{\gamma\gamma}^{(0)} + 4\pi\alpha_s c_{\gamma\gamma}^{(1)}). \tag{2.18}$$

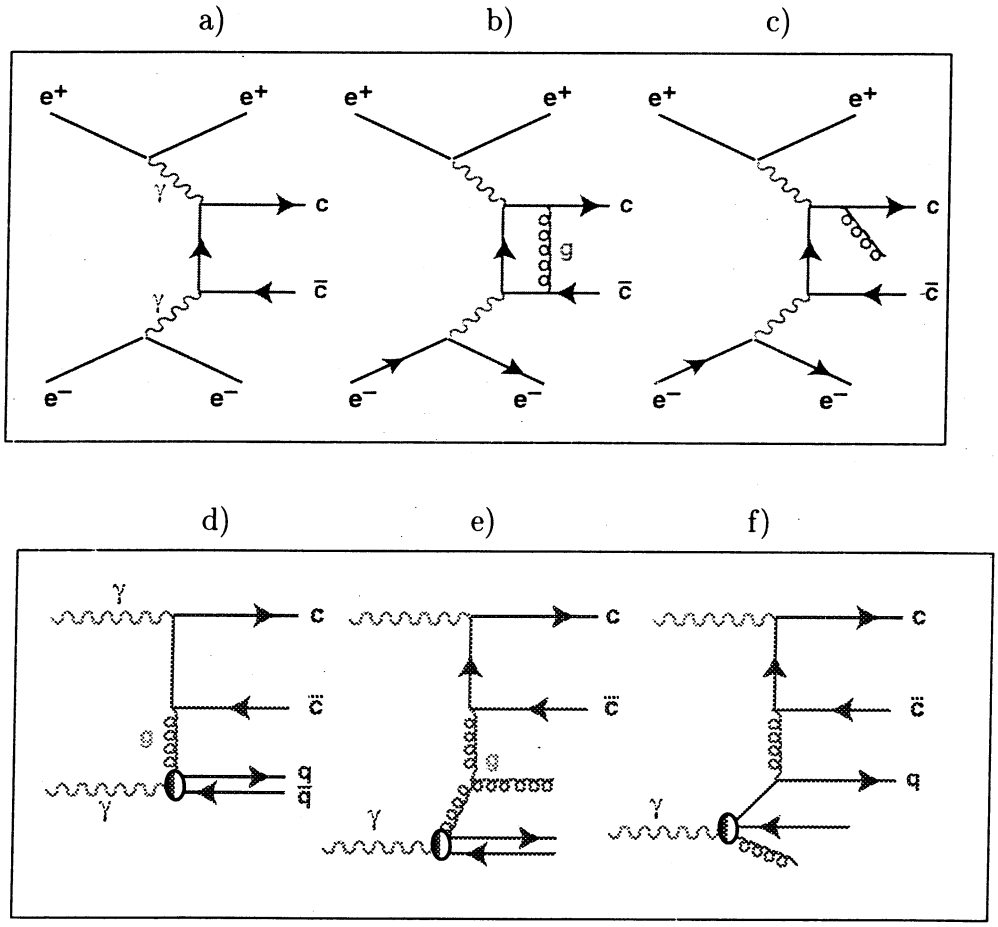

Figure 2.2: Next-to-leading order diagrams contributing to charm production in two-photon collisions. a) and d) are leading order direct and resolved processes. b-c) and e-f) are the NLO contributions due to virtual gluon radiation.

The functions $c_{\gamma\gamma}^{(0,1)}$ depend on the ratio $\rho = s_{\gamma\gamma}/4m_Q^2$. The direct cross section depends only on the heavy quark mass and the QCD coupling constant, α_s.

If one of the photons resolves into a flux of light quarks and gluons, one of the gluons may interact with the second photon to form the $Q\bar{Q}$ pair. The remaining partons produce a specatator jet in the direction of the resolved photon. The leading order resolved cross section can be derived by replacing $\alpha_{em}^2 e_Q^4$ by $\frac{4}{3}\alpha_{em}\alpha_s e_Q^2$ for the basic $\gamma g \to Q\bar{Q}$ diagram (Figure 2.2d). Besides the virtual QCD corrections and the soft and hard gluon radiation, the cross section in NLO involves the diagram $\gamma q \to Q\bar{Q}q$ (Figures 2.2d-f). The QCD corrected cross section may be parameterized as

$$\sigma_{\gamma i} = \frac{\alpha_{em}\alpha_s e_Q^2}{m_Q^2} c_{\gamma i}^{(0)} + 4\pi\alpha_s (c_{\gamma i}^{(1)} + c_{\gamma i}^{(1)} \log\frac{p_\perp^2}{m_Q^2}) \quad (i = g, q). \tag{2.19}$$

The coefficients are functions of $c_{\gamma i}/4m_Q^2$ and depend on the quark and gluon densities of the photon.

PYTHIA adopts the parameterizations of the parton densities in the real photon developed by Glück-Reya-Vogt (GRV) [26]. The photon structure function used in PYTHIA is the SaS1D [24] model which gives a description of the hadronic final states produced in two-photon collisions.

Only the leading order direct and single-resolved processes (Figure 2.2a & d) are calculated in PYTHIA.

2.4 Renormalization Scale and the Charm Mass

One of the motivations to measuring the charm production in two-photon collisions is to constrain the charm mass. In Figure 2.3, the cross section to NLO accuracy is illustrated for both the direct and the full QCD predictions. From equations 2.18 and 2.19, a larger charm mass results in a smaller

production rate. Naively, one could expect to make a good estimate of the charm mass from Figure 2.3 with an accurate measurement of the cross section. However, that is not the entire picture. There is additional uncertainty to the cross section predictions due to the renormalization scale.

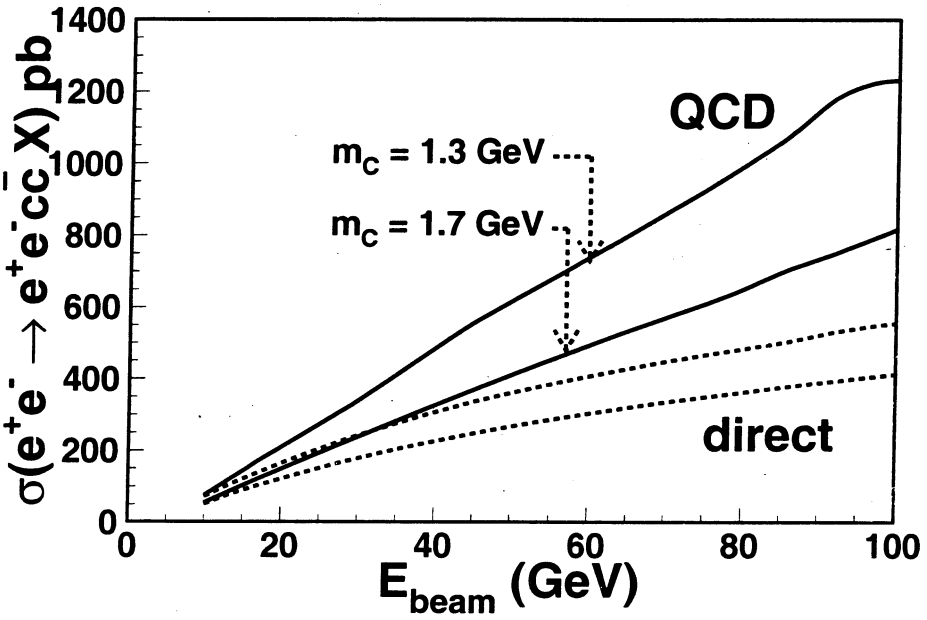

Figure 2.3: The charm cross section to NLO accuracy for direct and QCD prediction for a charm mass of 1.3 and 1.7 GeV.

In NLO, terms proportional to $\alpha_s \ln(p_\perp^2/m_c^2)$ (Eq. 2.19) arise from collinear emission of gluons by charm quarks at large transverse momentum ($p_\perp$) or from almost collinear branching of gluons or photons into charm quark pairs. Theses terms are not expected to affect the total charm production rates, but they might spoil the convergence of the perturbation series and cause large scale dependences of the NLO result at $p_\perp \gg m_c$ [27]. Therefore, a renormalization scale mass μ is introduced to separate the finite and divergent

terms, A convenient choice for this scale is the charm mass. However, this is a phenomenological parameter. There is some uncertainty in the choice of scale mass which leads to uncertainty in the total cross section prediction.

In Figures 2.4a-b, the NLO direct and QCD predictions are shown for two values of the charm mass, $m_C = 1.3$ and 1.7 GeV. To illustrate the uncertainty in the renormalization scale, μ is varied from m_C to $2m_C$. The cross section prediction decreases with an increase in the scale mass choice. For $m_C = 1.3$ GeV, the QCD prediction decreases by an average of 30%, by changing the renormalization scale μ from m_C to $2m_C$, and it decreases by an average of 15% for $m_C = 1.7$ GeV. Even with an accurate measurement of the total charm cross section, the uncertainty due to the renormalization scale is too large to make a statement on the charm mass. However, the direct process depends mainly on the charm mass and the QCD coupling constant. There is very little sensitivity to the renormalization scale in the direct prediction. Therefore, if there is a mechanism to separate the direct production of charm from the resolved, one may be able to constrain the charm mass.

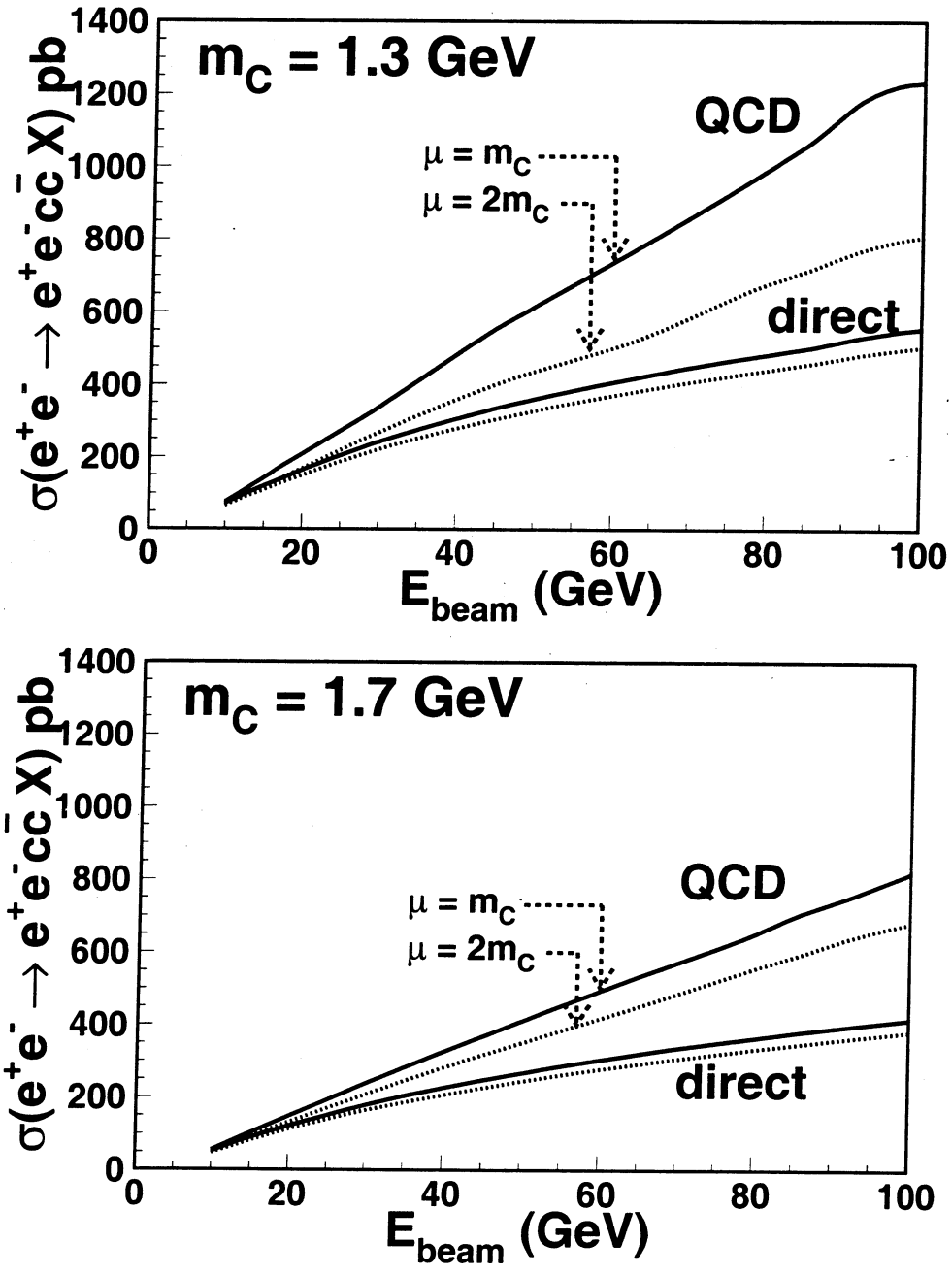

Figure 2.4: The uncertainty to the charm production prediction due to the change in the renormalization scale from m_C to $2m_C$.

CHAPTER 3

THE L3 EXPERIMENT

The general detector structure at an electron-positron collider is shown in Figure 3.1. The detector is symmetric about the beam axis and in the forward-backward directions about the interaction point. There is a magnetic field parallel to the beam axis in order to curve the tracks of charged particles. A typical detector will have at least four sections, or subdetectors, which are in concentric layers about the beam pipe. First, the vertex subdetector measures the momenta of charged particles and reconstructs an event interaction point. This is done by detecting the ionization energy loss (dE/dx_{ioniz}) of charged particles and measuring their position accurately along the trajectory. From the curvature of the trajectory in the magnetic field, the transverse momentum component is measured.

Highly energetic charged particles other than electrons lose energy in matter primarily through ionization. This energy loss is proportional to $\rho \cdot \beta^{-2}$, where ρ is the density of the absorbing material and β is the velocity of the particle as a fraction of the speed of light. The energy loss from ionization reaches a minimum at $\beta = 0.96$. Particles at this point are called *minimum ionizing particles* (MIPs). For $\beta > 0.96$, there is an increase in dE/dx losses due to the relativistic effect of the ionizing particle experiencing a larger electric field transverse to its direction of motion. A further correction is made to the ionization loss. The density effect is due to the polarization of the medium which opposes the relativistic rise. For solids, it

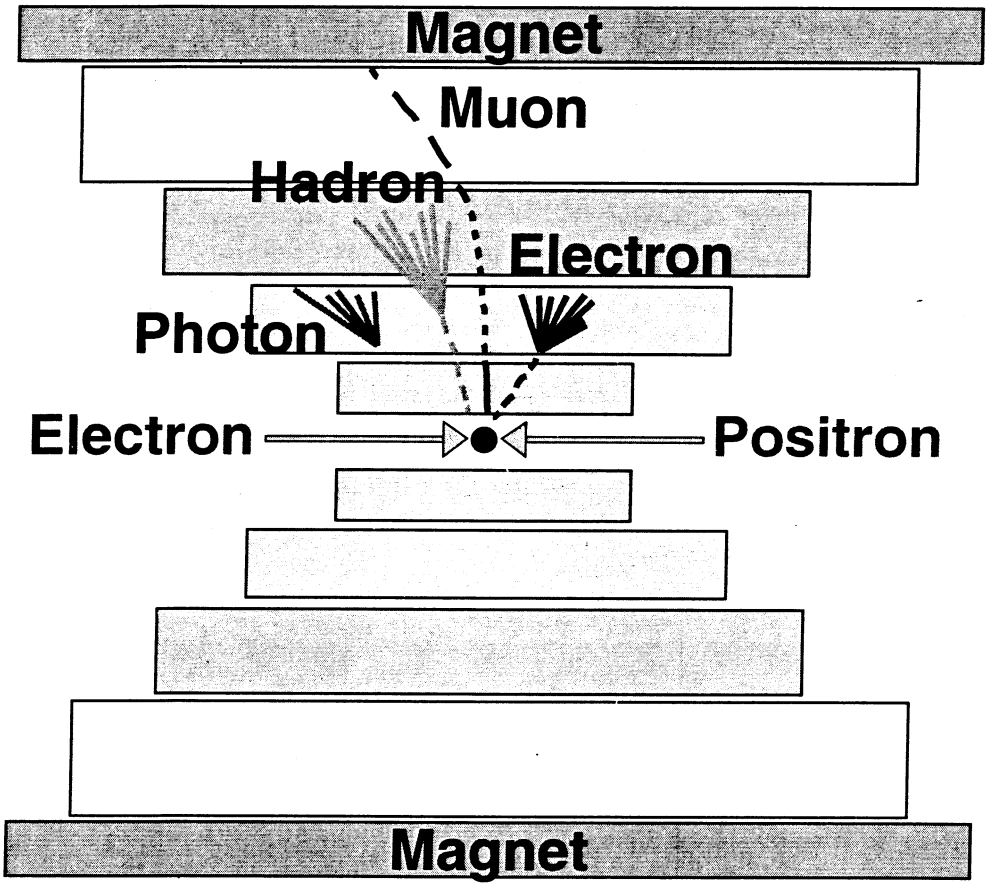

Figure 3.1: Diagram for a general detector for an electron-positron collider. Concentric sections, or subdetectors, are used to measure the energy and positions for electrons, hadrons and muons.

is about 10-20% above the minimum ionization. Although electrons also lose energy through ionization, the energy loss from bremsstrahlung dominates above a particle energy of 10 MeV.

Calorimeters are devices which measure the total energy of a particle. The electromagnetic calorimeter is made of a scintillating material in which photons and electrons shower and lose all of their energy. The electrons and photons lose their energy through electromagnetic interactions with nuclei. The interaction processes are bremsstrahlung:

$$\begin{aligned} e^+ + N &\rightarrow e^+ + N + \gamma \\ e^- + N &\rightarrow e^- + N + \gamma \\ \gamma + N &\rightarrow e^+ + e^- + N. \end{aligned} \tag{3.1}$$

An electromagnetic cascade or shower is produced which alternates between bremsstrahlung and pair production. These are the main mechanisms by which electrons and photons lose energy when passing through matter. The showering process converts the kinetic energy of the incident particle into a large number of electrons and photons. The shower reaches a maximum when the bremsstrahlung photons no longer have enough energy to pair produce. The energy is measured from the amount of ionization produced by the charged particles in the shower.

A parameter is defined to describe the distance over which the electron energy is reduced by a factor 1/e (63%) due to radiation loss. This quantity is called the radiation length and is proportional to the square of the atomic number of the material (Z). Electromagnetic calorimeters must have sufficient material, typically 15-25 radiation lengths, in order to completely absorb electron and photon showers. Total absorption calorimeters are made

of a single material, such as sodium iodide (NaI) or bismuth germanium oxide (BGO), which acts as both a shower initiator and ionization detector. The large numbers of electrons produced in the electromagnetic shower lose energy by ionization, and these energy losses excite vibrational modes of the molecules in the scintillators which then radiate scintillation light. The amount of scintillation light is proportional to the incident energy of the electrons and photons since all of the energy is contained.

The hadron calorimeter is composed of a material to stop hadron showers and to measure the energy and directions of hadrons. A dense material such as uranium or lead is used to increase the energy loss from ionization because there are more nuclei per unit length in the path of the incident hadron. In addition, strong interactions occur between the hadrons and the nuclei in the material. A hadron shower results when an incident hadron undergoes an inelastic nuclear collision with production of secondary hadrons which may then also interact inelastically to produce further generations of hadrons. In addition, neutral pions decay promptly into two photons which then generate showers by pair production and bremsstrahlung. Therefore, the hadron shower has an electromagnetic component. The absorbing material in a hadron calorimeter is specified by its interaction length which is large compared to the radiation length for heavy elements. Hadronic calorimeters have typically about 10 interaction lengths.

Finally, there is a subdetector called a muon chamber to measure the momentum and track position of muons which interact weakly with matter and consequently penetrate the calorimeters. A muon has a much smaller prob-

ability for bremsstrahlung compared to the electron. The emission probability for bremsstrahlung is inversely proportional to the square of the particle mass. The radiation loss by muons, the next lightest charged particle where $m_\mu/m_e \sim 200$, is 40,000 times smaller than that for electrons. Therefore, the muon will be detected only as a minimum ionizing particle in the electromagnetic and hadronic calorimeters and continues into the muon chamber. The trajectory of the muon is accurately measured and, combined with the magnetic field, the transverse mometum is calculated.

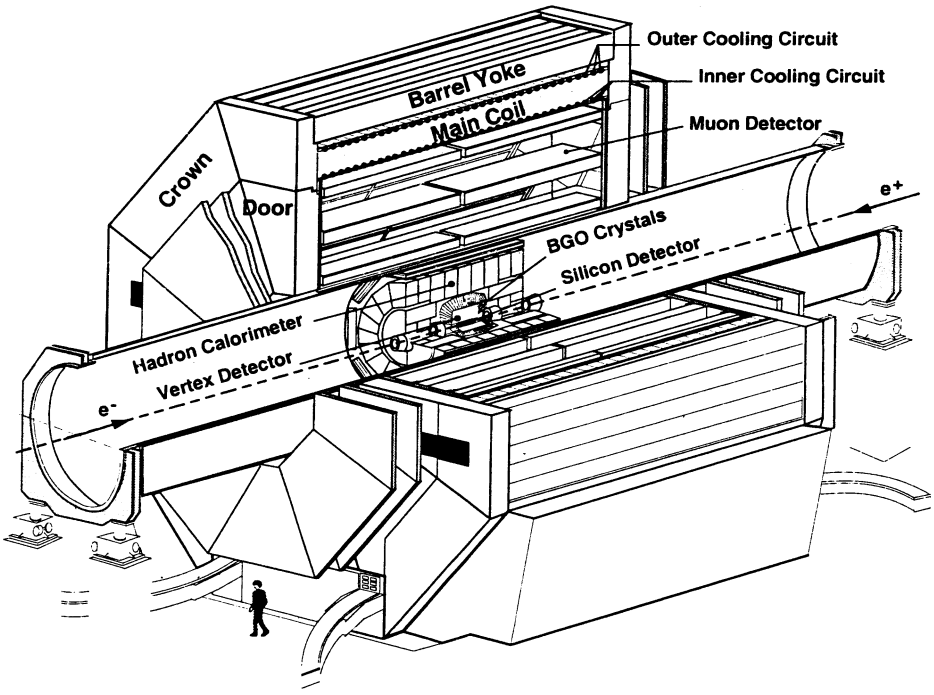

Figure 3.2: The L3 detector.

The L3 detector shown in Figure 3.2 was designed to study e^+e^- interactions in the center-of-mass energy range from 80 to 200 GeV with an emphasis on the high resolution measurements of electrons, photons, muons

and hadronic jets. The detector, which is located at the second interaction point of the LEP collider, is 14 m long and has a diameter of 16 m. It resides within a 7800 ton magnet which provides a uniform field of 0.5 T parallel to the beam axis. The choice of the low field and the large volume optimizes the muon momentum resolution.

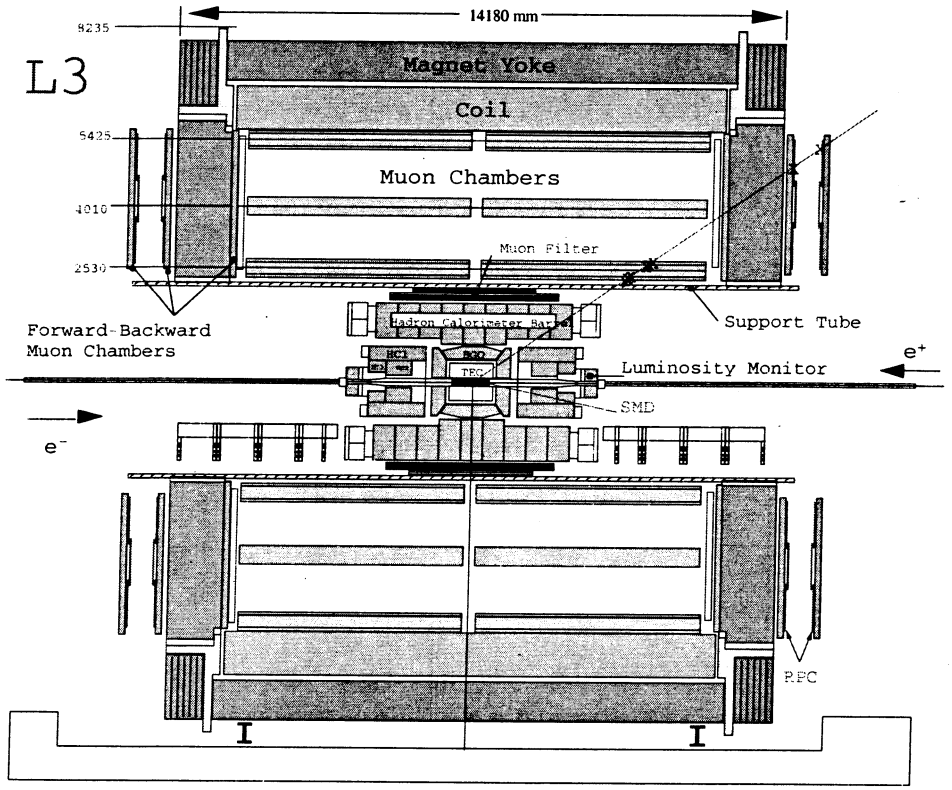

Figure 3.3: A side view of the L3 detector.

The central part of the L3 detector is housed in a steel support tube, which is 32 m in length and 4.45 m in diameter (Figure 3.3). The tube is concentric with the LEP beam line and symmetric with respect to the interaction point. The muon spectrometer is mounted outside the support tube and inside the

octagonal-shaped solenoidal magnet. The L3 coordinate system places the origin at the center of the detector. The positive z-axis points along the beam pipe in the direction of the electron beam. The positive x-axis points toward the center of the LEP ring; the positive y-axis points upwards, perpendicular to the plane of the LEP ring. In polar coordinates, θ is the angle from the positive z-axis, ϕ is the angle in the x-y plane measured counterclockwise from the positive x-axis and r is the absolute distance.

The L3 detector has been described with great detail in [4]. Therefore, only the components of the detector used in this analysis will be mentioned in the following sections.

3.1 Time Expansion Chamber

The time expansion chamber (TEC) [28] is the principle subdetector responsible for the following:

- the precise measurement of the location and direction of the charged particles tracks,
- the measurement of the transverse momentum and the sign of the charge for particles up to 50 GeV,
- the reconstruction of the primary vertex and the secondary vertices for particles with lifetimes greater than 10^{-13} s,
- the reconstruction of the impact point and the direction of charged particles as they enter the electromagnetic calorimeter.

The TEC, shown in Figure 3.4, is composed of two concentric cylindrical drift chambers with common end plates. The inner chamber is divided into

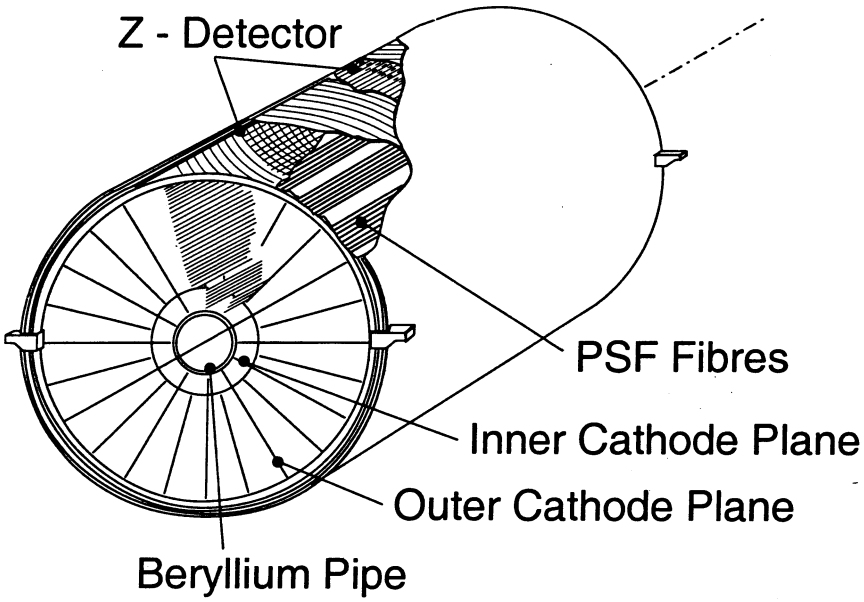

Figure 3.4: A perspective view of the TEC.

12 sectors in ϕ where each sector contains 8 anode wires. The outer chamber has 24 sectors, each with 54 anode wires. The wires are 98.2 cm in length and aligned parallel to the beam. The sectors are separated from each other by cathode planes. The anode plane is located in the middle of each sector. Figure 3.5 shows an inner sector and the associated outer sectors of the TEC.

The chamber is filled with a low diffusion 80% CO_2 and 20% isobutane gas mixture at a pressure of 1.2 bar and a temperature of 291 K. A charged particle ionizes the gas as it passes through the wire chamber. The electrons drift at a velocity of 6 μm/ns in a homogeneous electric field of 0.9 kV/cm towards the nearest anode wire which produces a signal, or *hit*, at the given wire. Combining the inner and outer sectors, a maximum of 62 coordinate measurements are possible for a single track. Track momenta are calculated

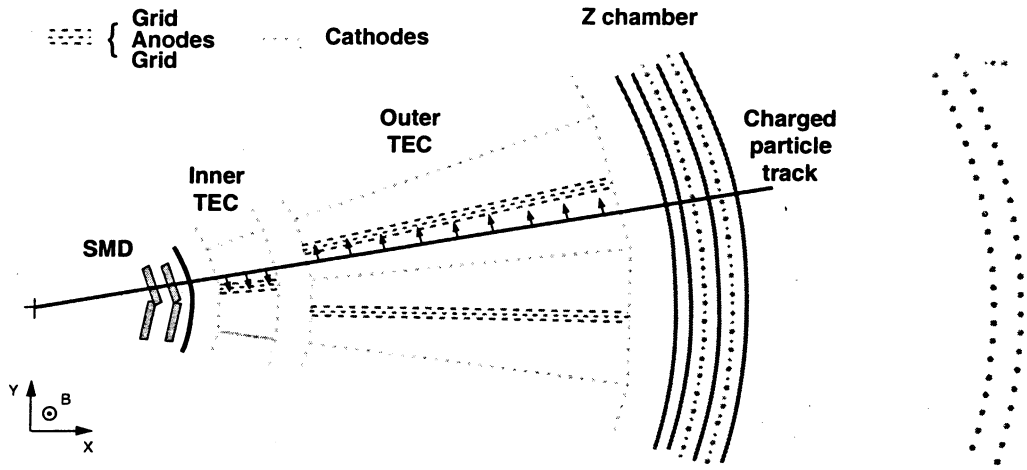

Figure 3.5: Wire configuration in one inner TEC sector and in part of two outer sectors.

from the bending of the tracks in the $r - \phi$ plane. The maximum radial length inside the TEC volume is 31.7 cm. For a polar angle of $\theta < 42°$, the number of wires available for track measurement decreases linearly with tan θ as dn/d(tan θ) $\approx$ 91.

The average single wire resolution of a charged track measurement is 50 μm. The resolution of the transverse momentum is $\sigma(p_T)/p_T^2 = 0.022$ $(GeV)^{-1}$.

3.2 Electromagnetic Calorimeter

The electromagnetic calorimeter (ECAL) is subdivided into two symmetric half-barrels and endcaps (Figure 3.6), which surround the TEC. The barrel part covers the angular region of $42° < \theta < 138°$. The endcaps extend this angular coverage to $11° < \theta < 38°$ and $142° < \theta < 169°$. The ECAL consists of about 11000 bismuth germanium oxide (BGO) scintillating crystals which are used as both the showering and detecting medium. This material

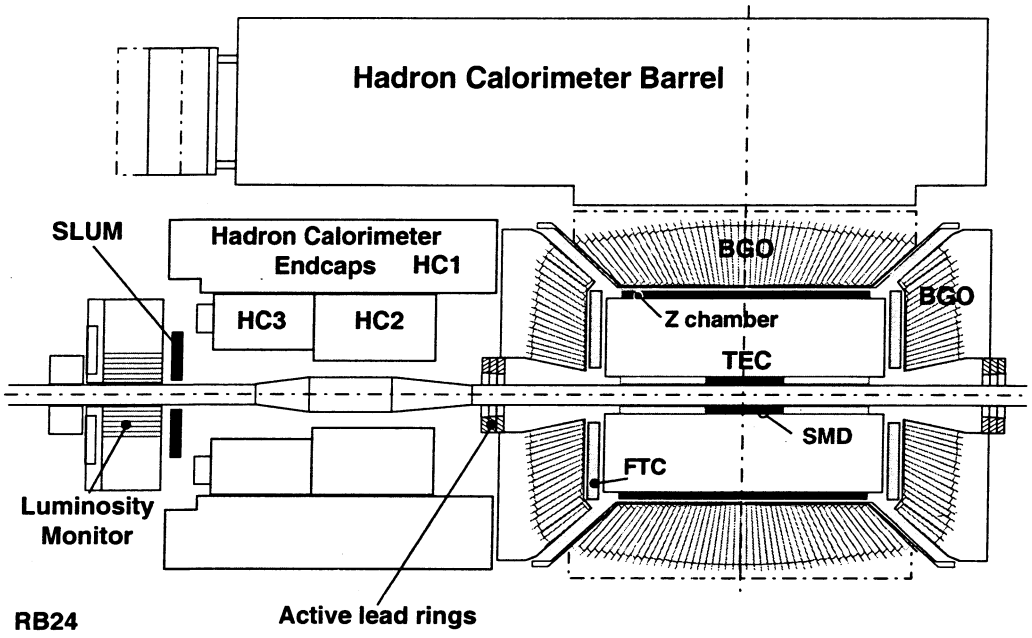

Figure 3.6: A side view of central part of the L3 detector.

was chosen for the high stopping power (short radiation length) for photons and electrons, and for the large nuclear interaction length for hadrons (Table 3.1). Also, BGO is highly efficient in converting the particle energy loss into photons.

The crystals have the shape of a truncated pyramid with a front face of 2 cm x 2 cm and a rear face of 3 cm x 3 cm (Figure 3.7). The crystal is 24 cm long which corresponds to 21 radiation lengths. The crystals are tapered, and their axes point towards the interaction region with a small angular offset to avoid cracks in the detector. The polished crystals are coated with a 50 μm thick layer of high reflectivity paint to ensure uniform light collection efficiency.

Table 3.1: Properties of a BGO crystal.

Density	7.13 g/cm^3
Radiation length	1.12 cm
Interaction length	22 cm
Peak emission wavelength	480 nm
Light yield	8000 γ/MeV
Decay time	300 ns

Two sillicon photodiodes detect the scintillation light from the rear face of the BGO crystals. The diodes are insensitive to the magnetic field of 0.5 Tesla inside the magnet. A charge sensitive amplifier is mounted directly behind each crystal. The design of the analog-to-digital converter (ADC) gives an accurate signal measurement over a wide range from 100 MeV to 100 GeV, and has a short memory time so the tails from large signals do not mimic small signals in later beam crossings.

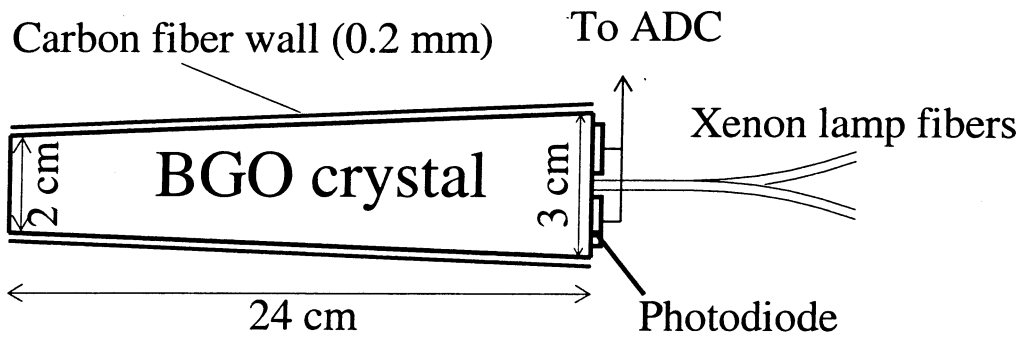

Figure 3.7: A BGO crystal.

The ECAL resolution, σ_E/E, for electrons and photons, is about 5% at 100 MeV, is less than 2% at 2 GeV and improves to about 1.2% at 45 GeV. The position resolution is about 1 mm corresponding to an angular resolution of about 2 mrad for electromagnetic showers at 45 GeV.

3.3 Hadron Calorimeter

The hadron calorimeter (HCAL) [29] is a fine sampling calorimeter made of proportional wire chambers (80% Ar + 20% CO_2) interleaved with depleted uranium absorber plates. The HCAL measures the energy and positions of hadrons. It also stops all showering particles before they enter the precision muon detector. Uranium was chosen because it has a short nuclear interaction length of about 11 cm.

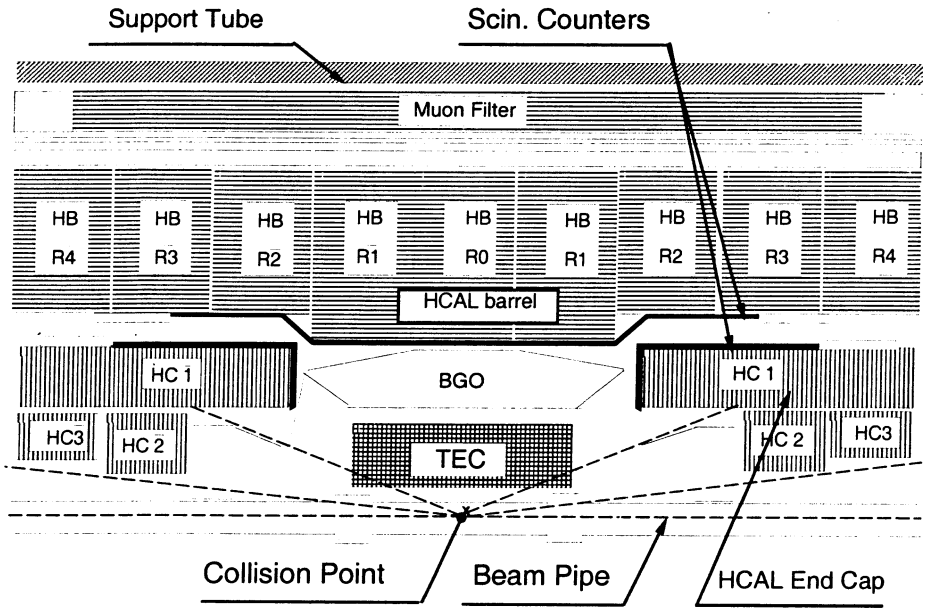

Figure 3.8: R-z view of the L3 hadron calorimeter.

The HCAL is divided into a barrel and encap part. The barrel HCAL consists of 9 rings along the z-axis (Figure 3.8). Each ring has 16 modules providing complete coverage in the azimuthal angle, ϕ. The barrel is 4725 mm long with an outer radius of 1795 mm and an inner radius of 886 mm for the three inner rings and 979 mm for the outer rings. The endcap HCAL consists of three separate rings. Combined, the barrel and endcaps cover 99.5% of the solid angle.

The energy resolution for hadrons in the HCAL can be parametrized by Eq. 3.2:

$$\frac{\Delta E}{E} = \left(5 + \frac{55}{\sqrt{E\ (GeV)}}\right). \tag{3.2}$$

By combining information from the ECAL and HCAL, a total energy resolution of about 10% is obtained for charged pions with energy greater than 15 GeV. The angular resolution for jets is about 2.5°.

3.4 Muon Chamber

The muon chamber [30] has a barrel and forward-backward component which resides outside the support tube. The barrel muon chamber consists of two *ferris wheels* which are each made up of eight octants (Figure 3.3). Each octant has five precision (P) drift chambers (Figure 3.9): two chambers (MO) in the outer layer each with 16 wires layer, two chambers (MM) in the middle layer each with 24 wires and one inner chamber (MI) with 16 wires. The wires of the P chambers are parallel to the beam axis and measure the x and y coordinates of the tracks. The top and bottom of the MI and MO chambers are covered by six drift chambers (Z chambers) to measure the z

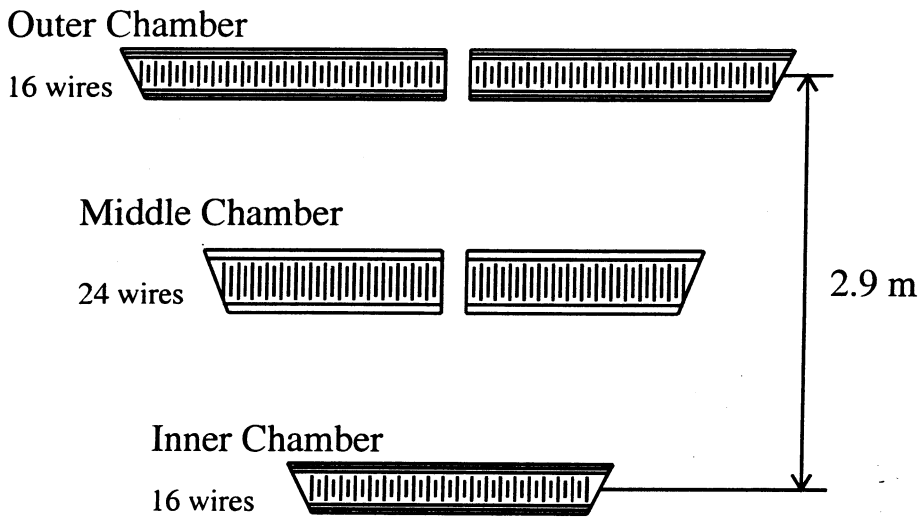

Figure 3.9: View of an octant of the muon detector with its five chambers.

coordinate along the beam. The muon transverse momentum is extracted from the sagitta of the track (Figure 3.10).

The polar angular coverage with all three layers of the P chambers is $44° < \theta < 136°$ which corresponds to 65% of the solid angle. The single wire resolution of the P chambers is 200 μm which translates to an error of $\sigma(p_T)/p_T \sim 2.5\%$ on the measurement of a 45 GeV muon. The resolution on the Z chambers is about 500 μm.

The forward and backward muon chambers [31] are mounted on the magnet doors. On each side there are three layers each of which contain 16 drift chambers (Figure 3.11). The polar angle coverage is extended to $22° < \theta < 44°$ and $136° < \theta < 158°$. In the angular range $36° < \theta < 44°$, the muon momentum is measured with the MI an MM barrel chambers and with

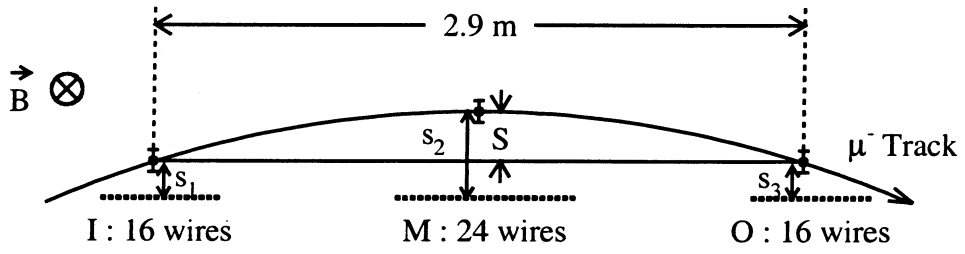

Figure 3.10: Sagitta of a muon track

one inner F/B chamber by using the curvature in the solenoidal magnetic field. In the angular range $22° < \theta < 36°$, the momentum is measured using the curvature of the toroidal magnetic field in the three layers of the F/B muon chambers. The momentum resolution degrades quickly, from 2 to 20%, with decreasing θ primarily due to the multiple scattering in the 1 m thick magnet doors.

3.5 Luminosity Monitor

The luminosity monitor [32] is designed to detect electrons and photons at very small angles and to determine the energy and scattering angles with a high degree of accuracy. The luminosity monitor consists of two detectors located at a distance of 265 cm on either side of the interaction point. Figure 3.6 shows the position of one of the luminosity monitors with respect to the other subdetectors. Each detector has a calorimeter made of BGO crystals, which provides an energy resolution of 2% at 45 GeV, and a tracker made of silicon wafers which have an intrinsic geometrical precision of 1-2 μm. The luminosity monitor covers the polar angle region of 25 mrad $< \theta <$ 70 mrad.

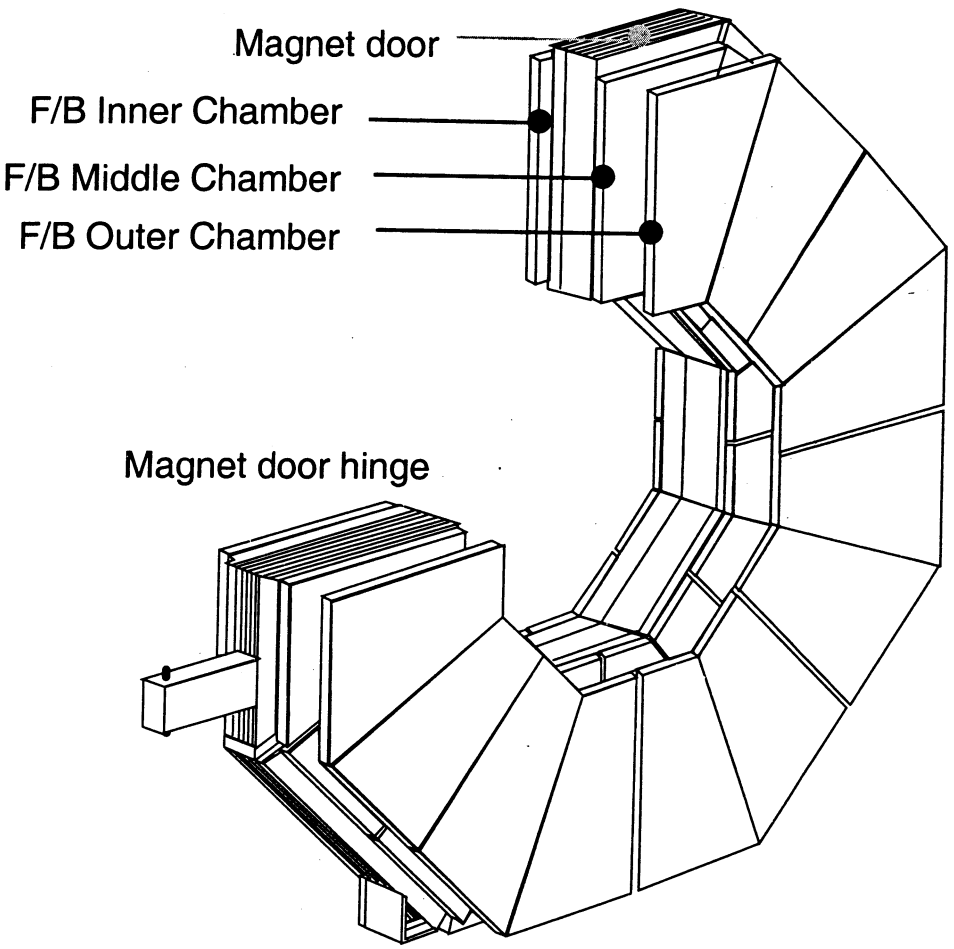

Figure 3.11: View of the forward backward muon spectrometer.

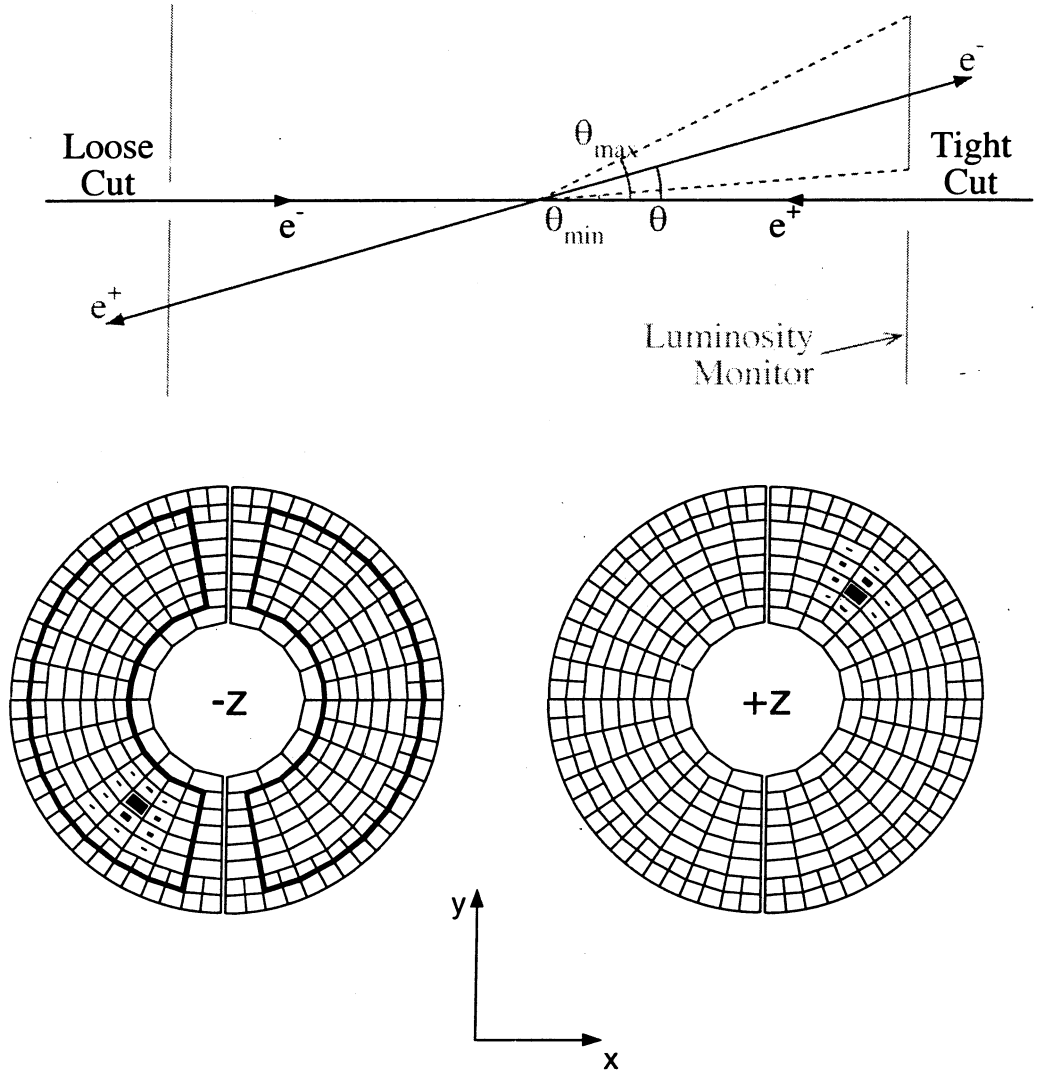

Figure 3.12: A Bhabha event in the luminosity monitor. There are two tracks which are back-to-back. The energy detected by the BGO crystals is represented by squares which are proportional to the amount of energy deposited.

As mentioned in the first chapter of this thesis, the luminosity monitor is very important in determining the integrated luminosity. Bhahba events are selected using the calorimetric measurement in the BGO to provide a sample of events free of background. A typical Bhabha event shows two energy deposits of $\sqrt{s}/2$ back-to-back in the luminosity monitor (Figure 3.12).

The luminosity monitor also detects the scattered electrons in two-photon events with high photon virtuality. At $\sqrt{s} = 183$ GeV, the Q^2 range corresponding to electrons scattered into the luminosity monitor is 8-30 GeV^2.

CHAPTER 4

L3 DATA TRIGGERING, RECONSTRUCTION AND SIMULATION

4.1 L3 Trigger System

The L3 trigger system [33] attempts to record all of the interesting physics interactions while at the same time rejecting background events, e.g., beam-gas, beam-wall, cosmic rays, etc. The beam crossing rate is about 45 KHz for the four bunch operations at LEP. With luminosities of 10^{31} $cm^{-2}s^{-1}$, the standard physics processes occur at a signal rate of about 1 Hz. Therefore, a 3-level trigger system is needed to reduce the 45 KHz of information to a signal rate of a few Hz which can be recorded to tape. This minimizes the dead time due to the data acquisition. A schematic of the L3 online trigger system is shown in Figure 4.1.

4.1.1 Level 1 Trigger

The first level trigger is made up of independent triggers for the calorimeters, the central tracking chamber, the muon chambers, the scintillation counters and the luminosity monitor. Each of the individual triggers must make a decision to accept or reject an event within a maximum of 22 μs before the next beam crossing. After each beam crossing, the information from all the subdetectors is read by the front end electronics. If a negative decision is made by the first level trigger, the trigger data in the front end electronics is cleared so as not to contribute to the dead time. If a positive decision is made by more than one of the individual triggers, the event is passed by the

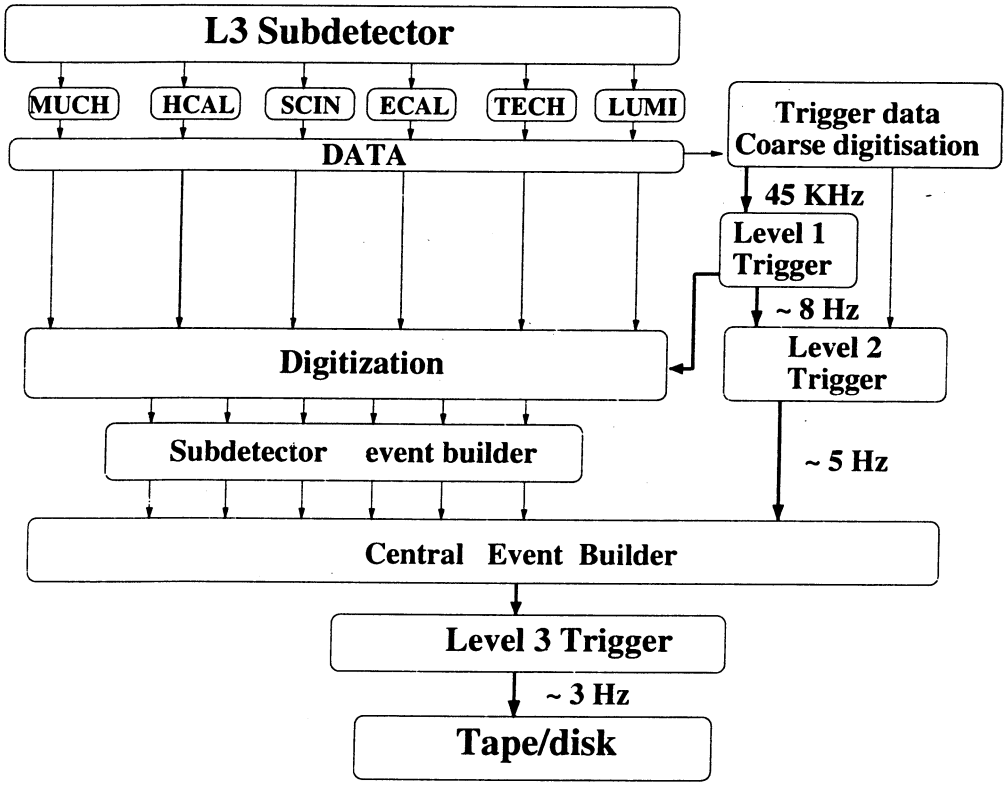

Figure 4.1: L3 online trigger system.

level 2 and level 3 triggers. The detector data is digitized and then stored into multi-event buffers. The combined rate of the first level trigger is about 8 Hz, with a dead time incurred from the digitization of less than 5%.

1. Calorimetric Trigger

   The first level calorimetric trigger [34] accepts events which deposit a specific amount of energy in the calorimeters. The input is the sum of the energy of several BGO crystals or HCAL towers. The event is selected if at least one of the following conditions is satisfied:

   - the ECAL energy is greater than 25 GeV in the barrel and endcaps,
   - the ECAL energy is greater than 8 GeV in the barrel alone,
   - the total calorimetric energy exceeds 25 GeV in the barrel and endcaps, or
   - the total calorimetric energy in the barrel exceeds 15 GeV.

   The typical trigger rate is 1-2 Hz.

2. TEC Trigger

   The TEC trigger [35] selects events with charged tracks. The TEC trigger is affected by background processes like beam-gas and synchrotron radiation. The rate of these background triggers decreases rapidly with distance from the beam pipe. Therefore, the inner TEC sectors are not included in the TEC trigger. The input is the hit pattern from the anode wires spread radially in the 24 outer TEC sectors. The transverse

momentum threshold is 150 MeV. Only events which have at least two tracks with an acoplanarity angle[1] less than 60° are selected. The TEC trigger rate varies between 1 to 4 Hz depending on the beam conditions. The efficiency of the trigger for real Bhabha events is greater than 99.5%, where the electrons are scattered into the barrel region of the calorimeter.

3. Muon Trigger

   The muon trigger [36] selects events where at least one charged particle penetrates the muon chambers. Measurements should be available from at least 2 P-layers and 1 Z-layer. The track must have a transverse momentum greater than 1 GeV. The trigger rate is about 10 Hz dominated by cosmic ray background. By requiring in coincidence one good hit from the scintillators, the rate is reduced to less than 1 Hz.

4. Luminosity Trigger

   The input to the luminosity trigger is the sum of the energies from the luminosity monitor. The detector is divided into 16 ϕ sectors on either side of the interaction point. Bhabha events are triggered if any of the following three threshold conditions are met:

   - two back-to-back energy depositions of energy greater than 15 GeV,
   - a total energy on one side greater than 25 GeV and on the other side greater than 5 GeV, or

[1] Acoplanarity $= \pi - \min(|\phi_2 - \phi_1|, 2\pi - |\phi_2 - \phi_1|)$

- a total energy on either side greater than 30 GeV.

The trigger rate is highly dependent on the delivered luminosity, and it can increase in bad beam conditions.

4.1.2 Level 2 Trigger

In contrast to the level 1 trigger which selects interesting physics events, the level 2 trigger [37] attempts to reject background events. The inputs to the second level trigger include:

- the coarse data used for the level 1 trigger,
- the results from the level 1 trigger, and
- information from the combined clusters and jets from the calorimeters and the loosely reconstructed tracks.

Because the information is read from the memory buffer and not from the front end electronics, the second level trigger spends more time per event (about 8 ms) to correlate the subdetector signals without incurring additional dead time. This is effective in removing the calorimetric triggers from electronic noise and the TEC triggers from beam-gas and beam-wall interactions and from synchrotron radiation. The input data is then passed to an event builder memory. If the level 2 result is positive, the event builder collates the data and transfers it to the level 3 trigger. If the result is negative, the event builder is reset. The second level trigger rejects from 20 to 30% of the events passed by a first level trigger. The total rate for level 2 is less than 6 Hz.

4.1.3 Level 3 Trigger

The third level trigger [38] performs a complete reconstruction of the event. Although the method is similar to the second level, the digitized data has finer granularity and better resolution. Several algorithms are used to examine the event. The specific algorithm is dependent on the level 1 trigger which selected the event (calorimeter, TEC, muon or luminosity). If more than one trigger at level 1 selected the event, it passes through both level 2 and level 3 unhindered. The calorimetric algorithm recalculates and calibrates the energies. Luminosity triggered events pass through untouched by the third level. The muon tracks are reconstructed and a more stringent coincidence of 10 ns is applied. The reconstructed TEC tracks are correlated with at least 100 MeV of energy in the calorimeters and also examined for quality and a common vertex. The combined algorithms reduce the rate to about 2-3 Hz. The events are analyzed in a time of less than 100 ms to prevent additional dead time. The output from a positive third level trigger is transferred to a memory buffer on the main online computer, and then written to tape.

4.2 Event Reconstruction

The event reconstruction program REL3 [39] converts raw digitized detector signals (either real or simulated) into physically meaningful observables. REL3 first reconstructs the objects in the subdetectors, e.g., energy clusters in the calorimeters or tracks in the TEC and muon chambers, then combines the objects in order to reconstruct particles and events. The detector signals arising from the real e^+e^- interactions and the simualated data are recon-

structed using the same REL3 program. The reconstructed objects used in this analysis are described in the following subsections.

4.2.1 Tracks

Hits in the central tracking chamber are combined to map the trajectory of charged particles in the detector. The curvature of the trajectory is used to measure the transverse momentum and the sign of the charge of the particle. The main parameters of a track are:

- the number of wires hit by the track (maximum of 62 in the TEC),
- the distance of closest approach (DCA) of the track, in the $r-\phi$ plane, to the interaction vertex,
- the transverse momentum, p_t,
- the span of the track, defined as the distance between the first and last hit wire, and
- the polar and azimuthal angles of the track.

4.2.2 Bumps in the ECAL

The purpose of the reconstruction of objects in the ECAL is to determine the energies and the directions of the particles interacting with the BGO material. Also, the showers are classified as electromagnetic or hadronic, or they are a result of minimum ionizing particles (MIPs). The raw ADC signal from each crystal is converted into an energy value. Geometrical clusters are formed by combining adjacent crystals with an energy greater than 10 MeV into groups. Each cluster must have a total energy of more than 40 MeV.

The next step is to identify energy deposits within a geometrical cluster that are characteristic of single particles. The local maxima, which are crystals with an energy deposition of more than 40 MeV, are referred to as bump crystals. Each non-bump crystal ($10 < E_{crystal} < 40$) is then associated to the nearest bump crystal. In the case there is more than one equidistant bump crystal, the non-bump crystal is assigned to the most energetic one. The combination of the bump crystal with all the associated neighbors is referred to as a *bump*.

For each bump, the center of gravity and the sums of the energies deposited in the 3×3 (E_9) and 5×5 (E_{25}) crystal matrix are constructed. After these sums are corrected for lateral energy loss, the ratio of E_9/E_{25} can be used to discriminate electromagnetic and hadronic particles. Similarly, the variable χ^2_{em} is the comparison between the event energy distribution deposited in a 3×3 crystal matrix and the expected distribution for an electromagnetic particle.

The main parameters used to describe a bump are:

- the number of crystals ($E_{crystal} > 10$ MeV) in the bump,
- the total energy in the bump,
- the most energetic crystal energy in the bump (E_1),
- E_9 and E_{25} crystal matrices around the bump crystal,
- χ^2_{em} of the shower shape fit assuming the bump to be of electromagnetic origin, and

- the polar and azimuthal angles of the bump crystal.

4.2.3 Clusters in the HCAL

Reconstruction of the clusters in the HCAL begins with the individual tower signals. A tower is accepted only if its energy deposit is greater than 9 MeV. The condition removes most of the uranium noise. The towers are then grouped into clusters using sophisticated pattern recognition algorithms, which can discriminate between clusters originating from interacting hadrons and clusters resulting from minimum ionizing muons. The energy deposition from a transversing muon is localized near its track.

4.2.4 Muons

Muons are identified in the muon chambers. A muon candidate is a track reconstructed with at least two P segments and one Z segment. The hits from the MUCH are fitted together with the hits from the central tracking chamber to form a higher class object, called AMUI, which represents a muon coming from the vertex interaction. The distance between the AMUI an the vertex interaction is called the DCA. The relevant parameters for a muon track are:

- the number of P and Z segments for track fitting,
- the momentum of the track,
- the polar coordinates,
- the DCA, and
- the time-of-flight measured by the scintillators.

4.3 Monte Carlo Simulation

Much of the understanding of physics is gained through a detailed Monte Carlo simulation of relevant physics processes. The detector response to the particle final states is learned through simulation. The selection criteria of a physics analysis can be optimized with a Monte Carlo. The systematic errors for a given measurement are accurately estimated through the comparison of the Monte Carlo to the data. In L3, the Monte Carlo is processed in two steps.

1. *Event generation.* Events are generated with a distribution according to the physics of interest.

2. *Detector simulation.* The generated particles are traced through the detailed representation of the detector, and the response of each active element is simulated.

4.3.1 Event Generation

Various event generators are used to generate events for different physics processes. In this analysis, the PYTHIA 5.7 [21] Monte Carlo is used to simulate two-photon signal events according to the current knowledge of hadronic interactions obtained by pp and γp studies. The two-photon processes are generated with massless ($m_q = 0$) matrix elements [40]. The resolved process uses the SaS1d photon structure function [24]. We have implemented the two-photon luminosity function in the equivalent photon approximation (EPA) which has a cut-off of $Q^2 < m_\rho^2$ [22].

Background sources include the two-photon process $e^+e^- \rightarrow e^+e^-\tau^+\tau^-$ simulated with the JAMVG [41] Monte Carlo generator and the annihilation processes $e^+e^- \rightarrow Z/\gamma \rightarrow q\bar{q}$, simulated with JETSET 7.3 [42] at $\sqrt{s} = 91$ GeV and with PYTHIA 5.7 [21] at energies above the Z mass. The process $e^+e^- \rightarrow \tau^+\tau^-$ is simulated with KORALZ [43], and, at higher energies, $e^+e^- \rightarrow W^+W^-$ with KORALW [44].

4.3.2 Detector Simulation

The L3 detector simulation program (SIL3) defines the geometry of all the subdetectors to an accuracy of 10-100 μm, along with the properties of the subdetector materials and the magnetic field. The GEANT3 [45] program provides elaborate simulation of all physical processes and interactions of the particles with matter such as decay, ionization loss, multiple scattering, photoproduction, δ-ray production, bremsstrahlung, etc. The hadronic interaction processes are simulated by the GHEISHA [46] program.

There is an uncertainty on the interaction vertex due to the finite dimension of the beam bunches. Therefore, SIL3 redefines the interaction point position to reproduce the same distributions observed in the data. Hits in the TEC and the MUCH are simulated using the time-to-distance relation measured in the test beam data [47]. The step size for particle tracking, the medium dependent energy cut-off values, the non-uniformity and saturation in light yield and the electronic noise in the ECAL and HCAL are fine-tuned in the simulations. The effects of temperature, pressure, noise and cross-talk are simulated. The scintillator ADC and TDC information is simulated to correct for light attenuation, for the particle time-of-flight and for the time

slewing due to varying pulse height. The full simulation of particle production and energy deposition is finally converted to the same electronic signal format as the real data.

4.4 Monte Carlo Reconstruction

The simulated data is passed through the same REL3 reconstruction program as the raw data recorded by the L3 detector. In reality, the ideal detector simulation does not exist. Dead or noisy BGO crystals, defective towers in the HCAL, disconnected sectors, inefficient wires in the TEC or MUCH, a burned-out PMT, etc. can contribute to a deterioration over time of the detector resolution. Therefore, the information of the status and the calibration of the detector is stored in the L3 database [48] for a given time period. When the simulated data is reconstructed, the appropriate information can be retrieved from the database and certain inefficiencies or calibrations will be applied. This procedure is called the *real detector MC simulation.*

CHAPTER 5

ANALYSIS

Inclusive charm events in two-photon interactions at e^+e^- collisions are produced in the reaction $e^+e^- \rightarrow e^+e^-c\bar{c}X$. The scattered electrons are not detected in this analysis. The X refers to the remnant jet in the case of resolved processes, or X is due to gluon emission and subsequent fragmentation to a hadron jet in the case of the direct or resolved next-to-leading order QCD corrections. The reactions of $\gamma\gamma \rightarrow c\bar{c}$ and $\gamma g \rightarrow c\bar{c}$ produce open charm which is very unstable and will decay spontaneously into a strange (anti-strange) quark through a virtual W boson exchange.

The strategy used in this analysis to select two-photon inclusive charm events is to tag the semileptonic decay of the charm quark. The semileptonic decay follows through the reaction:

$$\begin{array}{rcl} c & \rightarrow & s \;\; W^* \\ & & \hookrightarrow \ell + \nu \end{array} \tag{5.1}$$

where W* is a virtual W vector boson. The strange quark will go through fragmentation producing a hadronic jet. The virtual W will decay into an electron or muon and its associated neutrino which will not be detected. The average charm semileptonic branching ratio is 0.098 [49]. The other charm quark may decay hadronically, $c \rightarrow s\ W^* \rightarrow s\ q\bar{q}$, or semileptonically, in both cases producing another jet of hadrons. Although the charm quark is heavy in comparison to the light quarks (u,d,s), it is light in comparison to its

momentum. Therefore, the strange quark, lepton and neutrino are produced with a relatively small opening angle in the same general direction.

First, hadronic two-photon events are selected, and then the charm events are identified by tagging an electron or muon. The hadronic two-photon data sample is comprised mostly of hadrons made up of light quarks, *u, d* and *s*. The most common electron decay mode for non-charm hadrons is the reaction $\pi^0 \rightarrow e^+e^-\gamma$ which has a branching ratio of 1.2%. Although the non-charm hadron decays have small branching fractions for electrons, they are a very copious source of electrons because each hadronic event has several π^0s, and because $\sigma(\gamma\gamma \rightarrow q\bar{q}$, where q = u, d and s) $\gg \sigma(\gamma\gamma \rightarrow c\bar{c})$. However, the electrons (and muons) produced from semileptonic decay of charm quark hadrons are more energetic.

5.1 Hadronic Two-Photon Events Selection

In the reaction $e^+e^- \rightarrow e^+e^-$ *hadrons*, most of the center-of-mass energy is carried away by the scattered electrons. If $Q^2 \simeq 0$, the scattering angle is close to the beam and the electrons go undetected. At high values of $\sqrt{s}$, the visible energy of the detected hadron system is well separated from that of the e^+e^- annihilation processes: $e^+e^- \rightarrow q\bar{q}$ and, for $\sqrt{s} > 161$ GeV, also $e^+e^- \rightarrow W^+W^-$. The signal hadronic two-photon events have a large track multiplicity and can be distinguished from other background processes such as $e^+e^- \rightarrow \ell^+\ell^-$ and $e^+e^- \rightarrow e^+e^-\ell^+\ell^-$ ($\ell = e, \mu, \tau$), which have a smaller track multiplicity, typically ≤ 4.

Hadronic two-photon events are selected by placing cuts on the visible energy, the visible mass and the track multiplicity (Table 5.1). Also, a cut is

Table 5.1: Hadronic cut selection.

Event Variable	Cut Threshold
W_{vis}	> 3 GeV
E_{vis}	$< 0.38\sqrt{s}$
N_{tracks}	≥ 5
E_{Lumi}	$< 0.40\ E_{Beam}$

made on the energy in the luminosity monitor in order to require an anti-tag condition. Both scattered electrons continue down the beam pipe undetected, and the photons have a small virtuality. For each plot in this section, all hadronic cuts have been applied to the data and the Monte Carlo except for the variable being shown. The variable distributions shown in this matter are called *N-1* plots. They are useful for demonstrating the effectiveness of each cut individually and for showing agreement between data and Monte Carlo at different stages. The Monte Carlo prediction is normalized to the data luminosity and corrected for the trigger efficiency. This normalization is applied to both the Monte Carlo signal and background.

The visible mass, W_{vis}, of the event is calculated from the four-momentum vectors of the measured calorimetric clusters. The data is well described by the simulation (Figures 5.1a-b and 5.2a-b) except for the normalization in the first two bins because the Monte Carlo signal events are generated in PYTHIA with a cut on the two-photon invariant mass at 3 GeV.

The visible energy, E_{vis}, is the sum of the energies measured in the electromagnetic and hadronic calorimeters and the energies of the muons measured in the muon chambers. All particles are considered to be pions except for

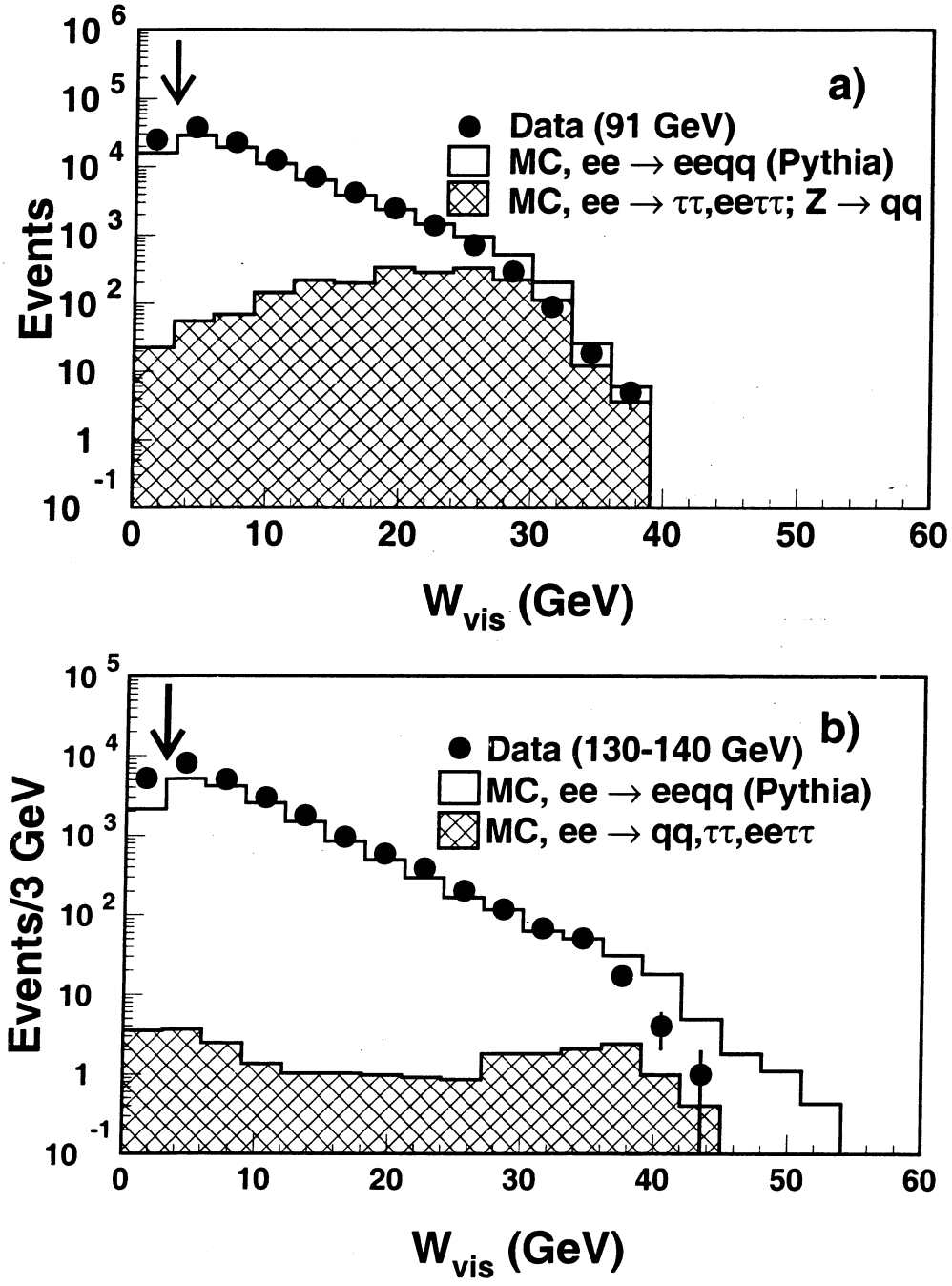

Figure 5.1: Invariant visible mass in the data at a) $\sqrt{s} = 91$ GeV and at b) $\sqrt{s} = 130 - 140$ GeV. Also shown are the Monte Carlo predictions for two-photon hadron production and the main backgrounds.

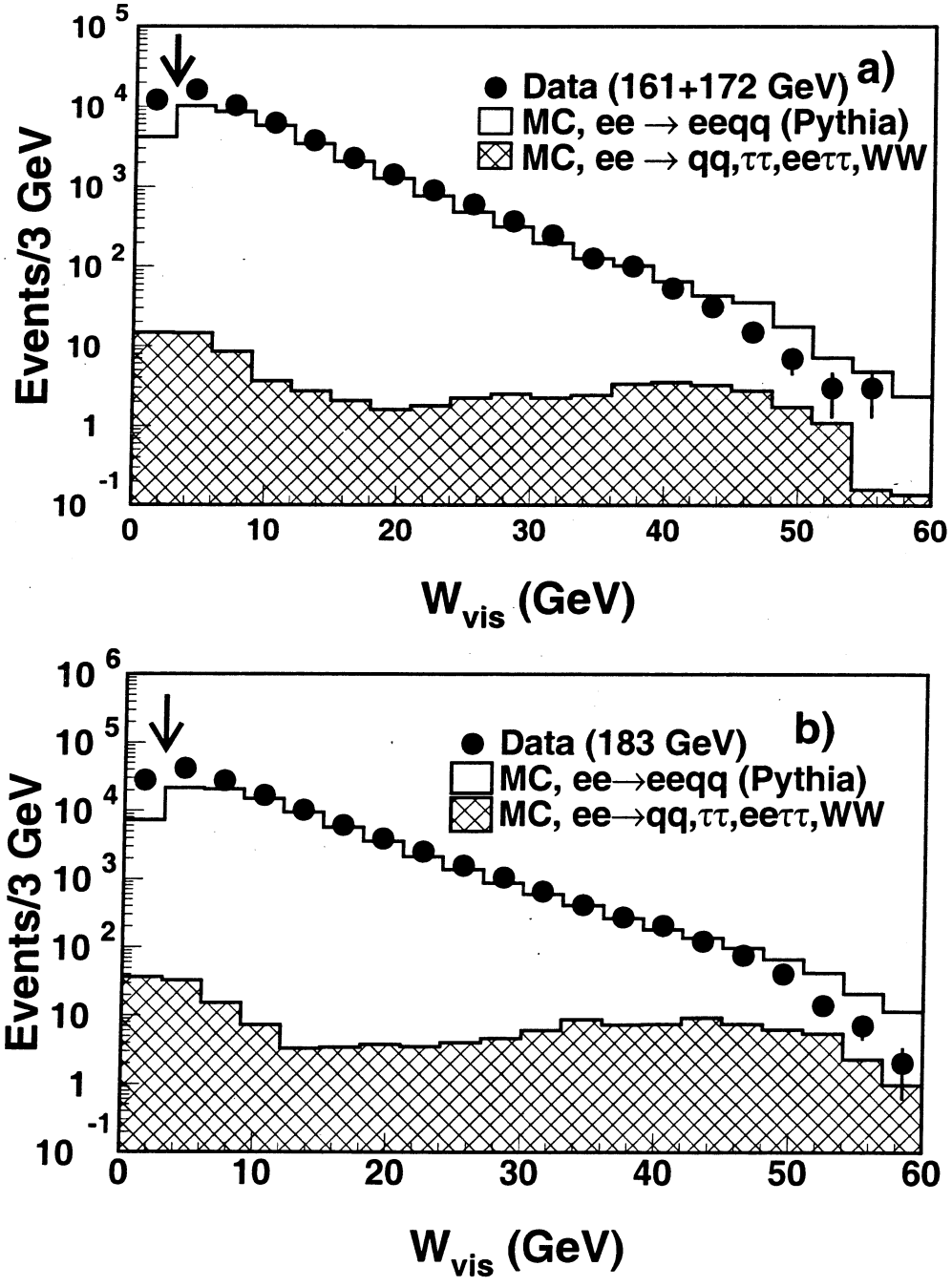

Figure 5.2: Invariant visible mass in the data at a) $\sqrt{s} = 161 - 172$ GeV and at b) $\sqrt{s} = 183$ GeV. Also shown are the Monte Carlo predictions for two-photon hadron production and the main backgrounds.

electromagnetic (EM) clusters identified as photons. The visible energy must be less than 0.38 $\sqrt{s}$. As one can see in Figures 5.3a-b and 5.4a-b, the cut on E_{vis} separates the two-photon processes from the annihilation processes which are characterized by a high visible energy. The data are reasonably well described by the simulation except for the normalization of the $\gamma\gamma \rightarrow$ *hadrons* contribution. Both the shape and the normalization of the annihilation background are well reproduced by the Monte Carlo, which is important when we later use the Monte Carlo estimate to subtract any remaining background from the data.

To suppress the background from $e^+e^- \rightarrow e^+e^-\tau^+\tau^-$ and $e^+e^- \rightarrow \tau^+\tau^-$ reactions, an event must have a track multiplicity of 5 or more. For this analysis, a *good* track must have:

- a transverse momentum, p_t, greater than 100 MeV,
- more than 15 wire hits in the tracking chamber (out of a possible 62),
- and a distance of closest approach (DCA) to the interaction vertex smaller than 5 mm.

The effect of the track multiplicity cut will be more clearly illustrated in Section 5.2 on the electron candidate selection.

The analysis is limited to anti-tagged events. Events are excluded when the most energetic cluster in the L3 luminosity monitor has an energy greater than 0.4 E_{Beam}. Thus the interacting photons are considered real or quasi-real: $\langle Q^2 \rangle \approx 0$ GeV^2, where $-Q^2$ is the invariant mass squared of the virtual photon. The choice of anti-tagged events in this analysis is in part due to the

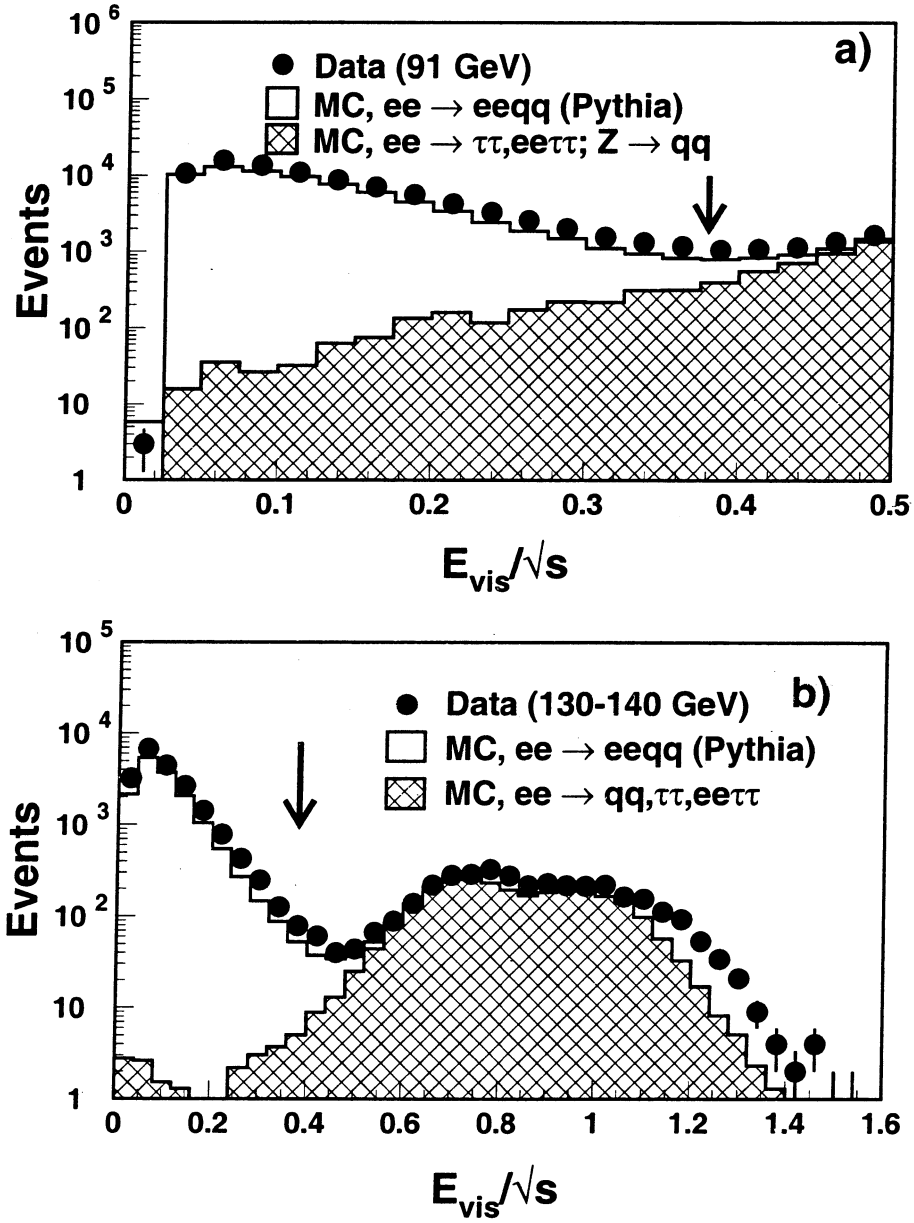

Figure 5.3: Total visible energy in the data at a) $\sqrt{s} = 91$ GeV and at b) $\sqrt{s} = 130 - 140$ GeV. Also shown are the Monte Carlo predictions for two-photon hadron production and the main backgrounds. A cut at $E_{vis} < 0.38\sqrt{s}$ removes most of the background coming from the annihilation channels. Because of the large Z decay background at $\sqrt{s} = 91$ GeV only the interval $E_{vis} < 0.5\sqrt{s}$ is shown in a).

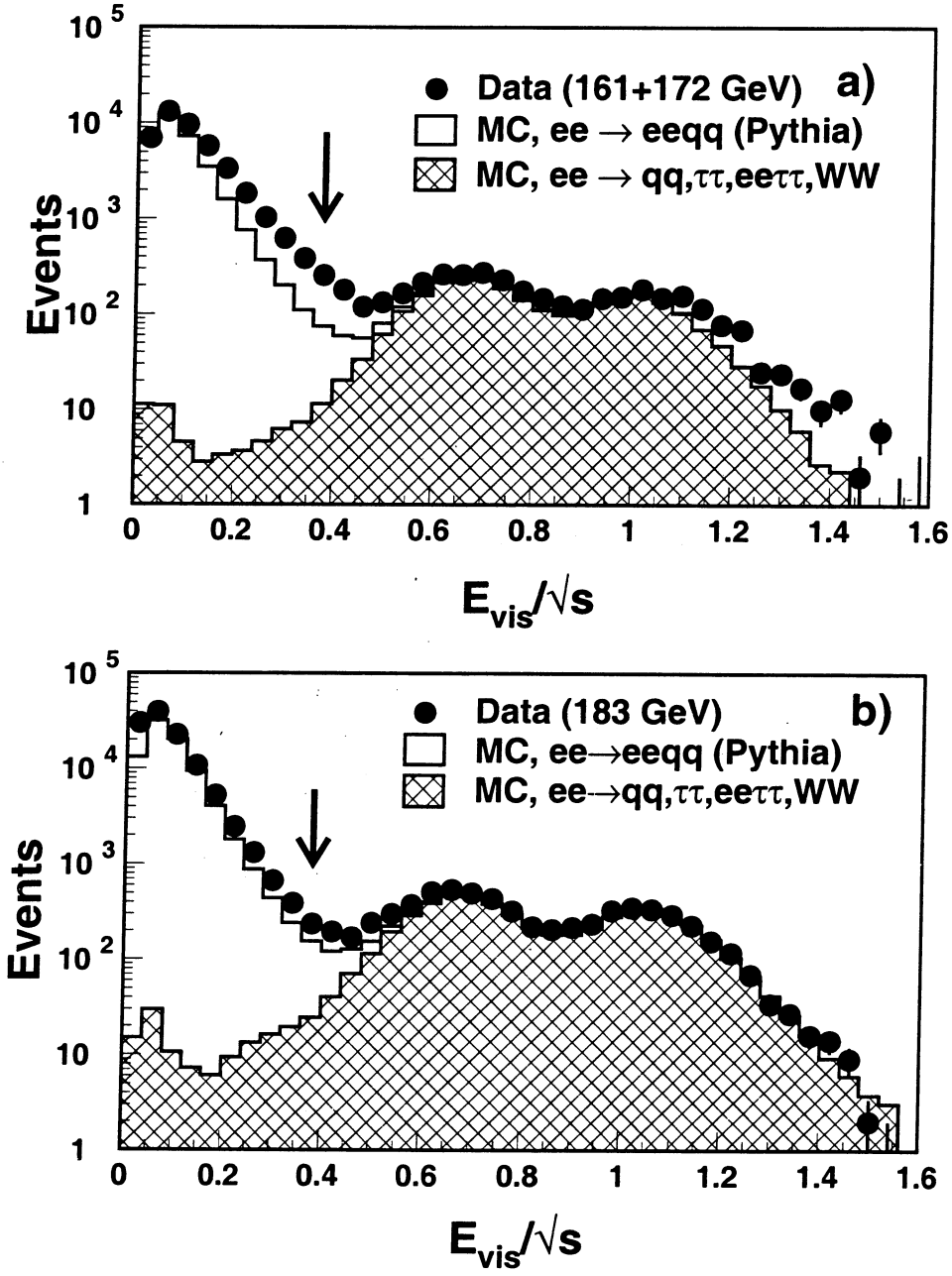

Figure 5.4: Total visible energy in the data at a) $\sqrt{s} = 161 - 172$ GeV and at b) $\sqrt{s} = 183$ GeV. Also shown are the Monte Carlo predictions for two-photon hadron production and the main backgrounds. A cut at $E_{vis} < 0.38\sqrt{s}$ removes most of the background coming from the annihilation channels.

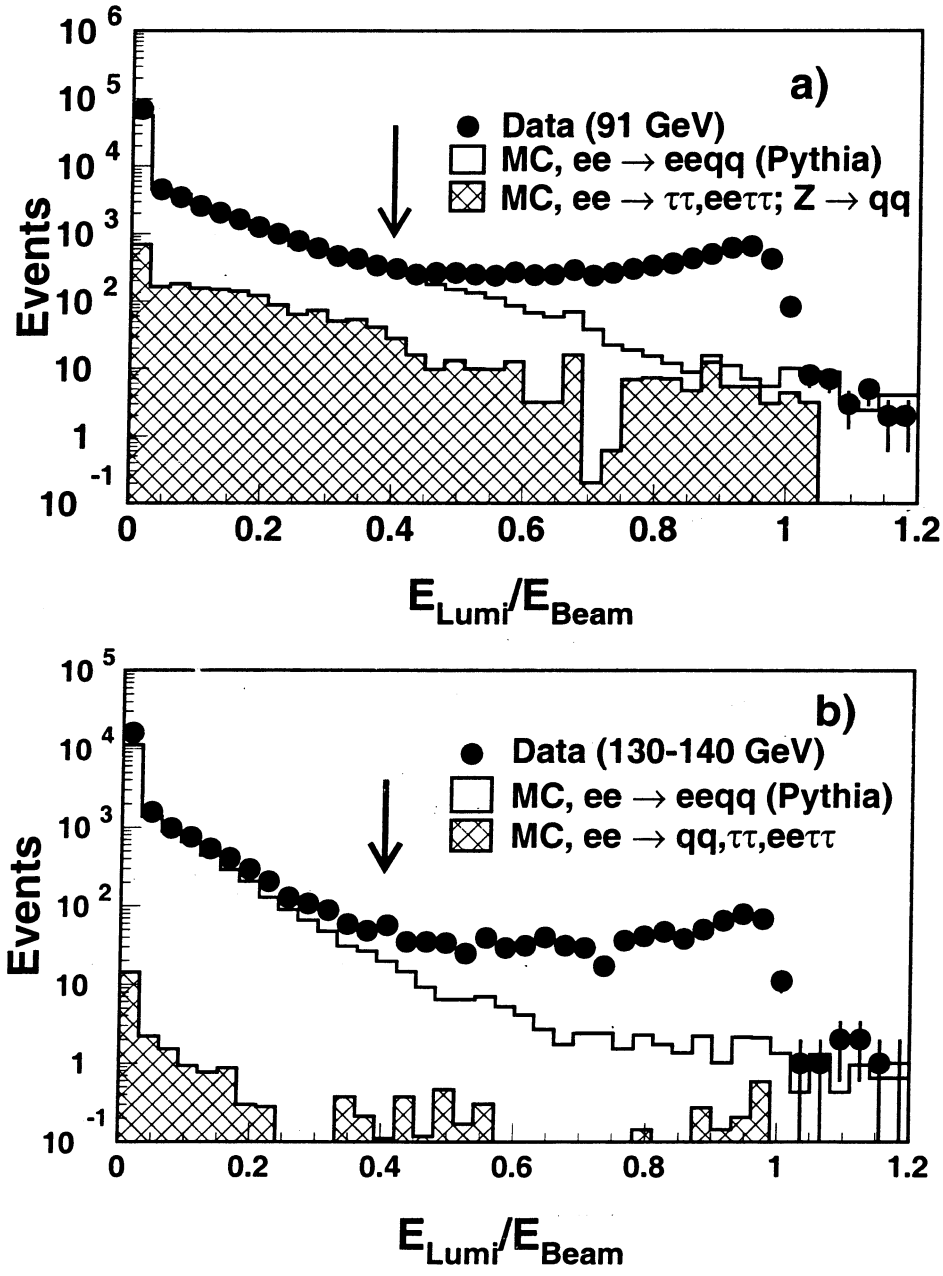

Figure 5.5: Ratio of the energy of the most energetic cluster in the luminosity monitor to the beam energy in the data at a) $\sqrt{s} = 91$ GeV and at b) $\sqrt{s} = 130 - 140$ GeV. Also shown are the Monte Carlo predictions for two-photon hadron production and the main backgrounds. A cut at $E_{Lumi} < 0.40\ E_{Beam}$ selects anti-tagged events.

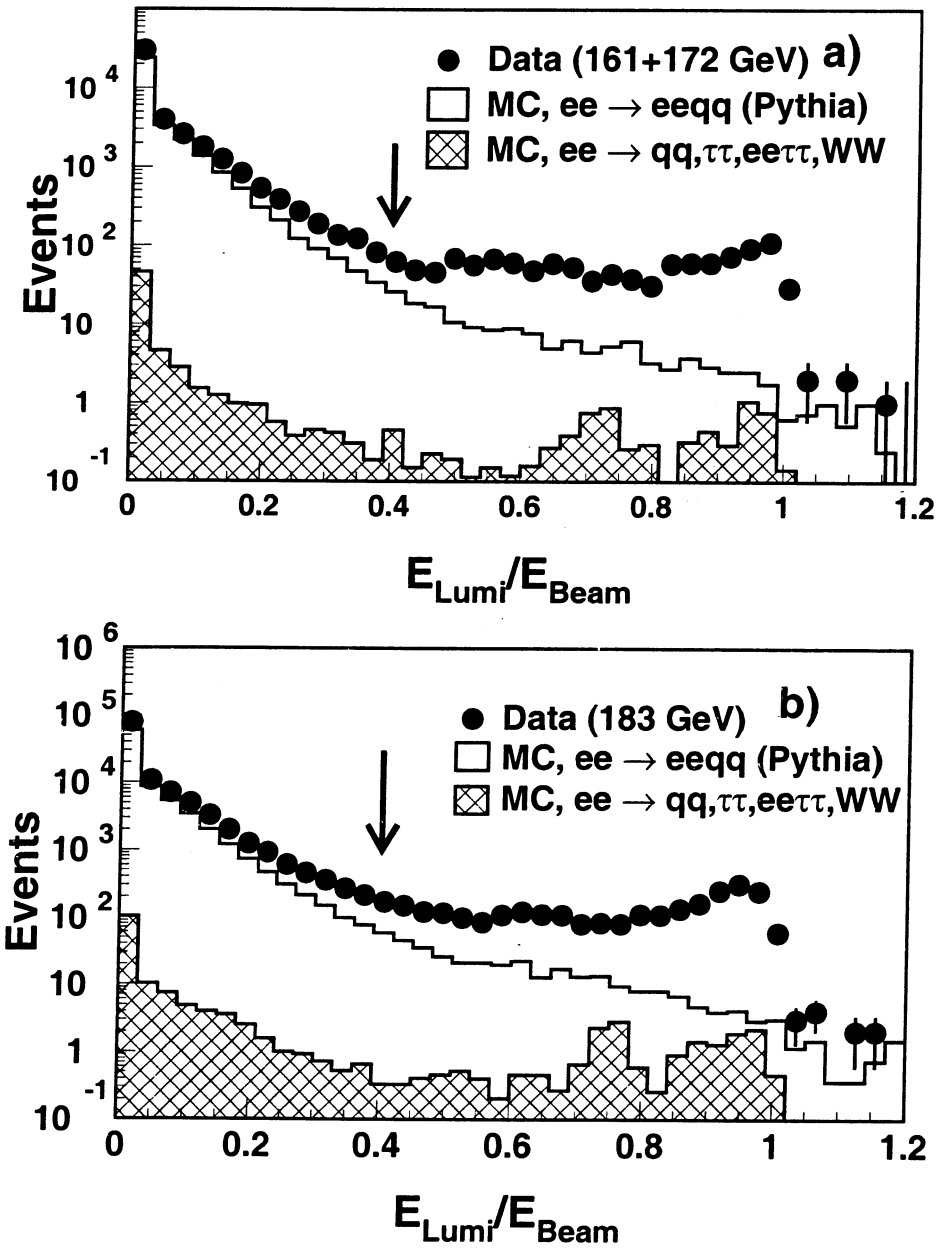

Figure 5.6: Ratio of the energy of the most energetic cluster in the luminosity monitor to the beam energy in the data at a) $\sqrt{s} = 161 - 172$ GeV and at b) $\sqrt{s} = 183$ GeV. Also shown are the Monte Carlo predictions for two-photon hadron production and the main backgrounds. A cut at $E_{Lumi} < 0.40\ E_{Beam}$ selects anti-tagged events.

limitations of the signal Monte Carlo, PYTHIA, which generates only events with $Q^2 < m_\rho^2$. Although there is a disagreement between the data and the simulation at high values of E_{Lumi}/E_{Beam}, the largest fraction of selected events reside at small values where there is good agreement (Figures 5.5a-b and 5.6a-b).

A typical feature of two-photon collisions is a momentum balance in the transverse plane and a relatively large imbalance for the longitudinal projection. This feature is illustrated in the event display of the transverse (Figure 5.7) and the longitudinal (Figure 5.8) view of an event. The plots show an event with a muon tracked from the interaction vertex to the muon chambers. The muon is balanced in the transverse plane by a shower in the BGO.

The numbers of events selected in the data at the different energies are given in Table 5.2 along with the Monte Carlo prediction, the integrated luminosities and the trigger efficiencies. The number of predicted events at the hadronic selection stage is about 22% lower than in the data partly because Monte Carlo events are generated with a cut on $\gamma\gamma$ invariant mass at 3 GeV. A comparison of the shapes of different distributions shows good agreement between the data and the Monte Carlo. After the hadron selection, the background from the annihilation processes and the two-photon production of tau pairs is about 2% at $\sqrt{s} = 91$ GeV and is below 1% at higher energies. The background at $\sqrt{s} = 91$ GeV is dominated by the $e^+e^- \rightarrow Z \rightarrow q\bar{q}$ process. Charm events make up about 10% of the hadronic two-photon sample as estimated by the Monte Carlo.

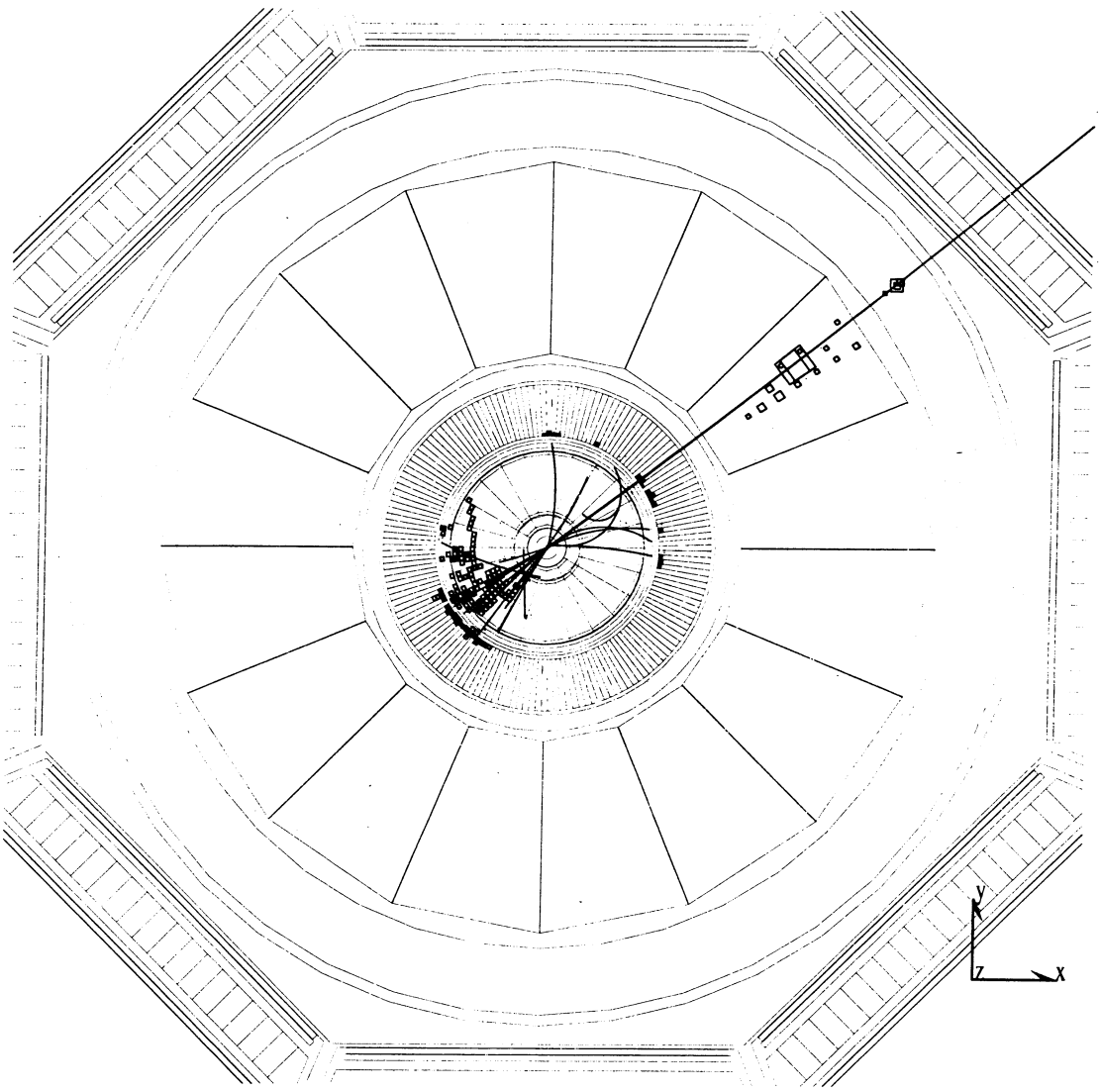

Transverse Imbalance :	.1627		**Longitudinal Imbalance :**	.5742	
Thrust :	.7681	**Major :**	.5903	**Minor :**	.0812
Event DAQ Time :	*960717 43936*				

Figure 5.7: Display of the transverse view of a two-photon muon event. The muon leaves a MIP trail in the HCAL before penetrating the muon chamber.

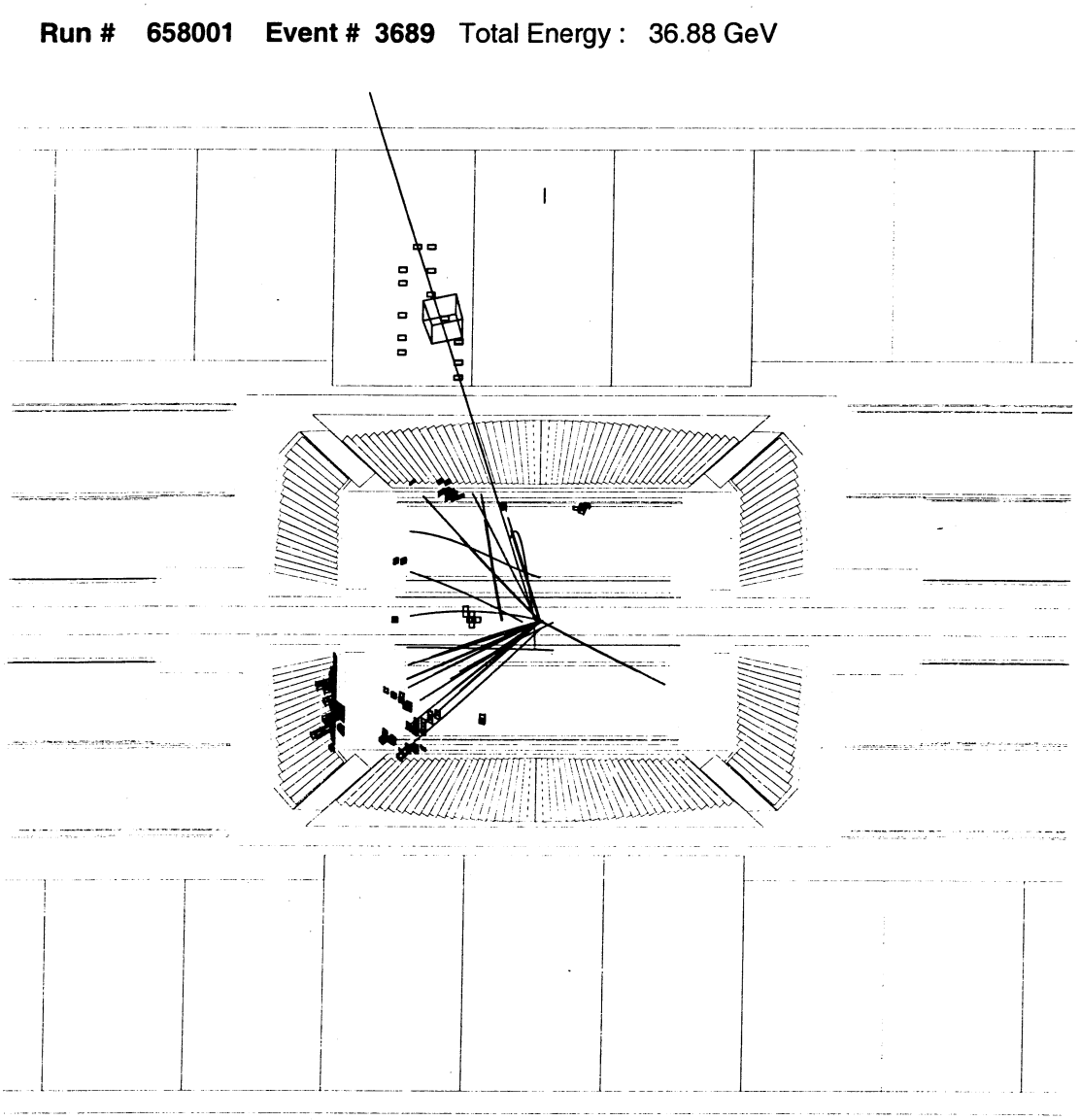

Transverse Imbalance :	.1627		**Longitudinal Imbalance :**	.5742	
Thrust :	.7681	**Major :**	.5903	**Minor :**	.0812
Event DAQ Time :	*960717 43936*				

Figure 5.8: Display of the longitudinal view of a two-photon muon event. There is a large momentum imbalance in the forward (postive z) direction.

Table 5.2: Hadronic two-photon event summary. Data samples were collected by L3 from 1994 to 1997 at $\sqrt{s} = 91 - 183$ GeV at the corresponding integrated luminosities $\mathcal{L}$ and trigger efficiencies. The number of selected hadronic data events along with the Monte Carlo predictions and the background fractions are given.

$\sqrt{s}$ $[GeV]$	$\mathcal{L}$ $[\mathrm{pb}^{-1}]$	Trigger Efficiency	Data Events	MC (PYTHIA) Events	BKG %
91	79.8	0.872	93204	72804	2.4
$130 - 140$	12.1	0.830	21045	16651	0.2
$161 - 172$	21.2	0.826	44444	34384	0.2
183	52.2	0.786	116760	90806	0.2

5.2 Electron Tag

One method of reducing the hadronic two-photon data sample to a majority of charm quark events begins by selecting electrons. Electrons lose their entire energy in the ECAL giving rise to characteristic electromagnetic showers. Hadrons lose their energy dominantly through nuclear interactions. The ECAL is only one interaction length thick, so many hadrons pass through as minimum ionizing particles (MIPs) or produce diffuse energy deposits with large fluctuations. Muons produce small signals as MIPs. Therefore, a study of the shower shape enables identification of electrons from muons and hadrons. The tracking chamber provides the track momentum and the distance of closest approach of the track to the interaction vertex measurement. This information helps to discriminate the electrons which decay from charm quarks from other sources of electrons such as photon conversions ($\gamma \rightarrow \mathrm{e}^+\mathrm{e}^-$) and π^0 Dalitz decays.

A tiny sample of electron candidates is extracted from the huge background of pions by studying the distributions of several different variables. Each variable cut is initially chosen by the eye to best separate the signal and the background in the Monte Carlo (Figure 5.9). Ideally, one would like to obtain a data sample with 100% electron purity, but there is always a region of overlap for both signal and background. Therefore, with each

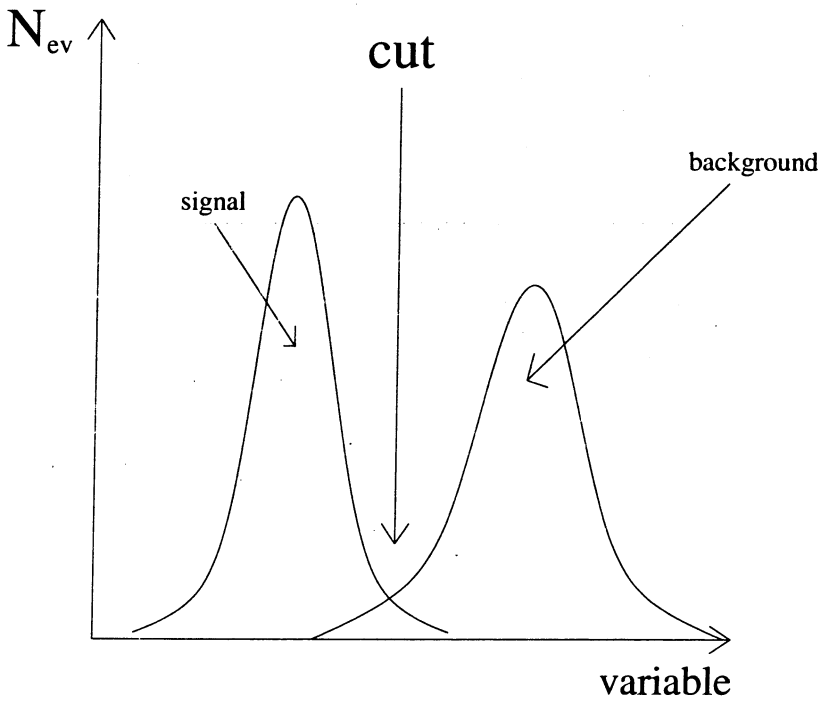

Figure 5.9: Variable cut is chosen by eye to separate signal from background.

cut applied to remove the background, some fraction of the signal will also be removed, so the electron selection efficiency decreases. A balance must be achieved in order to reject the maximum amount of background while at the same time losing the minimum amount of signal electrons. The choice

and combination of cuts were optimized by minimizing the uncertainty on the cross section measurement due to the final number of selected events and the ratio of the signal to the background. In total, cuts on eight different variables are applied (Table 5.3).

Table 5.3: Electron candidate cut selection.

Variable	Cut Threshold
p	> 0.6 GeV
$\|\cos\theta\|$	< 0.9
$\|\Delta\varphi\|$	< 20 mrad
χ^2	< 3
|DCA|	< 0.5 mm
E_1/E_9	> 0.5
E_9/E_{25}	> 0.95
E_t/p_t	> 0.85
E_t/p_t	< 1.20

The method of electron selection is identical for each energy, but the choice of each variable cut was determined with the best statistical sample at 183 GeV. All plots are at the N-1 level with respect to the final selection of an electron candidate. All of the variable cuts have been applied except for the variable that is being shown. The electron candidate is defined as the track matched to the most energetic bump in a selected event. In all of the plots, the Monte Carlo distributions are scaled to the final number of events selected in the data for a given center-of-mass energy. Therefore, in some distributions, the normalization will be less than perfect outside of the region for which the cut was applied. This disagreement between data and

Monte Carlo is taken into consideration in calculating the contribution of a given cut to the total systematic error.

We require that the electron candidate have a momentum greater than 0.6 GeV. Electrons which decay from charm quarks are on average more energetic than electrons decaying from other sources (Figure 5.10). The number of

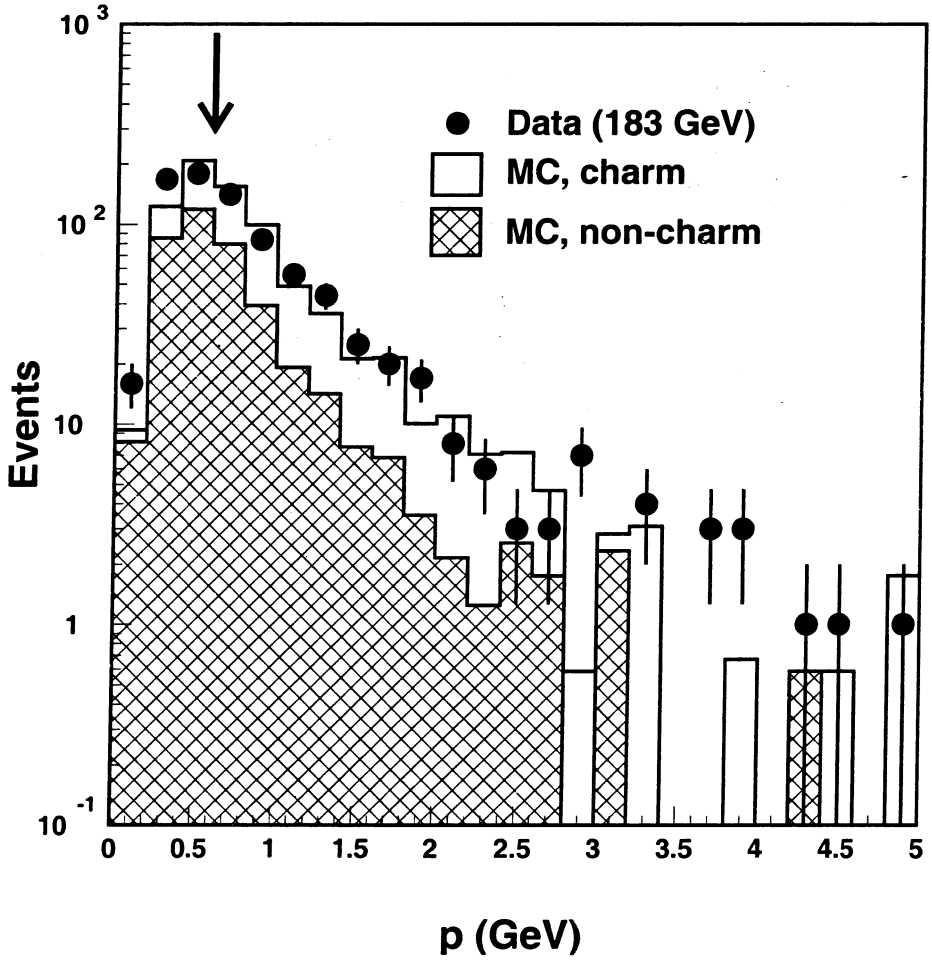

Figure 5.10: Momentum of the electrons at $\sqrt{s} = 183$ GeV. The electron candidate event is defined as either originating from charm or non-charm decay.

non-charm events in the Monte Carlo decrease more rapidly with increasing momentum than the charm events. This cut is effective at removing electrons from pair production and from non-charm quark decays.

A cut is made on the polar angle because of the detector geometry. At very small angles, a track does not hit enough wires in the TEC in order to make an accurate measurement of the position and the energy. The analysis is restricted to the polar angle range of $|\cos\theta| < 0.9$.

The sample of electron candidates is refined by the following selection criteria:

- The EM cluster matches to a track. The difference between the azimuthal angles estimated from the shower barycenter and from the track impact point at the calorimeter must be smaller than 20 mrad (Figures 5.11a-b). This cut rejects 30% of the hadron background while retaining 94% of the electron signal.

- To confirm that a shower in the EM calorimeter is created by an electron, the distribution of energies measured in the crystals of the calorimeter are compared to that of an EM cluster using a χ^2 test. As shown in Figures 5.12a-b, a cut of $\chi^2 < 3$ rejects non-electron background.

- The distance of closest approach (DCA) of the track to the average position of the e^+e^- collision point in the r-ϕ plane must be less than 0.5 mm (Figures 5.13a-b). This cut rejects 71% of electron candidates from photon conversions while keeping more than 88% of signal electrons.

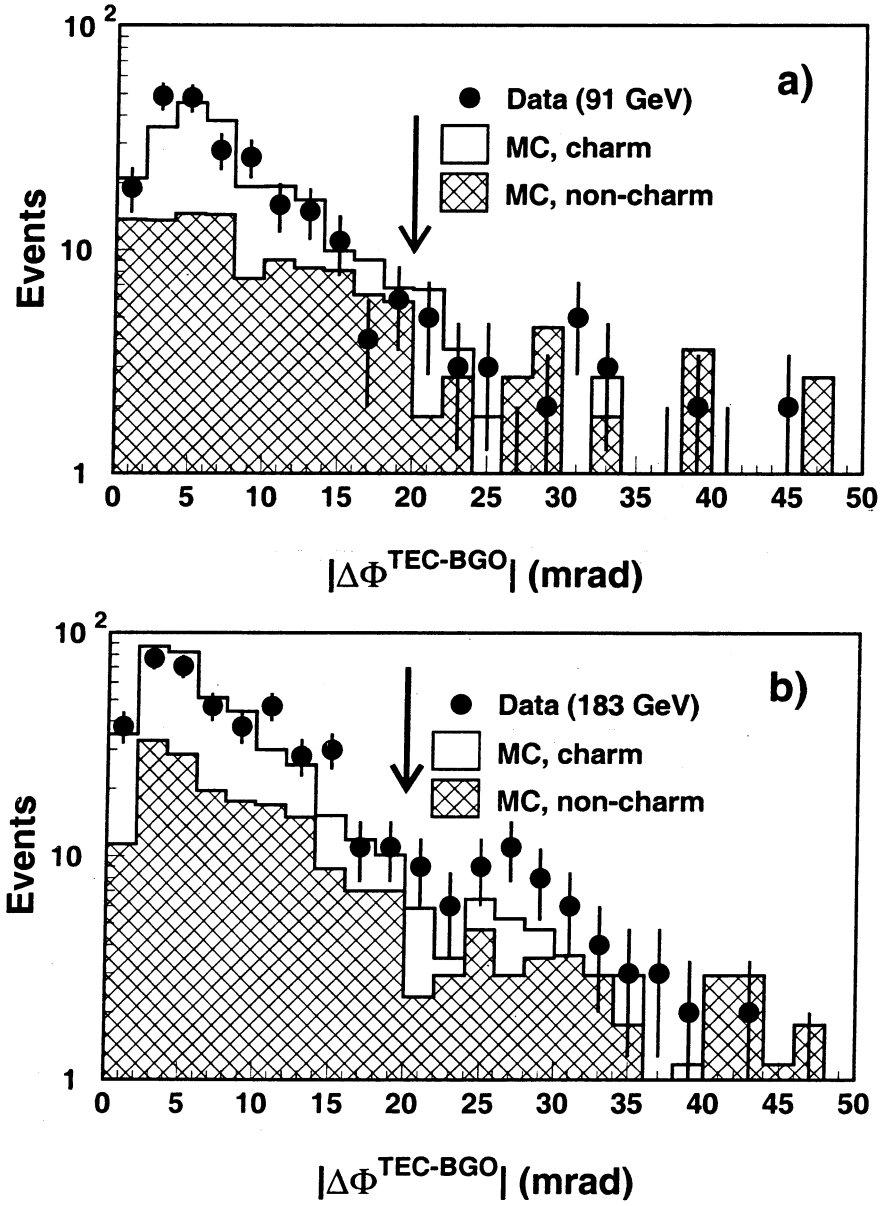

Figure 5.11: Matching of the azimuthal angle of the electron candidate track in the TEC to the shower in the BGO at a) $\sqrt{s} = 91$ GeV and b) $\sqrt{s} = 183$ GeV. A cut at $|\Delta\varphi| < 20$ mrad removes about 30% of the non-electron background. The interval from 0 to 50 mrad was chosen to highlight the signal and to show agreement between the data and the Monte Carlo simulation. About 17% of the background events are not shown as they range from 50 to 300 mrad.

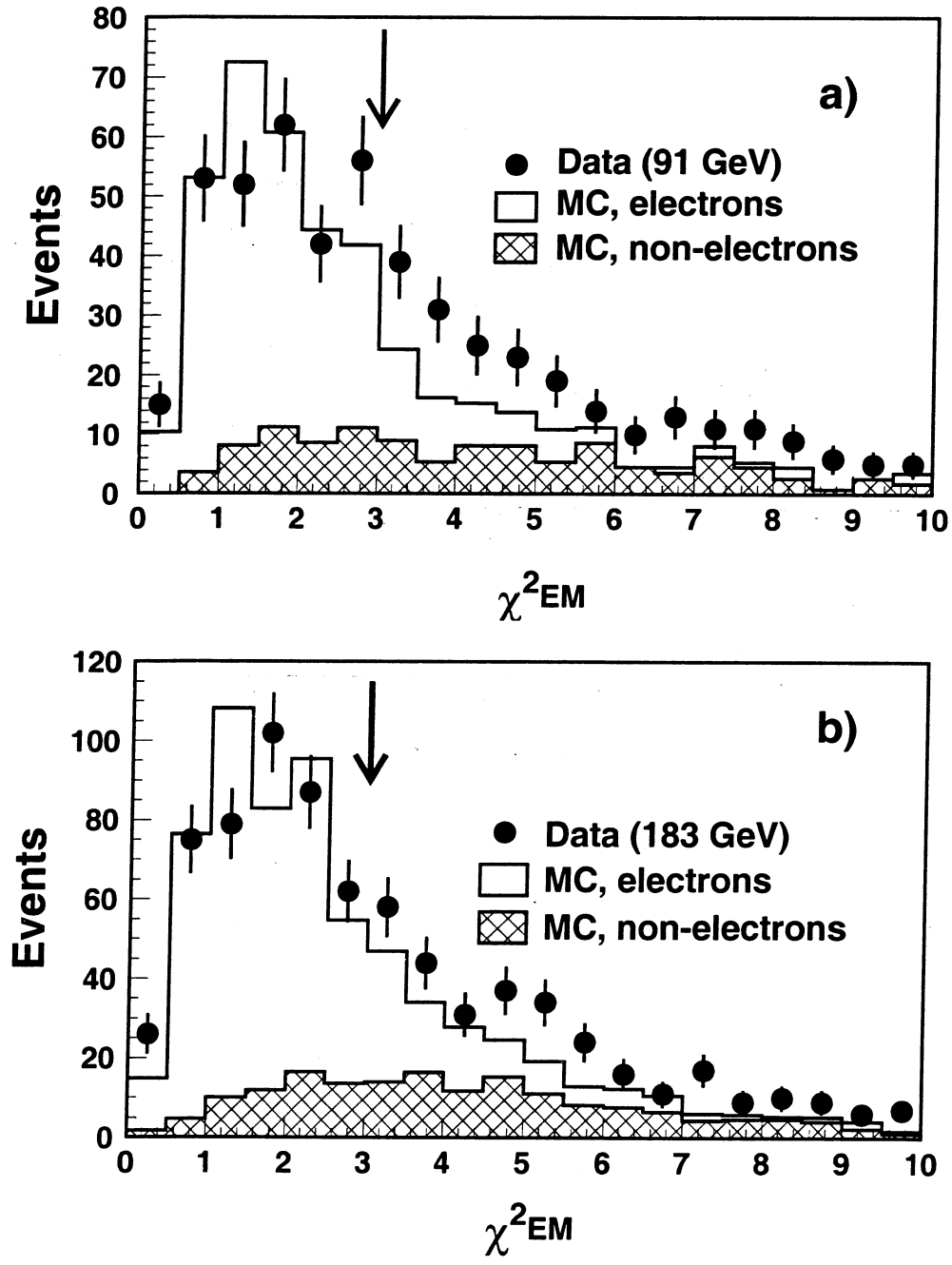

Figure 5.12: A χ^2 test to identify a shower in the BGO as an EM cluster at a) $\sqrt{s} = 91$ GeV and b) $\sqrt{s} = 183$ GeV. A cut of $\chi^2 < 3$ is applied to favor electrons.

This cut improves on the fraction of electrons originating from charm semileptonic decays.

- The lateral shower shape of the cluster must be consistent with an EM shower. E_1/E_9 is the ratio of the energy deposited in the central crystal to the energy of the 9 crystals around the shower center (Figures 5.14a-b). The shape for the non-electron background has an opposing slope to the electron shape. A cut of $E_1/E_9 > 0.5$ is applied.

- E_9/E_{25} is the ratio of the energy deposited in the 9 crystals at the shower center to the energy of the 25 crystals (Figures 5.15a-b). A cut of $E_9/E_{25} > 0.95$ is made because the EM showers of electrons are more narrow than those for hadrons.

- The cluster must also satisfy the condition $0.85 < E_t/p_t < 1.20$ (Figures 5.16a-b and 5.17a-b), where E_t is the projection of the energy of the cluster on the r-ϕ plane as measured in the EM calorimeter, and p_t is the transverse momentum of the track as measured in the tracking chamber. The curvature of the track is measured in the $r - \phi$ plane of the tracking chamber where there are 62 wires to provide an accurate measurement of the transverse momentum. In addition, the electromagnetic calorimeter has an excellent spatial resolution. Therefore, the ratio of E_t/p_t is a better choice as a variable than E/p for the L3 detector. This condition rejects more than 95% of the hadrons (mainly pions) while keeping more than 90% of the electrons. The average res-

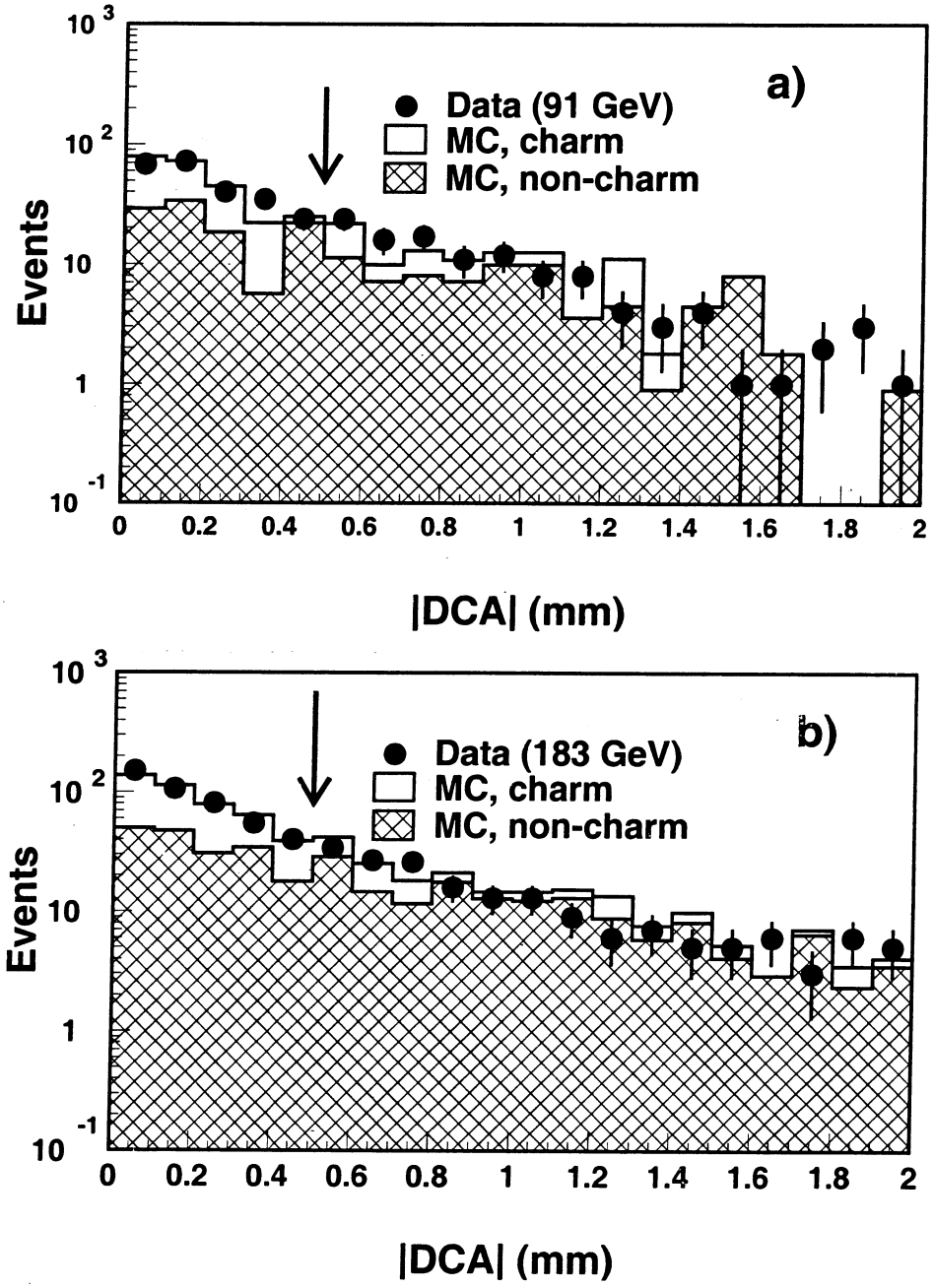

Figure 5.13: The distance of closest approach (DCA) of a track to its reconstructed vertex in the tranverse plane at a) $\sqrt{s} = 91$ GeV and b) $\sqrt{s} = 183$ GeV. A cut of $|\mathrm{DCA}| < 0.5$ mm is effective in rejecting most of the electron candidates from photon conversions.

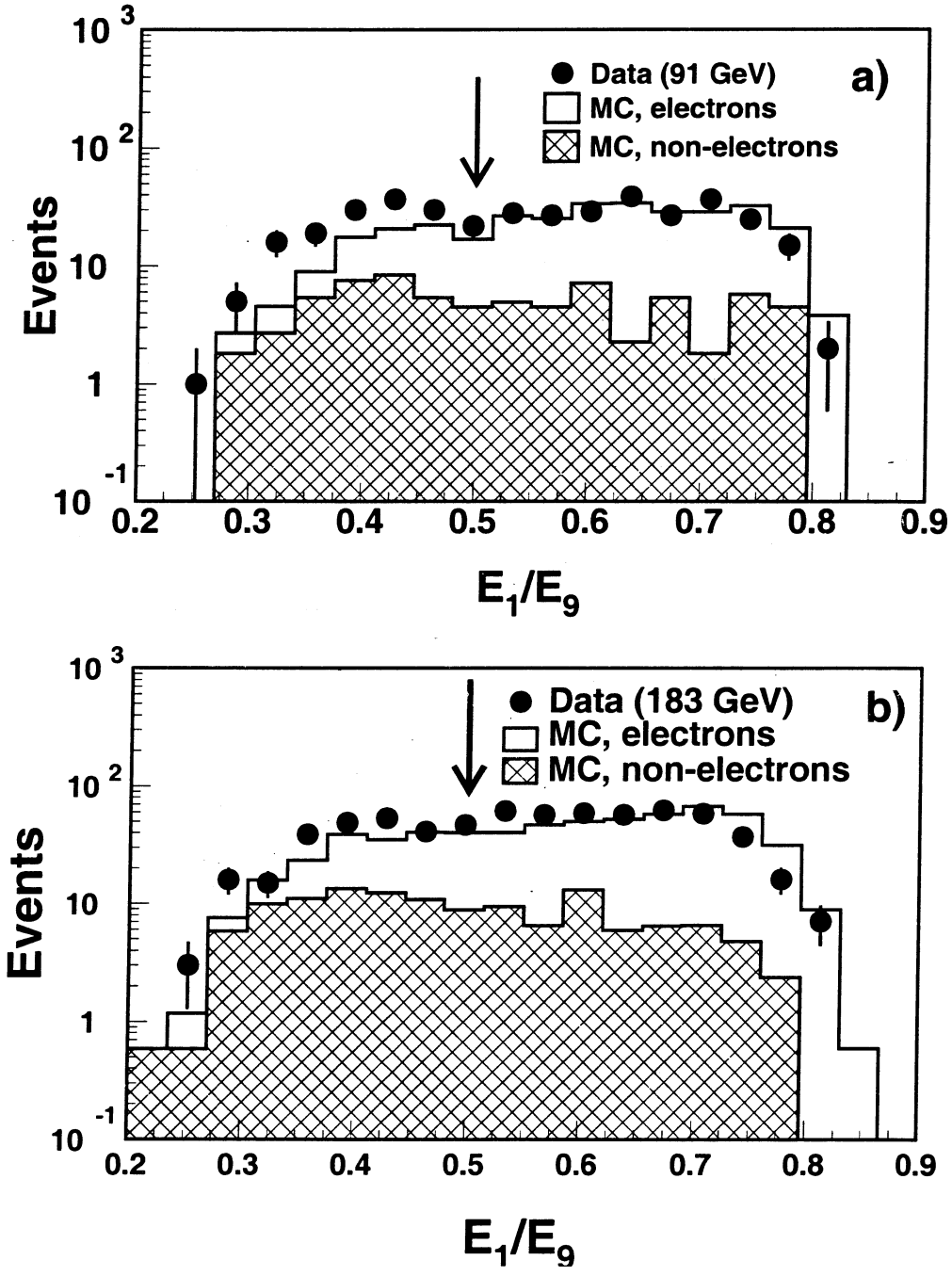

Figure 5.14: The shower shape variable E_1/E_9 at a) $\sqrt{s} = 91$ GeV and b) $\sqrt{s} = 183$ GeV. We require $E_1/E_9 > 0.5$.

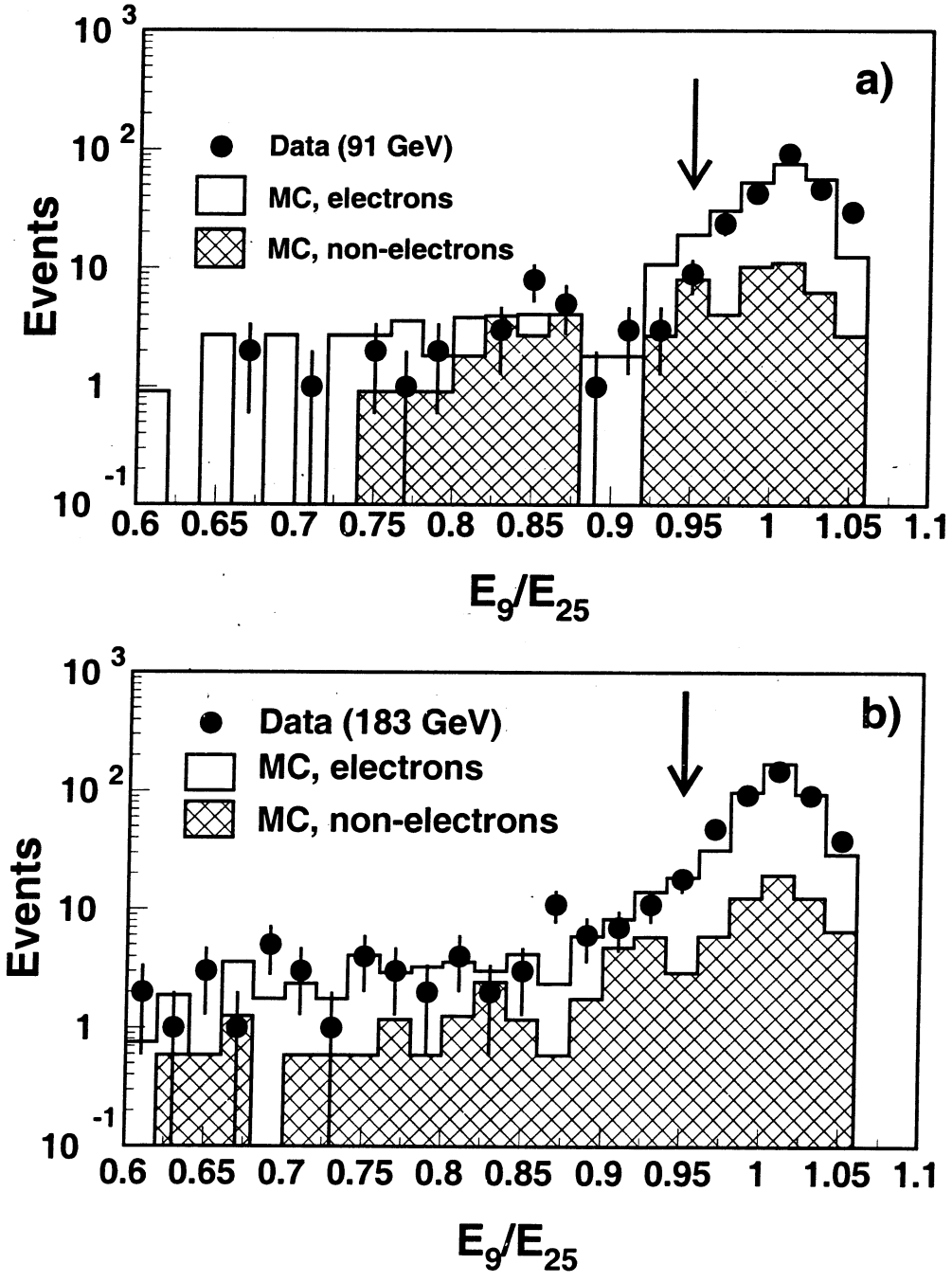

Figure 5.15: The shower shape variable E_9/E_{25} at a) $\sqrt{s} = 91$ GeV and b) $\sqrt{s} = 183$ GeV. We require $E_9/E_{25} > 0.95$.

olutions for the selected electron candidates are 4.6% on p_t and 3.3% on E_t. The residual non-electron background is about 15%.

The display for the transverse (Figure 5.18) and a longitudinal (Figure 5.19) view is shown for an electron-tagged event. The electron candidate has a momentum of 2.3 GeV as measured in the tracking chamber. The track is matched to an energy deposit of 2.3 GeV in the electromagnetic calorimeter. There is a only a small momentum imbalance in the $r - \phi$ plane due to the undetected neutrino. In the longitudinal projection, at least three jets are visible. One of these jets is at a small polar angle with respect to the negative z-axis of about 15° and does not contain the electron candidate. This low-angle jet may be the photon remnant produced in a resolved process. The remnant jet flows in the original direction of the target photon.

The number of observed events is given in Table 5.4. If the Monte Carlo prediction is only normalized to the data luminosity and corrected for the trigger efficiency, then this absolute prediction for the number of events would be 10% (60%) too small at $\sqrt{s} = 91$ GeV (183 GeV). This difference can be attributed to the fact that the PYTHIA Monte Carlo contains only leading order calculations. Although the absolute normalization of the prediction is insufficient to describe the data, the shapes of the data and Monte Carlo distributions are in good agreement when the prediction is scaled to the final number of selected data events.

The background from the annihilation processes and the two-photon production of tau pairs is 12% at $\sqrt{s} = 91$ GeV and is about 1% at higher energies (Table 5.5). We assume that this background has the same trigger

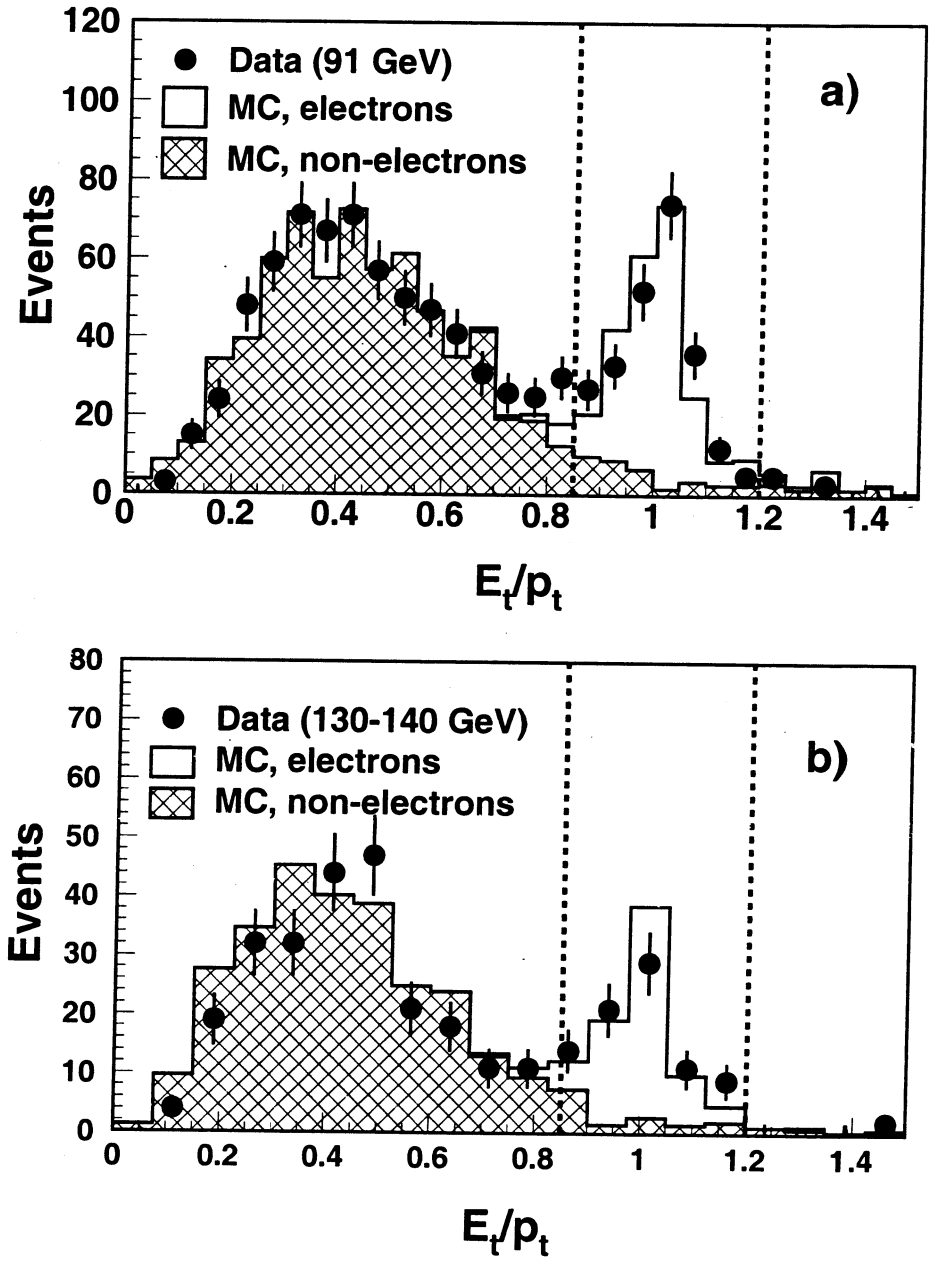

Figure 5.16: The ratio, E_t/p_t, of the transverse energy measured by the electromagnetic calorimeter and the transverse momentum of the track for a) $\sqrt{s} = 91$ GeV and b) $\sqrt{s} = 130 - 140$ GeV. A clear electron signal is observed at the expected value of $E_t/p_t = 1$. The window, defined by the dashed lines, of $0.85 < E_t/p_t < 1.2$ indicates the selected electron candidates.

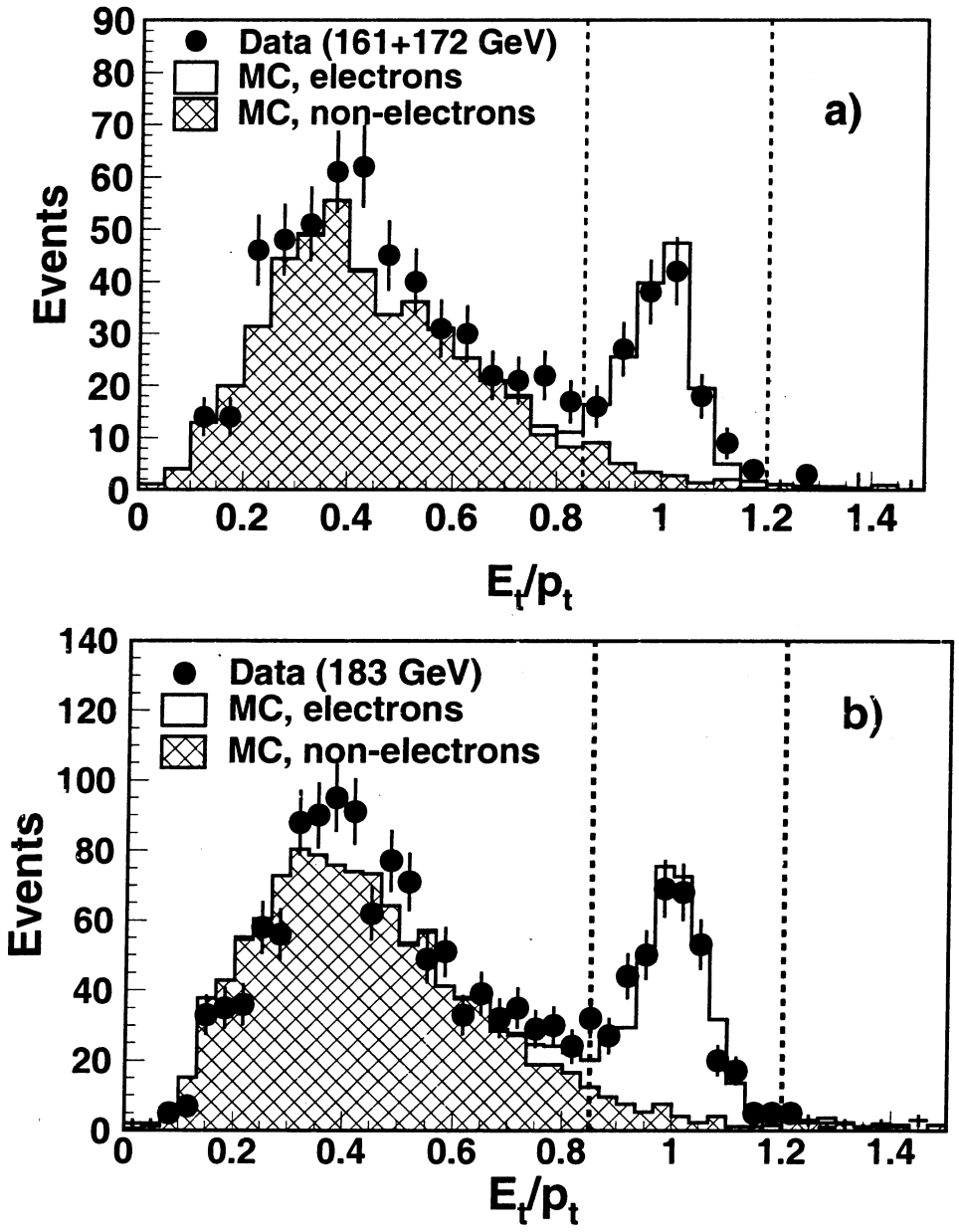

Figure 5.17: The ratio, E_t/p_t, of the transverse energy measured by the electromagnetic calorimeter and the transverse momentum of the track for a) $\sqrt{s} = 161 - 172$ GeV and b) $\sqrt{s} = 183$ GeV. A clear electron signal is observed at the expected value of $E_t/p_t = 1$. The window, defined by the dashed lines, of $0.85 < E_t/p_t < 1.2$ indicates the selected electron candidates.

Run # 688501 Event # 1069 Total Energy : 29.94 GeV

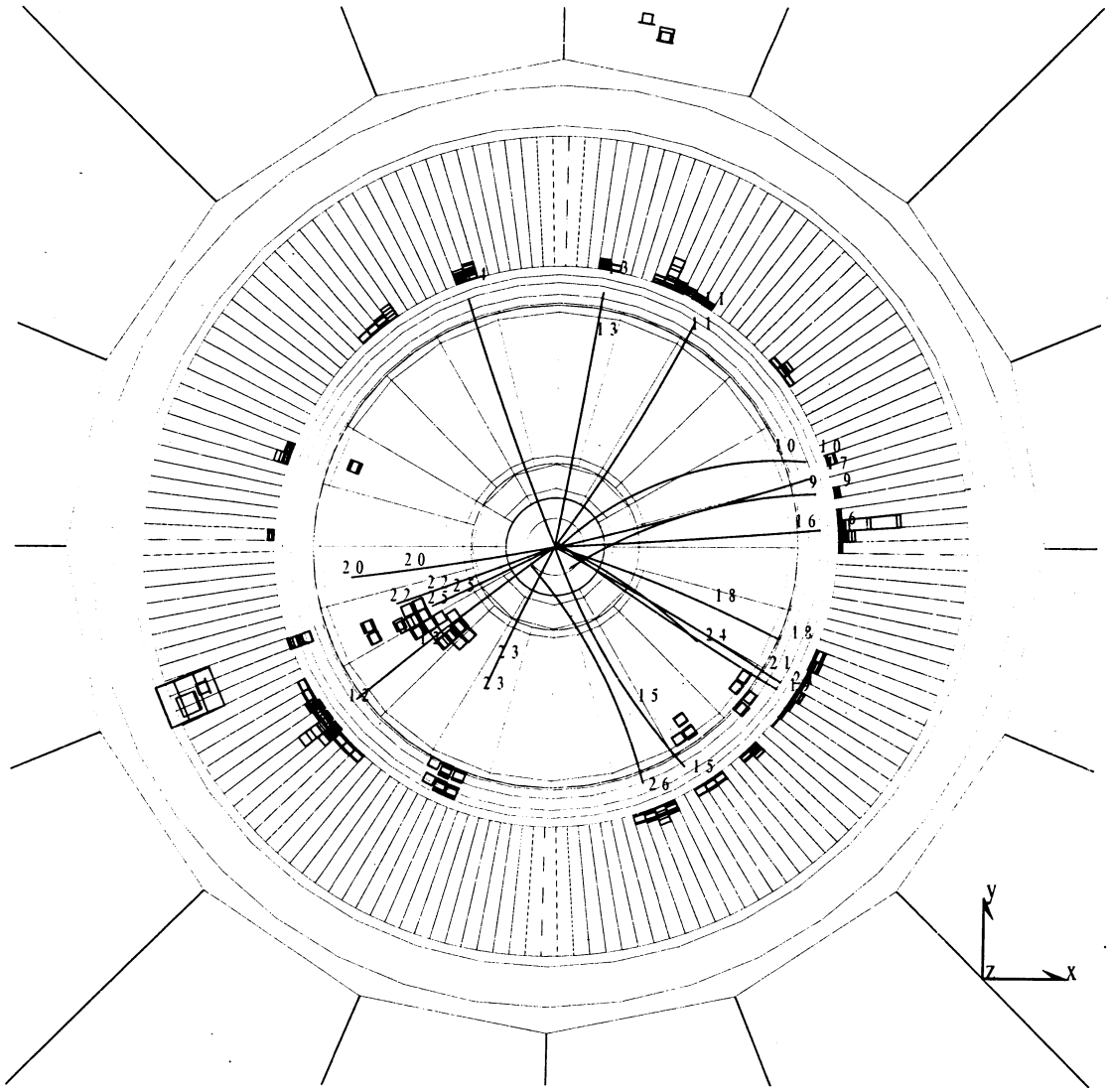

Transverse Imbalance :	.0453		**Longitudinal Imbalance :**	-.5303	
Thrust :	.7080	**Major :**	.4463	**Minor :**	.3052
Event DAQ Time :	*971027 145523*				

Figure 5.18: Display of the transverse view of a two-photon electron event. The electron candidate has a momentum of 2.3 GeV and an energy deposit in the electromagnetic calorimeter of the same amount. The track is matched to a BGO shower at an azimuthal angle, $\phi \simeq 3°$.

Run # 688501 Event # 1069 Total Energy : 29.94 GeV

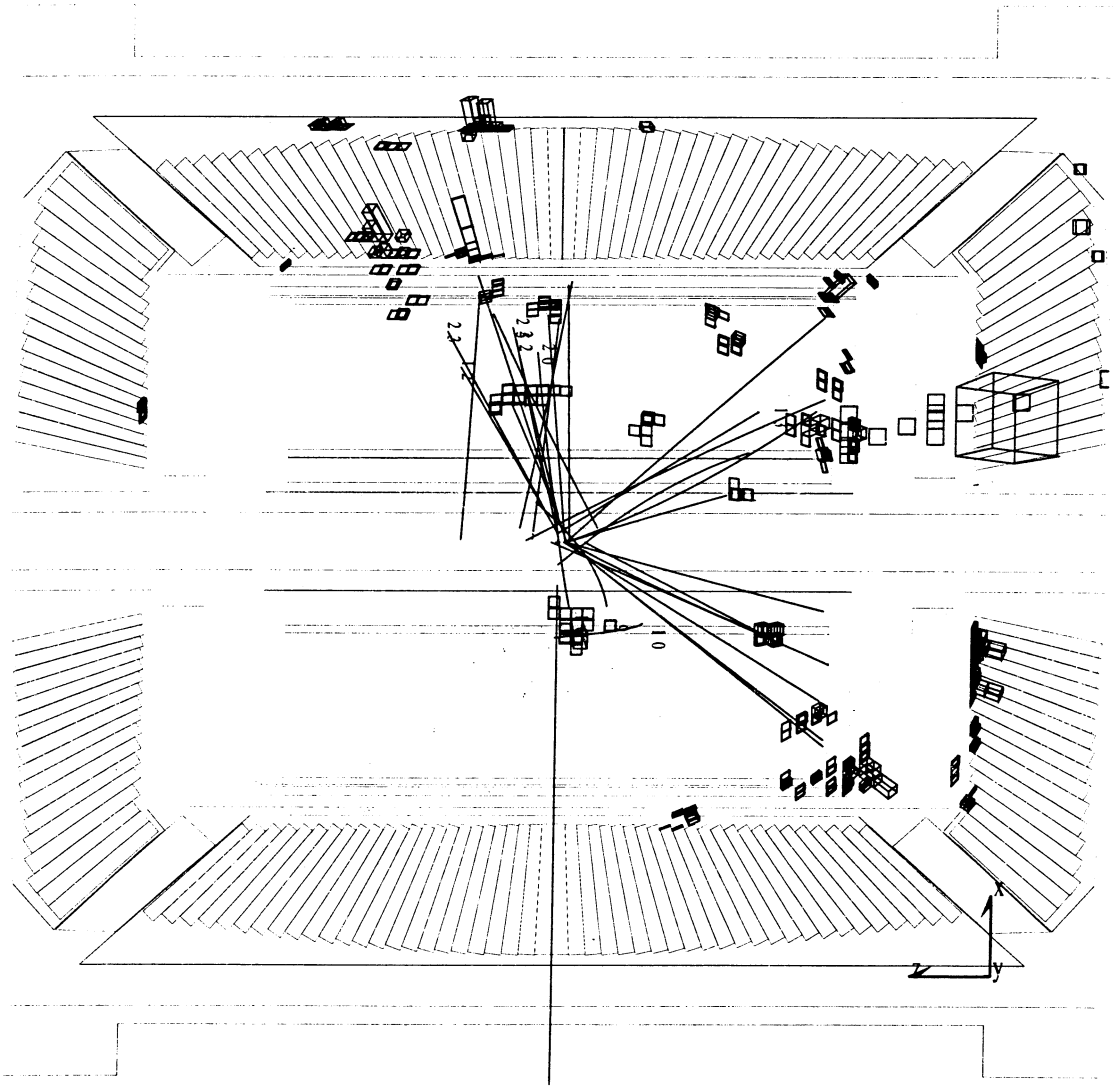

Transverse Imbalance :	.0453		**Longitudinal Imbalance :**	-.5303	
Thrust :	.7080	**Major :**	.4463	**Minor :**	.3052
Event DAQ Time :	*971027 145523*				

Figure 5.19: Display of the longitudinal view of a two-photon electron event. The track of the electron candidate is matched to an energy deposit of 2.3 GeV in the BGO at a polar angle, $\theta \simeq 73°$. There is a large momentum imbalance in the backward (negative z) direction.

Table 5.4: Summary of the electron tag analysis for the data collected at $\sqrt{s} = 91 - 183$ GeV . The column elements from left to right are the center of mass energy, the events selected by the electron tag ($N_{observed}$), the Monte Carlo prediction ($N_{expected}$), the background from sources other than two-photon hadronic interactions, the electrons from photon conversions, the electron purity and the electron selection efficiency, respectively. N_{BKG}, N_{Conv}, P_e and ϵ_e are all estimated from Monte Carlo.

$\sqrt{s}$	$N_{observed}$	$N_{expected}$	N_{BKG}	N_{Conv}	P_e	ϵ_e
91	282	252	29.5	37.1	0.84	0.097
130 – 140	82	45	0.5	8.4	0.84	0.084
161 – 172	156	112	1.5	22.8	0.85	0.096
183	433	273	4.1	50.5	0.86	0.100

Table 5.5: Background from sources other than two-photon hadronic interactions for electron tag analysis. The background is estimated from Monte Carlo.

LEP energy $[GeV]$	Number of expected background events	Background source
$\sqrt{s} = 91$	19.2 ± 7.2	$Z \to q\bar{q}$
	7.4 ± 1.7	$e^+e^- \to \tau^+\tau^-$
	2.9 ± 0.8	$e^+e^- \to e^+e^-\tau^+\tau^-$
$\sqrt{s} = 130 - 140$	0.2 ± 0.1	$e^+e^- \to e^+e^-\tau^+\tau^-$
	0.2 ± 0.2	$e^+e^- \to e^+e^-q\bar{q}$
	< 0.1	$e^+e^- \to \tau^+\tau^-$
$\sqrt{s} = 161 - 172$	0.9 ± 0.2	$e^+e^- \to e^+e^-\tau^+\tau^-$
	0.7 ± 0.2	$e^+e^- \to q\bar{q}$
	< 0.1	$e^+e^- \to \tau^+\tau^-$
	< 0.1	$e^+e^- \to W^+W^-$
$\sqrt{s} = 183$	2.6 ± 0.7	$e^+e^- \to e^+e^-\tau^+\tau^-$
	1.5 ± 0.2	$e^+e^- \to q\bar{q}$
	< 0.1	$e^+e^- \to \tau^+\tau^-$
	< 0.1	$e^+e^- \to W^+W^-$

efficiencies as the hadronic two-photon signal events. The electron efficiency after hadronic selection is 43%. The electron selection reduces the electron efficiency to about 10% (mostly due to the electromagnetic shower shape requirement). Both the electron selection efficiency and the electron purity are estimated using the PYTHIA Monte Carlo. The electron purity is defined as the ratio of electron candidates, where the track matched to the most energetic bump is a true electron, to the total number of electron candidates selected. The electron purity is about 85% at all energies. The 15% background of non-electrons is well illustrated in Figures 5.16-5.17. The Monte Carlo includes electrons from π^0 Dalitz decays; such electrons give a contribution of 12.7% to the electron sample.

In Figures 5.20a-b, the track multiplicity per event is shown for the final sample of electron candidates. Most of the background from $e^+e^- \to \tau^+\tau^-$ and $e^+e^- \to e^+e^-\tau^+\tau^-$ events is removed when 5 or more tracks are required per event.

In Section 5.1 on the hadron selection, the normalization of the Monte Carlo with the data was not in agreement at low visible mass because the events simulated with PYTHIA are generated with a visible mass greater than 3 GeV. If no cut is applied to the visible mass in the selection of two-photon hadronic events, then one would see in Figure 5.21a that the prediction would agree well in shape with the final data sample after the electron selection. In fact, no signal charm events are lost to the visible mass cut. If no cut of $E_{Lumi}/E_{Beam} < 0.40$ was made to require anti-tagged events

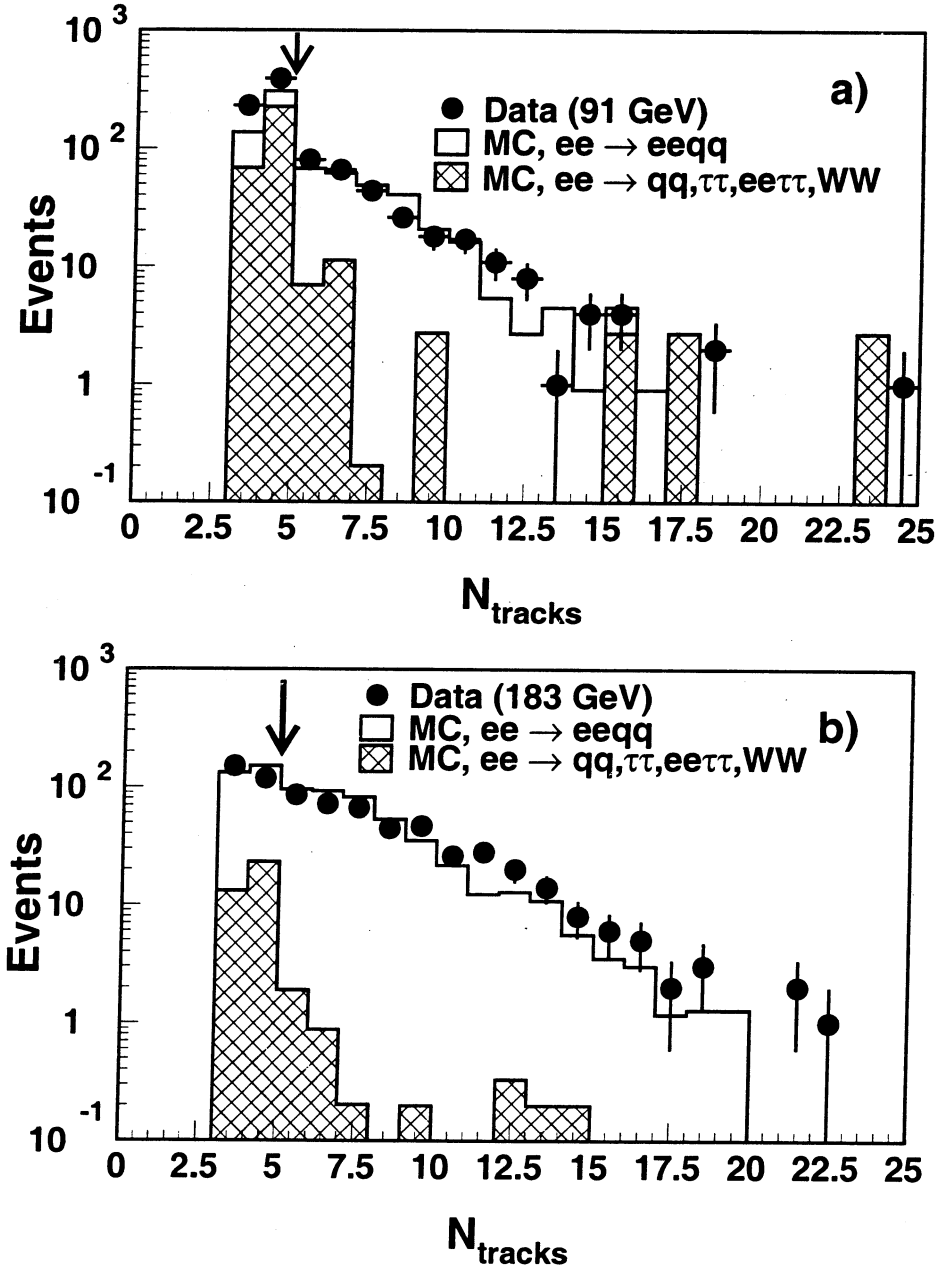

Figure 5.20: Track multiplicity for the final event sample in the data at a) $\sqrt{s} = 91$ GeV and at b) $\sqrt{s} = 183$ GeV. A cut of at least five good tracks removes background from $e^+e^- \to \tau^+\tau^-$ and $e^+e^- \to e^+e^-\tau^+\tau^-$ events.

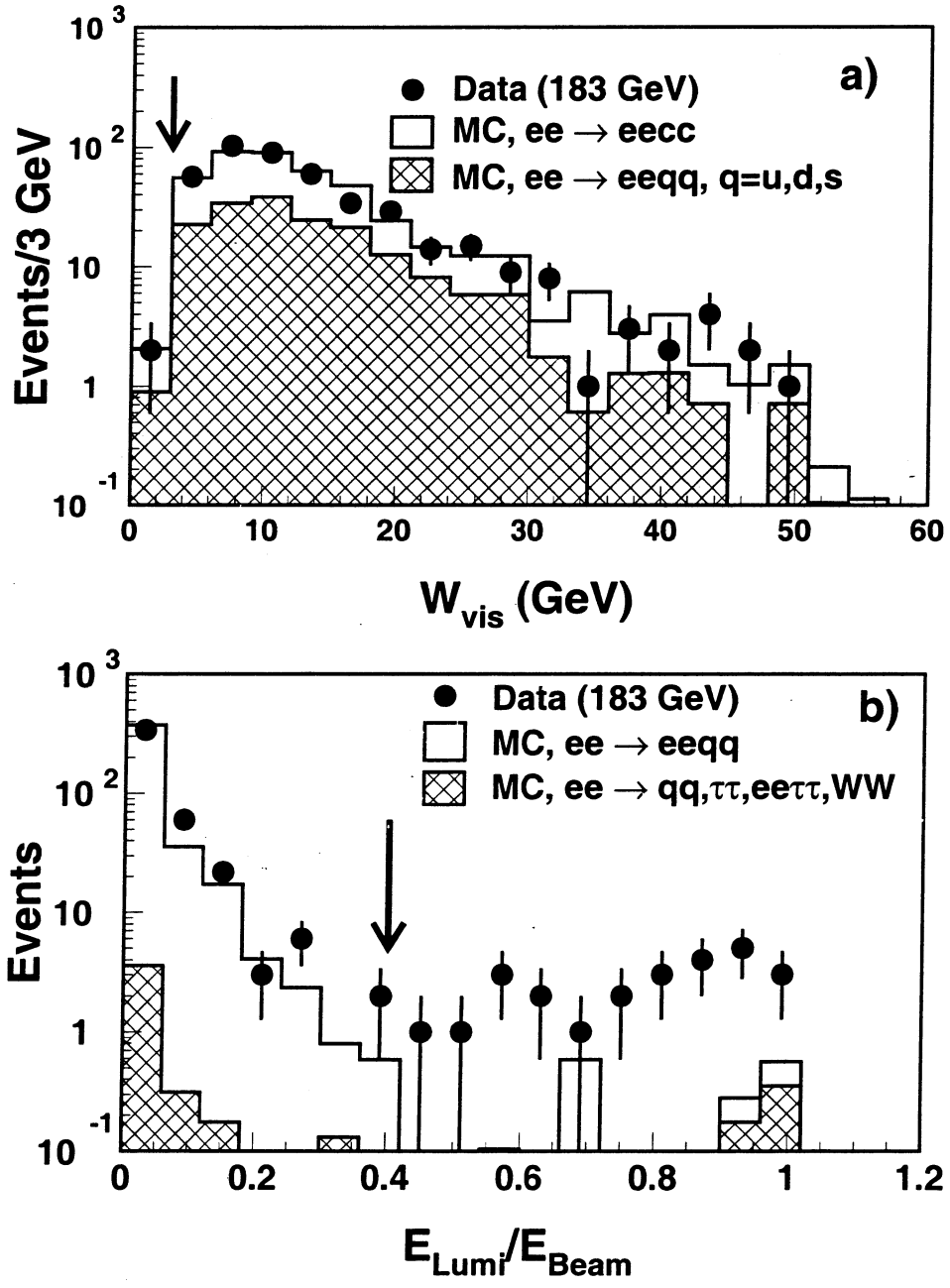

Figure 5.21: The final event distributions of a) the visible mass and b) the ratio of the most energetic luminosity cluster to the beam energy for the data at $\sqrt{s} = 183$ GeV. The Monte Carlo predictions are also given.

(Figure 5.21b), the final data sample after electron selection would be about 5.5% larger at $\sqrt{s} = 183$ GeV.

5.3 Muon Tag

Although muons are produced at a smaller rate than electrons in the semileptonic decay of charmed mesons, muons are more easily discriminated from other particles and therefore are selected more efficiently (Table 5.6). By design, the electromagetic and hadron calorimeters effectively stop electrons, photons and hadrons before they can penetrate to the muon chambers. The

Table 5.6: Muon candidate cut selection.

Variable	Cut Threshold
p	> 2.0 GeV
p	< 0.2 E_{Beam}
$\|\cos\theta\|$	< 0.9

muons leave a MIP signature in the calorimeters depositing a total of about 2 GeV in the ECAL and HCAL before reaching the muon chambers. Muons produced by decays in the calorimeters are sources of background which are rejected by matching the muon to a track in the TEC. The cosmic ray muons are rejected when the time-of-flight provided by the scintillators is within the beam crossing time (± 5 ns).

The muon candidate is required to have a momentum greater than 2 GeV because only such muons can penetrate the calorimeters and reach the muon chambers. In addition, muons produced from light quark hadron decay, e.g., $\pi^+ \rightarrow \mu^+\nu_\mu$, have on average a lower momentum. This momentum cut thus favors muons from heavy flavor decay. The contribution from the annihilation

processes are suppressed by requiring the muon momentum to be less than 0.2 E_{beam}. The angular acceptance is limited to $|\cos\theta| < 0.9$ (Figure 5.22).

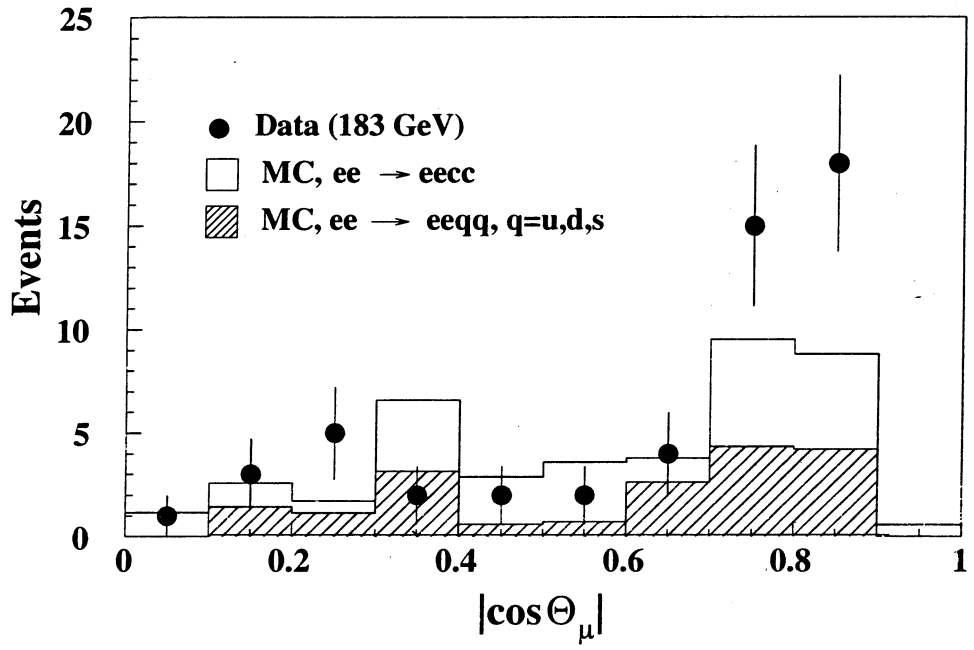

Figure 5.22: Polar angle distribution of the events at $\sqrt{s} = 183$ GeV selected with the muon tag. Also shown are the Monte Carlo predictions for the charm production and the non-charm background.

The number of observed events is given in Table 5.7. The Monte Carlo prediction is scaled to the final number of selected data events in the muon tag distributions. The trigger efficiency is higher by a factor 1.08 than in the case of the electron selection due to the higher momentum cut. For a momentum greater than 2 GeV and a fiducial volume of $|\cos\theta| < 0.9$, the muon selection efficiency, ϵ_μ, is estimated to be 33%; the muon purity, P_μ, is 100%. The background from annihilation processes and two-photon

Table 5.7: Summary of the muon tag analysis for the data collected at $\sqrt{s} = 91 - 183$ GeV . The column elements from left to right are the center of mass energy, the events selected by the muon tag ($N_{observed}$), the Monte Carlo prediction ($N_{expected}$), the background from sources other than two-photon hadronic interactions, the muon purity and the muon selection efficiency, respectively. N_{BKG}, P_μ and ϵ_μ are all estimated from Monte Carlo.

$\sqrt{s}$	$N_{observed}$	$N_{expected}$	N_{BKG}	P_μ	ϵ_μ
91	57	45	16.9	1.00	0.33
161 – 172	16	15	1.4	1.00	0.33
183	52	39	1.4	1.00	0.33

Table 5.8: Background from sources other than two-photon hadronic interactions for muon tag analysis. The background is estimated from Monte Carlo.

LEP energy $[GeV]$	Number of expected background events	Background source
$\sqrt{s} = 91$	6.8 ± 0.3	$e^+e^- \to q\bar{q}$
	6.5 ± 0.2	$e^+e^- \to \tau^+\tau^-$
	0.9 ± 0.4	$e^+e^- \to e^+e^-\tau^+\tau^-$
$\sqrt{s} = 161 - 172$	1.8 ± 0.2	$e^+e^- \to q\bar{q}$
	0.3 ± 0.2	$e^+e^- \to e^+e^-\tau^+\tau^-$
	0.05 ± 0.01	$e^+e^- \to \tau^+\tau^-$
	< 0.1	$e^+e^- \to W^+W^-$
$\sqrt{s} = 183$	0.9 ± 0.3	$e^+e^- \to q\bar{q}$
	0.3 ± 0.3	$e^+e^- \to e^+e^-\tau^+\tau^-$
	0.3 ± 0.1	$e^+e^- \to W^+W^-$
	< 0.1	$e^+e^- \to \tau^+\tau^-$

production of tau pairs is 24% at $\sqrt{s} = 91$ GeV and about 5% at higher energies (Table 5.8).

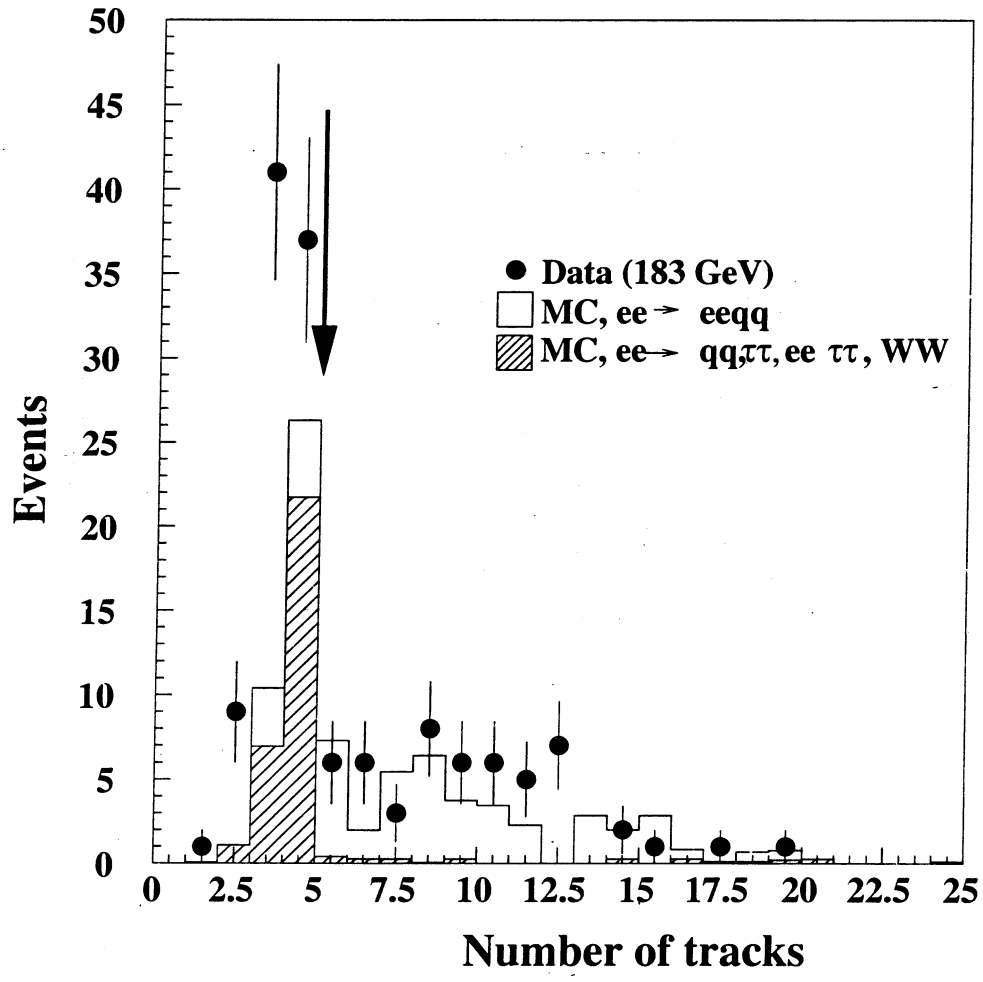

Figure 5.23: Track multiplicity for the final event sample selected by the muon tag in the data at $\sqrt{s} = 183$ GeV. The τ background is removed by requiring five or more good tracks.

In Figure 5.23, the track multiplicity per event is shown for the final sample of muon candidates at $\sqrt{s} = 183$ GeV. Most of the background from

$e^+e^- \to \tau^+\tau^-$ and $e^+e^- \to e^+e^-\tau^+\tau^-$ events is removed when 5 or more tracks are required per event.

5.4 Inclusive Lepton Cross Sections

The inclusive lepton cross section,

$$\Delta\sigma(e^+e^- \to e^+e^-q\bar{q} \to e^+e^- + \text{hadrons} + \text{lepton}), \tag{5.2}$$

is calculated for a kinematic range and a fiducial volume for both electrons and muons. The sample of events selected by the electron and the muon tag are used. The calculated cross sections may be compared to measurements made by other experiments which use a different model for charm production.

5.4.1 Inclusive Electron Cross Section

The inclusive electron cross section in the fiducial volume of $|\cos\theta| \lesssim 0.9$, with a momentum greater than 0.6 GeV and $W_{\gamma\gamma} > 3$ GeV is calculated as:

$$\Delta\sigma_e = \frac{[(N_{obs}^{lept} - N_{bkg}^{lept})\ P_e] - N_{conv}}{\mathcal{L}\ \epsilon_{trig}\ \epsilon_e}. \tag{5.3}$$

The variables are defined as follows:

- N_{obs}^{lept} is the number of events in the data after the final electron selection.
- ϵ_{trig} is the trigger efficiency which is determined from the data using a set of independent triggers.
- N_{bkg}^{lept} is the number of background events estimated from Monte Carlo which do not originate from two-photon hadronic interactions.
- N_{conv} is the estimated number of electrons from photon conversions. This background comprises about 22% of the selected electron sample.

- $\mathcal{L}$ is the total integrated luminosity.
- ϵ_e, the electron selection efficiency, is the fraction of electrons generated within $|\cos\theta| < 0.9$, with a momentum greater than 0.6 GeV and $W_{\gamma\gamma} > 3$ GeV which remains after final selection.
- P_e is the electron purity in the selected sample.

Table 5.9: Inclusive electron cross section. Data samples were collected by L3 from 1994 to 1997 at $\sqrt{s}$ = 91-183 GeV at the corresponding integrated luminosities $\mathcal{L}$. The number of events selected with the electron tag in the data, $N_{observed}$, is given with the number of expected events, $N_{observed}$, predicted by the Monte Carlo. The inclusive electron cross section $\Delta\sigma$ is calculated after the subtraction of annihilation and $e^+e^- \to e^+e^-\tau^+\tau^-$ background in the polar angle region $|\cos\theta| < 0.9$, for a momentum greater than 0.6 GeV and with $W_{\gamma\gamma} > 3$ GeV. The first error is statistical and the second one is systematic.

$\sqrt{s}$	$\mathcal{L}$	Electron Tag		
[GeV]	[pb^{-1}]	$N_{observed}$	$N_{expected}$	$\Delta\sigma_e$ [pb]
91	79.8	282	252	25.9 ±2.1±3.7
130 – 140	12.1	82	45	71.9 ±9.1±8.1
161 – 172	21.2	156	112	64.6 ±6.3±5.9
183	52.2	433	273	77.8 ±4.4±5.0

The trigger efficiencies and integrated luminosities are given in Table 5.2. The number of selected events, the background, the selection efficiency and the purity can be found in Table 5.4. The measured inclusive electron cross sections, $\Delta\sigma_e$, are given in Table 5.9 along with the statistical and systematic errors. We observe an increase of the cross section with increasing beam energy. The systematic error is dominated by the uncertainty on the event

selection and the electron selection efficiency. A more detailed discussion of systematic error, for both electrons and muons, will be provided in the Chapter 6.

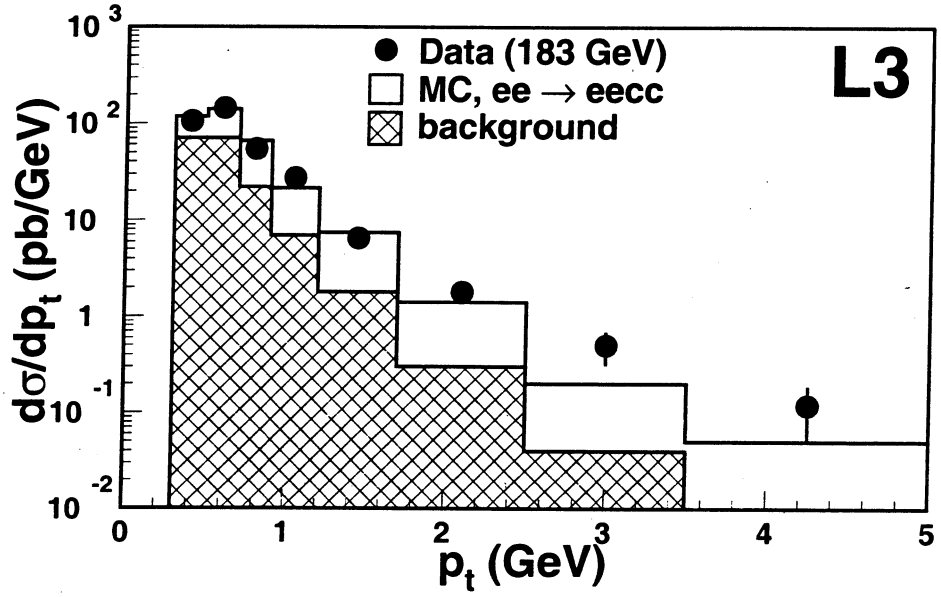

Figure 5.24: The differential cross section for inclusive electrons at $\sqrt{s} = 183$ GeV as a function of the electron transverse momentum. The data are compared to the total PYTHIA Monte Carlo predictions scaled to the observed cross section. The shaded area shows the non-charm two-photon events background. The cross section is given for the kinematic range defined in the text.

In Figure 5.24, the differential cross section at 183 GeV is plotted as a function of the transverse momentum of the electron. The prediction from the PYTHIA Monte Carlo for the inclusive charm production and for the background (both normalized to the number of data events) is also shown. The shape of the distribution is in agreement with the prediction. Leptons from semileptonic decays of charm quarks are on average more energetic than

leptons from non-charm two-photon processes, therefore the charm purity increases with the transverse momentum. Although the statistical errors are large, there appears to be an excess in the data at high values of p_t. This excess may be due to beauty production, or perhaps the PYTHIA Monte Carlo is not generating enough resolved process events.

5.4.2 Inclusive Muon Cross Section

The inclusive muon cross section is calculated for $|\cos\theta| < 0.9$, a momentum greater than 2 GeV and $W_{\gamma\gamma} > 3$ GeV. The measured cross sections,

Table 5.10: Inclusive muon cross section. Data samples were collected by L3 from 1994 to 1997 at $\sqrt{s}$ = 91-183 GeV at the corresponding integrated luminosities $\mathcal{L}$. The number of events selected with the muon tag in the data, $N_{observed}$, is given with the number of expected events,$N_{observed}$, predicted by the Monte Carlo. The inclusive muon cross section $\Delta\sigma$ is calculated after the subtraction of annihilation and $e^+e^- \to e^+e^-\tau^+\tau^-$ background in the polar angle region $|\cos\theta| < 0.9$, for a momentum greater than 2.0 GeV and with $W_{\gamma\gamma} > 3$ GeV. The first error is statistical and the second one is systematic.

$\sqrt{s}$	$\mathcal{L}$	Muon Tag		
[GeV]	[pb^{-1}]	$N_{observed}$	$N_{expected}$	$\Delta\sigma_\mu$ [pb]
91	79.8	57	47	1.64 ±0.30±0.08
161 – 172	21.2	16	16	2.31 ±0.63±0.12
183	52.2	52	35.3	3.33 ±0.49±0.16

$\Delta\sigma_\mu$, are given in Table 5.10 along with the statistical and systematic errors. Systematic errors arise from the uncertainty on background subtraction, selection efficiency, trigger efficiency and cut variation. The statistical error is dominant for this measurement.

CHAPTER 6

RESULTS

The inclusive charm production in two-photon collisions has been measured for the first time at LEP2 energies by the L3 experiment [50]. The L3 results are compared with the previous cross section measurements made by experiments at PEP, PETRA, TRISTAN and LEP [12, 13, 14, 15, 16, 17, 18]. All measurements are plotted with the theoretical prediction to next-to-leading order (NLO) accuracy for the direct process ($\gamma\gamma \rightarrow c\bar{c}$) alone and for the Quantum Chromodynamics (QCD) prediction which includes contributions from resolved photons.

6.1 Total Inclusive Charm Cross Section

The total cross section of inclusive charm production is calculated from the following equation:

$$\sigma = \frac{(N_{obs}^{lept} - N_{bkg}^{lept})\ \pi_c}{\mathcal{L}\ \epsilon_{trig}\ \epsilon_c'}. \tag{6.1}$$

N_{obs}^{lept} is the final number of selected events in the data for either the electron or muon tag. N_{bkg}^{lept} is the background from non-hadronic two-photon sources remaining after the electron or muon tag. The charm selection efficiency, ϵ_c', is the fraction of charm events selected by the lepton tag analysis relative to the events generated in the full phase space. The charm purity, π_c, is defined as:

$$\pi_c = \frac{N_c^{lept}}{N_c^{lept} + N_{nc}^{lept}}. \tag{6.2}$$

N_c^{lept} (N_{nc}^{lept}) is the final number of selected charm (non-charm) events by either the electron or muon tag as estimated by PYTHIA. In order to be less dependent on the Monte Carlo flavor composition (charm to non-charm fraction), the charm purity can be rewritten as:

$$\pi_c = (1 - \frac{\epsilon_{nc}}{\epsilon_d})/(1 - \frac{\epsilon_{nc}}{\epsilon_c}), \tag{6.3}$$

where the ϵ_c (ϵ_{nc}) is the fraction of charm N_c^{lept} (non-charm N_{nc}^{lept}) events, accepted by the final selection, from the charm (non-charm) events obtained after the hadronic selection. The Monte Carlo estimate with the electron tag for ϵ_c is about 1.5% at all center-of-mass energies, while ϵ_{nc} is a full order of magnitude smaller. The quantity ϵ_d is defined by the relation:

$$\epsilon_d = \frac{N_c^{lept} + N_{nc}^{lept}}{N_c^{had} + N_{nc}^{had}} = \frac{N_{obs}^{lept} - N_{bkg}^{lept}}{N_{obs}^{had} - N_{bkg}^{had}} \tag{6.4}$$

and can thus be determined directly from the data. N_{obs}^{had} is the number of data events obtained after the hadronic two-photon selection. N_{bkg}^{had} is the background from non-hadronic two-photon sources. The values for ϵ_d ranged from 0.29% at $\sqrt{s} = 91$ GeV to 0.36% at $\sqrt{s} = 183$ GeV for the electron tag. Equation 6.4 is obtained by noticing that the total number of selected hadronic events $N_c^{had} + N_{nc}^{had}$ can be expressed as:

$$\frac{N_c^{lept} + N_{nc}^{lept}}{\epsilon_d} = \frac{N_c^{lept}}{\epsilon_c} + \frac{N_{nc}^{lept}}{\epsilon_{nc}}. \tag{6.5}$$

This method of deriving the charm cross section is insensitive to the absolute normalization of the charm and background Monte Carlo, but still depends on the ratio of direct to resolved process in the signal Monte Carlo.

Table 6.1: Summary of the charm analysis by the electron tag for the data collected at $\sqrt{s} = 91 - 183$ GeV . The column elements from left to right are the center-of-mass energy, the integrated luminosity, the events selected by the electron tag (N^e_{obs}), the background from sources other than two-photon hadronic interactions (N^e_{bkg}), the charm purity (π^e_c) and the charm selection efficiency ($\epsilon^{e\prime}_c$), respectively.

$\sqrt{s}$ $[GeV]$	$\mathcal{L}$ $[pb^{-1}]$	N^e_{obs} Events	N^e_{bkg} Events	π^e_c [%]	$\epsilon^{e\prime}_c$ $[10^{-2}\%]$
91	79.8	282	29.5	50.5 ± 4.9	42.2 ± 3.4
$130 - 140$	12.1	82	0.5	70.0 ± 3.4	42.0 ± 4.0
$161 - 172$	21.2	156	1.5	60.0 ± 3.2	52.6 ± 3.3
183	52.2	433	4.1	65.9 ± 2.2	53.3 ± 2.6

The charm purity and the charm selection efficiency for electrons and muons[1] are given in Tables 6.1 and 6.2. The purity calculated with the use of ϵ_d from the data gives on average a value about 10% higher than the estimate using only the Monte Carlo.

Table 6.2: Summary of the charm analysis by the muon tag for the data collected at $\sqrt{s} = 91 - 183$ GeV . The column elements from left to right are the center-of-mass energy, the integrated luminosity, the events selected by the muon tag (N^μ_{obs}), the background from sources other than two-photon hadronic interactions (N^μ_{bkg}), the charm purity (π^μ_c) and the charm selection efficiency ($\epsilon^{\mu\prime}_c$), respectively.

$\sqrt{s}$ $[GeV]$	$\mathcal{L}$ $[pb^{-1}]$	N^μ_{obs} Events	N^μ_{bkg} Events	π^μ_c [%]	$\epsilon^{\mu\prime}_c$ $[10^{-2}\%]$
91	79.8	57	15.9	70.6 ± 8.8	6.43 ± 1.10
$161 - 172$	21.2	16	1.41	48.3 ± 10.1	6.48 ± 1.01
183	52.2	52	1.38	61.7 ± 6.8	5.59 ± 0.83

[1] Besides charm quark semileptonic decays other sources of electrons and muons are the decays $\tau^+ \to l^+\nu_l\bar{\nu}_\tau, \pi^+ \to \mu^+\nu_\mu, \pi^0 \to e^+e^-\gamma, K^+ \to \mu^+\nu_\mu, l^+\pi^0\nu_l, K^0_L \to l^+\pi^-\nu_l, ...$

Table 6.3: Total cross section values for the process $e^+e^- \to e^+e^- c\bar{c}X$ at four different energies using electron and muon identification. The statistical and systematic uncertainties are also given. In the last column, the data from both lepton tags are combined.

$\sqrt{s}$ [GeV]	Electron Tag σ [pb]	Muon Tag σ [pb]	Combined σ [pb]
91	$435 \pm 64 \pm 76$	$601 \pm 168 \pm 164$	$459 \pm 60 \pm 75$
133	$1358 \pm 243 \pm 180$	–	$1358 \pm 243 \pm 180$
167	$1009 \pm 152 \pm 106$	$576 \pm 361 \pm 197$	$936 \pm 140 \pm 100$
183	$1291 \pm 105 \pm 122$	$1260 \pm 328 \pm 246$	$1287 \pm 100 \pm 114$

The cross sections are given in Table 6.3 with statistical and systematic uncertainties. The statistical error is determined only for the final number of events in the data, because the statistical uncertainty due to the hadronic selection makes a negligible contribution as $N_{obs}^{had} \gg N_{obs}^{lept}$. The fractional statistical uncertainty is calculated by:

$$\frac{\Delta\sigma_{stat}}{\sigma_{stat}} = \frac{\sqrt{N_{obs}^{lept}}}{\pi_c(N_{obs}^{lept} - N_{bkg}^{lept})}\left(\frac{1}{1-\epsilon_{nc}/\epsilon_c}\right) \approx \frac{1}{\pi_c\sqrt{N_{obs}^{lept}}}. \qquad (6.6)$$

A main source of systematic error for the electron sample is from the cut variation, from 9.5% at $\sqrt{s} = 91$ GeV to 6.5% at $\sqrt{s} = 183$ GeV. Each selection cut was changed individually in the direction which favored rejecting more background. The number of observed events, the background, the charm purity and the charm selection efficiency were recalculated to determine the effect on the cross section measurement. The cut variation was small and chosen by eye with regard to the signal and background distributions. For example, the cut on the momentum of the electron candidate was increased from 0.6 GeV to 0.65 GeV. The cuts made on the E_t/p_t distribution

were tightened individually to narrow the selection window for the electron peak, and the average of the two cut variations was calculated. The signal and background distributions shown in the plots of E_1/E_9 and χ^2 are not as cleanly separated, so the cuts were varied in both directions and the average was taken. For example, the cut on E_1/E_9 was varied from 0.45 to 0.55.

The estimates for the systematic errors are sensitive to the statistical sample in both the data and the Monte Carlo. The amount of data is a fixed quantity, but the Monte Carlo can be produced in multiples of the integrated luminosity available in the data. There are diminishing returns in generating larger and larger Monte Carlo samples as the statistical uncertainty falls as $1/\sqrt{N}$. In addition, there are limitations to the time available to generate and reconstruct large quantities Monte Carlo and to the capacity to store it. To estimate the effect of the Monte Carlo statistics on the systematic error, the cross section and the uncertainties were recalculated using Monte Carlo samples that were about one-half and one-quarter the size. This effect was considered in order not to overestimate the total systematic uncertainty in the cross section measurement.

Additional systematic errors arise from the uncertainty on the background subtraction, the selection efficiencies, the trigger efficiency and the charm semileptonic branching ratio. The average charm semileptonic branching ratio used in the simulation is 0.098 ± 0.005 [49]. The systematic errors are added in quadrature (Tables 6.4 and 6.5). The dominant systematic error for the muon tag comes from selection efficiencies, from 24% at $\sqrt{s} = 91$ GeV to 18% at $\sqrt{s} = 183$ GeV.

Table 6.4: Systematic errors for the inclusive charm cross section measurement by the electron tag. The different contributions are given in [pb] and added in quadrature for the total systematic error.

$\sqrt{s}$ [GeV]	91	130-140	161-172	183
Charm purity	42.2	66.8	54.5	42.6
Charm selection eff.	35.0	129.3	63.6	63.3
Background	28.7	20.2	15.0	10.3
Trigger efficiency	4.8	40.5	22.2	18.1
Visible mass cut	32.0	100.8	14.0	64.6
Visible energy cut	2.6	0.7	0.1	9.0
E_{Lumi}/E_{Beam} cut	6.5	14.4	2.0	1.0
Momentum cut	0.1	28.0	20.0	25.8
Polar angle cut	8.7	42.0	30.0	19.4
Other electron cuts	37.0	62.7	44.8	43.6
Branching ratio	13.0	40.8	30.3	38.7
TOTAL	76	180	106	122

Table 6.5: Systematic errors for the inclusive charm cross section measurement by the muon tag. The different systematic sources are given in [pb] and added in quadrature for the total systematic error.

$\sqrt{s}$ [GeV]	91	161-172	183
Charm purity	74.5	121.0	139.0
Charm selection eff.	103.0	90.0	186.0
Background	15.0	22.0	13.0
Trigger efficiency	6.6	12.0	18.0
Visible mass cut	12.2	44.0	17.0
Visible energy cut	97.0	51.0	43.0
E_{Lumi}/E_{Beam} cut	0.1	87.0	0.1
Muon cut variation	24.2	11.0	50.1
Branching ratio	18.0	17.3	37.8
TOTAL	164	188	246

The charm production cross sections are obtained with the PYTHIA Monte Carlo using a massless quark matrix element calculation. The effect of the use of massive matrix elements is tested by using the PYTHIA Monte Carlo events generated with the charm mass $m_c = 1.6$ GeV. Since the cross section values are dependent on the ratio of the charm purity to the charm selection efficiency, π_c/ϵ'_c, we compare the value of this ratio using the massless matrix elements to the ratios obtained from the massive matrix elements approach. Within statistics they are the same. The change of the direct to resolved process ratio in the signal Monte Carlo by a factor 1.2 (1.4) results in a change of the charm cross section by 3.4% (6%) for electrons and has negligible effect for muons.

The PYTHIA Monte Carlo is the only generator available which includes all hadronic two-photon processes relevant in this analysis. The QED JAMVG program generates only the direct process. To better understand possible systematics due to the different models, we have compared the values of π_c/ϵ'_c for the direct process as given by PYTHIA and by JAMVG. There is agreement within 10% which is comparable with the statistical uncertainty. However, for low momenta as seen in the case of the electron selection, the value of π_c/ϵ'_c for the direct process is two times higher than that for the resolved process.

The total inclusive charm production cross sections are plotted in Figure 6.1 together with previous measurements [12, 13, 14, 15, 16, 17, 18]. For the purpose of comparison, the published results of different experiments were extrapolated to the total charm cross sections using the procedure of

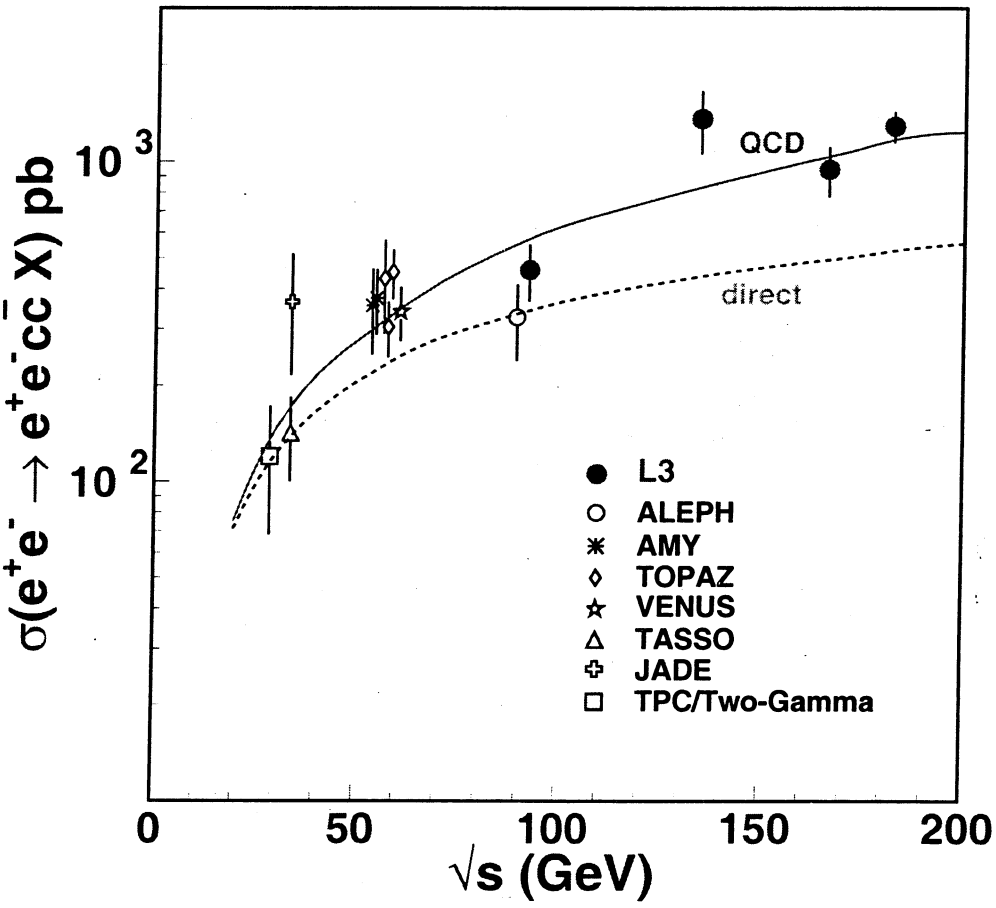

Figure 6.1: The charm production cross section in two-photon collisions. The L3 data from both the electron and the muon events are combined. The statistical and systematic errors are added in quadrature. The dashed line corresponds to the direct process prediction while the solid line shows the QCD prediction for the sum of the direct and the resolved processes calculated to NLO accuracy [11]. The prediction corresponds to a calculation for a charm quark mass of 1.3 GeV, the parton density function of Glück-Reya-Vogt [26] and the renormalization scale was chosen to be the charm quark mass. Points at $\sqrt{s} = 58$ GeV and $\sqrt{s} = 91$ GeV energies are artificially separated for clear visibility.

Ref. [51]. The data are compared to the predictions of Ref. [11]. The dashed line corresponds to the direct process, NLO QCD calculations, while the solid line shows the QCD prediction for the sum of direct and resolved processes calculated to NLO accuracy. The direct process depends upon the heavy quark mass and the QCD coupling constant. The prediction is calculated using a charm mass of 1.3 GeV; the open charm threshold energy is set to 3.8 GeV. The renormalization scale was chosen to be the charm mass. A change in the renormalization scale from m_c to $2m_c$ decreases the QCD prediction by 30% (15%) for $m_c = 1.3$ (1.7) GeV. The uncertainties in the calculations indicate that it is not possible to determine the mass of the charm quark simply by measuring the total charm cross section.

6.2 Direct and Resolved Contributions

The most sensitive distributions where predictions for direct and resolved processes are different are found to be the visible mass, the track multiplicity, the transverse momentum of the lepton and the energy flow spectra. In the resolved process, the probing photon interacts with a parton in the target photon. The remaining quarks and gluons from the target photon form a remnant jet which leaves with some energy fraction of the two-photon system. The presence of a remnant jet adds to the average track multiplicity per event while subtracting from the average p_t of the lepton candidates.

A comparison of the visible mass and track multiplicity distributions in the data with the expectations of the direct, resolved and all two-photon processes for the high statistics electron sample at $\sqrt{s} = 183$ GeV is given in

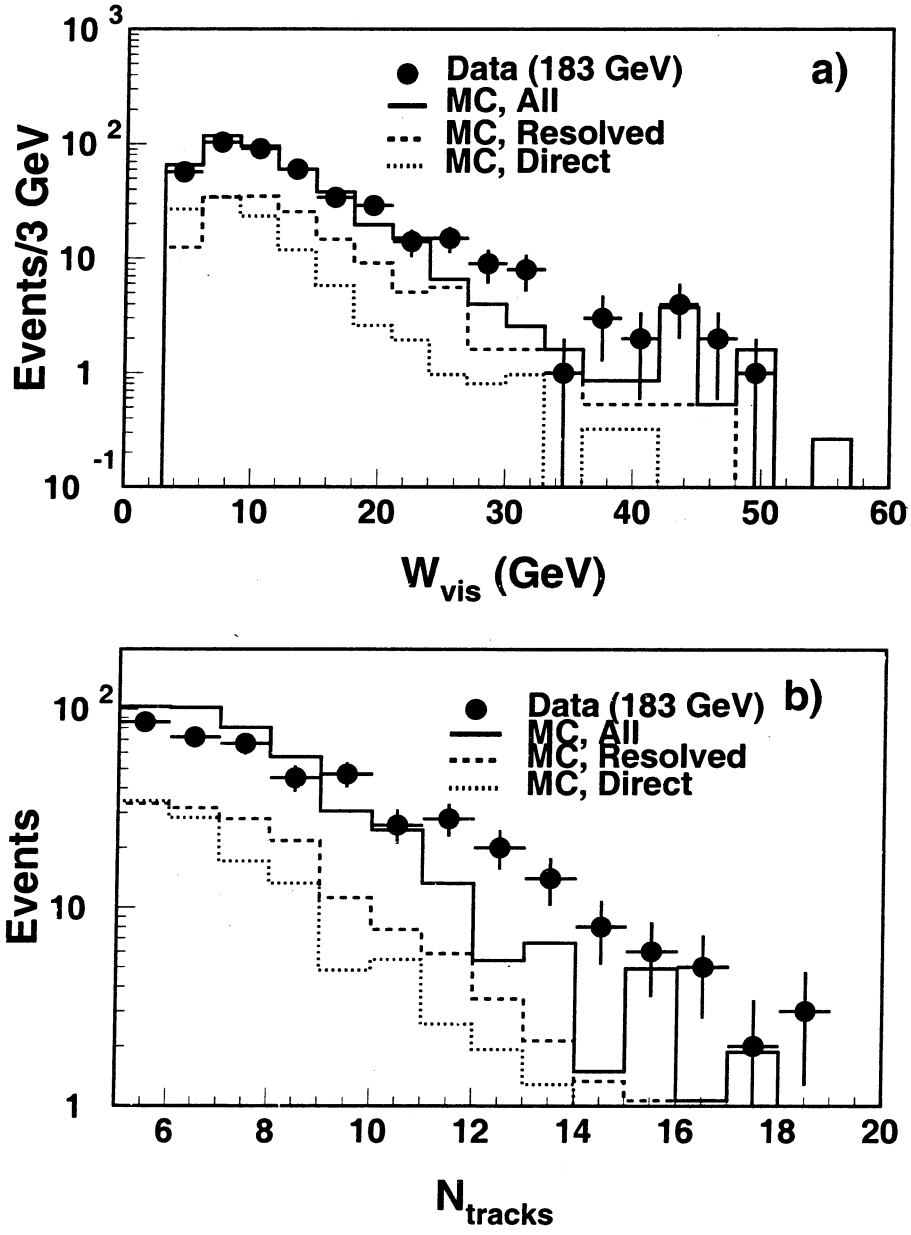

Figure 6.2: Distributions of a) the visible mass spectrum and b) the track multiplicity for the inclusive electron data at $\sqrt{s} = 183$ GeV compared to PYTHIA events generated with massless matrix elements. The Monte Carlo spectrum with all contributions is normalized to the same number of events as the data. The dashed and dotted histograms show the contributions from the resolved and direct process respectively.

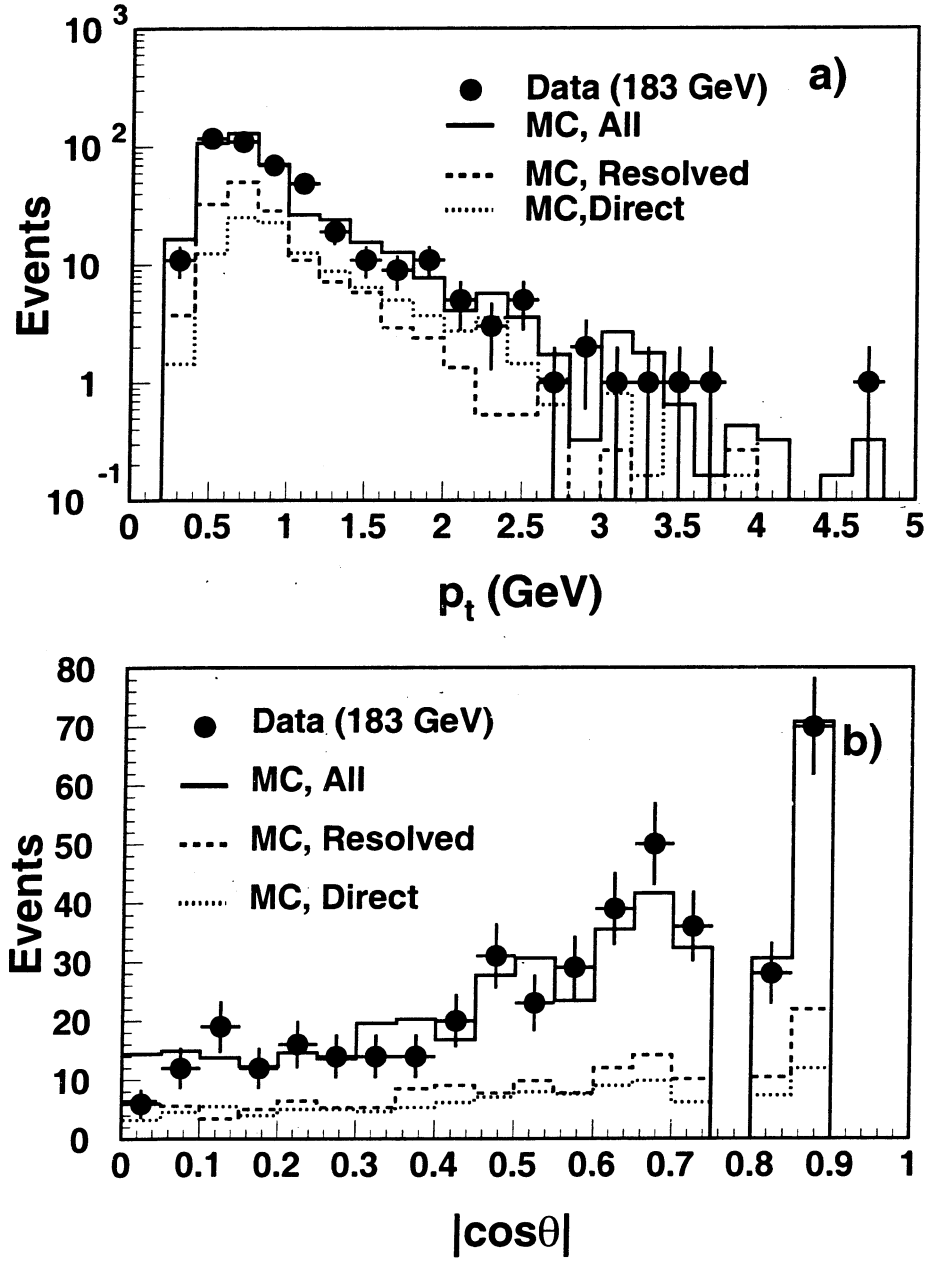

Figure 6.3: Distributions of a) the transverse momentum and b) the polar angle for the inclusive electron data at $\sqrt{s} = 183$ GeV compared to PYTHIA. The Monte Carlo spectrum with all contributions is normalized to the same number of events as the data. The dashed and dotted histograms show the contributions from the resolved and direct process respectively.

Figures 6.2a-b. The direct process decreases more quickly than the resolved process with increasing visible mass and track multiplicity.

A comparison of the transverse momentum and polar angle distributions in the data with the expectations of the direct, resolved and all two-photon processes for the high statistics electron sample at $\sqrt{s} = 183$ GeV is given in Figures 6.3a,b. The resolved process peaks at smaller values of p_t and decreases more quickly than the direct process. There is no discernible difference in the polar angle distributions between the direct or resolved process.

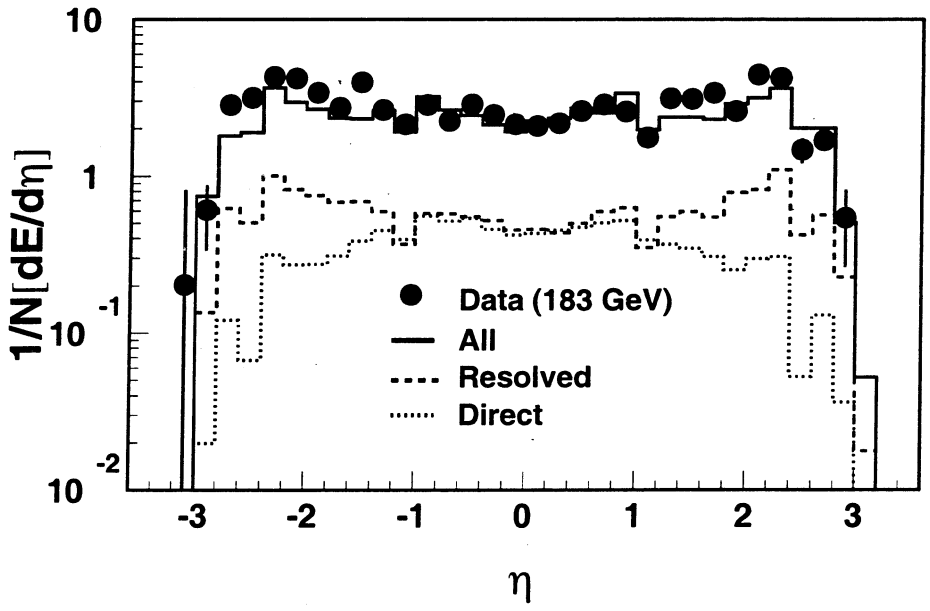

Figure 6.4: Energy flow as a function of pseudorapidity η. The data are compared to the PYTHIA prediction with all contributions (solid histogram) and to the resolved and direct processes separately (dashed and dotted histograms, respectively).

In Figure 6.4, we plot the average event energy deposited in the calorimeters in GeV, or *energy flow*, in bins of the pseudorapidity, $\eta = -\ln(\tan(\frac{\theta}{2}))$,

where θ is the polar angle of the particle. The data from the final electron tag selection is plotted against the full Monte Carlo prediction which includes contributions from direct and resolved processes as well as VDM. About one-third of the final event sample are a result of light quark (u,d,s) decay. Through the direct process, a $c\bar{c}$ are produced. The charm quarks are not bound and will decay, producing two collinear jets of large transverse momentum with respect to the incident photons. The jets are found predominantly in the barrel. The resolved process is similar to the direct process except for the remnant jet. The remaining partons, or photon remnant, of the target photon will produce a jet along the direction of the target photon. This jet will be at small angles typically $|\eta| > 1$. A clear difference in shape can be seen between the distributions for the direct and resolved processes for $|\eta| > 1$. However, the contribution from VDM is considerable. Therefore, a three-parameter fit would be necessary to extract information about the gluon content of the photon in the resolved processes.

CHAPTER 7

SUMMARY AND OUTLOOK

The cross section for inclusive charm production in two-photon collisions, $\sigma(e^+e^- \rightarrow e^+e^-c\bar{c}X)$, is measured with the L3 detector at 91 GeV $\leq \sqrt{s} \leq$ 183 GeV. The cross section increases with energy as expected by QCD predictions [11]. The current version of PYTHIA does not include NLO corrections. The number of observed events exceed the prediction by as much as 60% at $\sqrt{s} = 183$ GeV. Therefore, the next generation of Monte Carlo generators will need to include at least NLO corrections to the QCD processes.

The direct process $\gamma\gamma \rightarrow c\bar{c}$ is insufficient to describe the data, even if the real and virtual gluon corrections are included. This is shown in Figure 6.1 where the L3 cross section measurements exceed the NLO direct prediction. The cross sections and the event distributions require contributions from the resolved processes which are dominantly $\gamma g \rightarrow c\bar{c}$. The data therefore require a significant gluon content in the photon.

One objective is to measure the direct contribution of the charm cross section which is not dependent on the renormalization scale. An accurate measurement of the direct production would constrain the charm mass. The distributions for the visible mass and the transverse momentum (Figures 6.2 and 6.3a) show that the spectrum for direct and resolved events have a somewhat different kinematical evolution. However, any cuts made on these two variables to get a sample of events which is mostly from direct production would reduce the statistics significantly. So the positive of removing the un-

Table 7.1: Total cross section values for the process $e^+e^- \rightarrow e^+e^-c\bar{c}X$ at $\sqrt{s} = 189$ GeV using electron and muon identification. The statistical and systematic uncertainties are also given. In the last column, the data from both leptons are combined.

$\sqrt{s}$	Electron Tag	Muon Tag	Combined
[GeV]	σ [pb]	σ [pb]	σ [pb]
189	$1599 \pm 60 \pm 174$	$1077 \pm 144 \pm 152$	$1378 \pm 55 \pm 134$

certainty on the renormalization scale is lost to the statistical error. Another possibility is to model the total cross section as the sum of a direct and resolved component. Performing a fit to determine the relative amounts of each process is a task for the immediate future.

The data used in this analysis was taken by the L3 experiment from 1994 through 1997 when LEP reached a record center-of-mass energy (for e^+e^- colliders) of 183 GeV. At this energy, two-photon collisions are the dominant physics process where the cross section grows like $(\ln (s/m^2_{electron}))^2$. The 433 events, which were selected by the electron tag of charm production at $\sqrt{s} = 183$ GeV, was the highest statistical sample obtained. In 1998, LEP increased the center-of-mass energy to 189 GeV. The data collected by L3 with a total integrated luminosity of 176 pb^{-1} at $\sqrt{s} = 189$ GeV is about 3.4 times as much as was collected at $\sqrt{s} = 183$ GeV.

The charm production has already been studied at $\sqrt{s} = 189$ GeV, and preliminary results were presented at three conferences [52, 53, 54] in 1999. Nearly 400,000 hadronic two-photon events were selected, compared to less than 120,000 at $\sqrt{s} = 183$ GeV. Using the identical selection of charm quark events through semileptonic decay, 1710 electron and 208 muon events re-

Table 7.2: Total cross section values for the process $e^+e^- \to e^+e^-b\bar{b}X$ at $\sqrt{s} = 189$ GeV using electron and muon identification. The statistical and systematic uncertainties are also given. In the last column, the data from both leptons are combined.

$\sqrt{s}$	Electron Tag	Muon Tag	Combined
[GeV]	σ [pb]	σ [pb]	σ [pb]
189	$9.5 \pm 3.6 \pm 4.1$	$10.3 \pm 4.6 \pm 3.3$	$9.9 \pm 2.9 \pm 3.8$

main. This is a statistical increase of nearly 400% from the $\sqrt{s} = 183$ GeV results. The cross section measurements for $\sqrt{s} = 189$ GeV are given in Table 7.1. The combined lepton result is plotted with the four published values [50] in Figure 7.1. The result is consistent with NLO QCD prediction. With this large sample of events, a separation of direct and resolved processes should be made leading to a possible measurement of the charm mass.

With the larger statistics and center-of-mass energy, beauty production in two-photon collisions is being measured for the first time. Using additional constraints on the lepton momentum and the p_t of the lepton with respect to the nearest jet, the beauty production can be measured. Preliminary cross section values are given in Table 7.2 and were presented at PHOTON99 [54]. The beauty cross section is plotted in Figure 7.1 with the prediction assuming a mass of 5 GeV. The main uncertainty is statistical. This topic has been chosen for the thesis of LSU student Sepehr Saremi.

Finally, LEP is currently running at even higher energies. In 1999, LEP will deliver about 200 pb^{-1} of luminosity at $\sqrt{s} = 190 - 200$ GeV, and the same is expected in the year 2000. This will more than double the data taken at $\sqrt{s} = 183$ and 189 GeV.

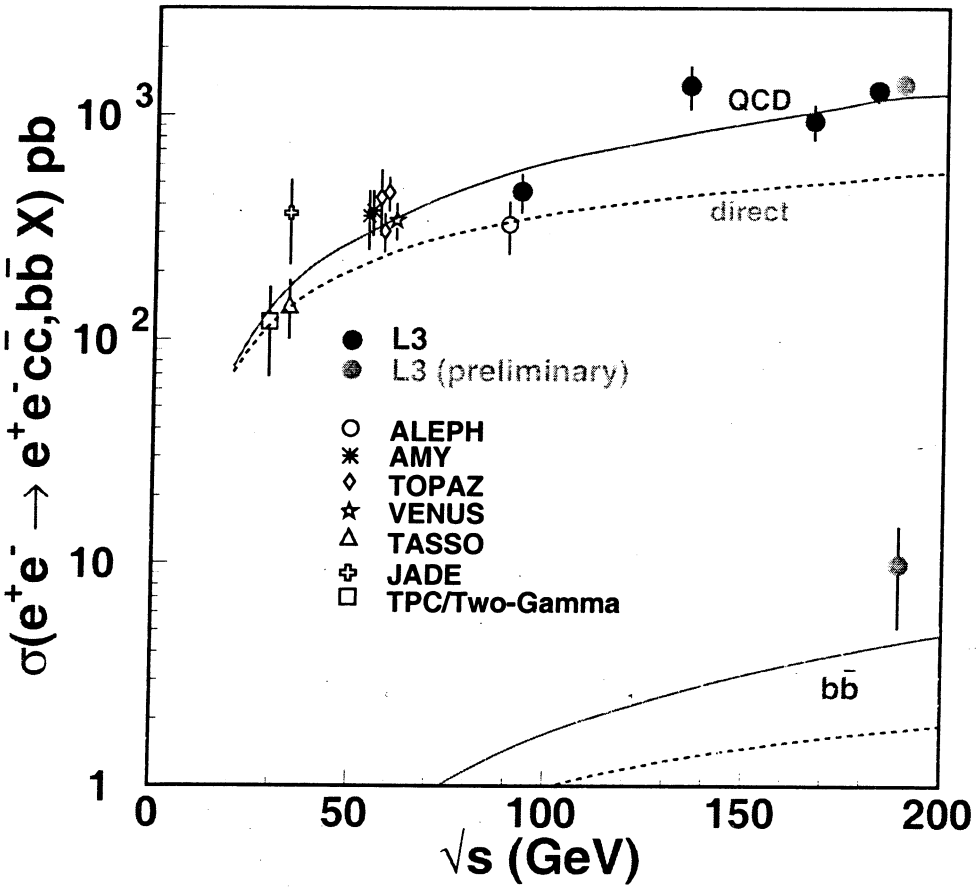

Figure 7.1: The charm and beauty production cross section in two-photon collisions at $\sqrt{s} = 189$ GeV. The L3 data from both the electron and the muon events are combined. The statistical and systematic errors are added in quadrature. The dashed line corresponds to the direct process prediction while the solid line shows the QCD prediction for the sum of the direct and the resolved processes calculated to NLO accuracy [11]. The prediction corresponds to a calculation for a charm (beauty) quark mass of 1.3 GeV (5.0 GeV), the parton density function of Glück-Reya-Vogt [26] and the renormalization scale was chosen to be the charm quark mass. Points at $\sqrt{s} = 58$ GeV and $\sqrt{s} = 91$ GeV energies are artificially separated for clear visibility. The charm and beauty measurements at 189 GeV are preliminary.

BIBLIOGRAPHY

[1] *LEP design report, vol I, The LEP Injector Chain*, CERN-LEP-TH/83-29 (1983);
LEP design report, vol II, The LEP Main Ring, CERN-LEP-TH/84-01 (1984);
I. Wilson and H. Henke, *The LEP Main Ring Accelerating Structure*, CERN/89-09, CERN, 1989.

[2] D. DeCamp *et al.*, Nucl. Inst. and Meth. **A294** (1990) 127.

[3] P. Aarnio *et al.*, Nucl. Inst. and Meth. **A303** (1991) 233.

[4] B. Adeva *et al.*, Nucl. Inst. and Meth. **A289** (1990) 35;
O. Adriani *et al.*, Phys. Rep. **236** (1993) 1;
M. Acciari *et al.*, Nucl. Inst. and Meth. **A351** (1994) 300;
M. Acciari *et al.*, Nucl. Inst. and Meth. **A360** (1995) 103.

[5] K. Ahmet *et al.*, Nucl. Inst. and Meth. **A305** (1991) 275.

[6] A.A. Zholentz *et al.*, Phys. Lett. **B96** (1980) 214;
A.S. Artamonov *et al.*, Phys. Lett. **B118** (1982) 225;
D.P. Barber *et al.*, Phys. Lett. **B135** (1984) 498;
W.W. McKay *et al.*, Phys. Rev. **D29** (1984) 2483;
A.N. Skrinskii and Yu.M. Shatunov, Sov. Phys. Usp. **32(6)** (1989) 548.

[7] L. Arnaudon *et al.*, *The Energy Calibration of LEP in 1991*, Preprint CERN-SL/92-37-DI and CERN-PPE/92-125, CERN, 1992;
L. Arnaudon *et al.*, *The Energy Calibration of LEP in 1992*, Preprint CERN-SL/93-21-DI, CERN, 1993;
L. Arnaudon *et al.*, *Accurate Determination of the LEP Beam Energy by Resonant Depolarization*, Preprint CERN-SL/94-71-BI, CERN, 1994;
L. Arnaudon *et al.*, *The Energy Calibration of LEP in 1993 Scan*, Preprint CERN-SL/95-02, CERN, 1995.

[8] A. Blondel *et al.*, *Beam Measurement at LEP2*, Preprint CERN-SL/92-37-DI and CERN-PPE/92-125, CERN, 1992;
The LEP Energy Working Group, *LEP Energy Calibration in 1996*, LEP Energy Group/97-01, CERN, 1997.

[9] B. Dhning *et al.*, *A Study of the Magnetic Field of LEP during the 1995 Energy Scan*, CERN-SL/96-54-BI, CERN, 1996.

[10] The LEP Energy Working Group, *LEP Energy Calibration above the W Pair Production Threshold*, LEP-ECAL/98-02 and ICHEP/98-352, CERN, 1998.

[11] M. Drees, M. Krämer, J. Zunft and P.M. Zerwas, Phys. Lett. B **306**, (1993) 371.

[12] JADE Collab., W. Bartel *et al.*, Phys. Lett. B **184**, (1987) 288.

[13] TPC/Two-Gamma Collab., M. Alston-Garnjost *et al.*, Phys. Lett. B **252**, (1990) 499.

[14] TASSO Collab., W. Braunschweig *et al.*, Z. Phys. C **47**, (1990) 499.

[15] TOPAZ Collab., R. Enomoto *et al.*, Phys. Lett. B **328**, (1994) 535, Phys. Rev. D **50**, (1994) 1879, Phys. Lett. B **341**, (1994) 99, Phys. Lett. B **341**, (1994) 238.

[16] VENUS Collab., S. Uehara *et al.*, Z. Phys. C **63**, (1994) 213.

[17] AMY Collab., T. Aso *et al.*, Phys. Lett. B **363**, (1995) 249, Phys. Lett. B **381**, (1996) 372.

[18] ALEPH Collab., D. Buskulic *et al.*, Phys. Lett. B **255**, (1995) 595.

[19] M. Cacciari *et al.*, in CERN 96-01 Physics at LEP2, edited by G. Altarelli, (1996), v.2, p. 205.

[20] H1 Collab., S. Aid *et al.*, Z. Phys. C **69**, (1995) 27;
ZEUS Collab., M. Derrick *et al.*, Z. Phys. C **63**, (1994) 391;
Proc. Workshop on HERA Physics, Durham, 1995, J. Phys. **G22** (1996).

[21] T. Sjöstrand, Comput. Phys. Commun. **82**, (1994) 74.

[22] V. M. Budnev *et al.*, Phys. Rep. **15** (1975) 181.

[23] G.A. Schuler and T. Sjöstrand, Phys. Lett. B **300**, (1993) 169;
G.A. Schuler and T. Sjöstrand, Nucl. Phys. B **407**, (1993) 539;
G.A. Schuler and T. Sjöstrand, Z. Phys. C **73**, (1997) 677.

[24] G.A. Schuler and T. Sjöstrand, Z. Phys. C **68**, (1995) 607; Phys. Lett. B **376**, (1996) 193.

[25] M. Drees and K. Grassie, Z. Phys. C **28**, (1985) 451.

[26] M. Glück, E. Reya and A. Vogt, Phys. Rev. D **46**, (1992) 1973.

[27] M. Krämer, *Proceedings on Two-Photon Collisions at PHOTON '95*, Sheffield, England (1995), 111.

[28] H. Akbari *et al.*, Nucl. Inst. and Meth. **A315** (1992) 161;
G.M. Viertel *et al.*, Nucl. Inst. and Meth. **A323** (1992) 399;
F. Beissel *et al.*, Nucl. Inst. and Meth. **A332** (1993) 33.

[29] A. Arefiev *et al.*, Nucl. Inst. and Meth. **A275** (1989) 71;
A. Arefiev *et al.*, Nucl. Inst. and Meth. **A285** (1989) 403;
O. Adriani *et al.*, Nucl. Inst. and Meth. **A302** (1991) 53.

[30] B. Adeva *et al.*, Nucl. Inst. and Meth. **A277** (1989) 187;
B. Adeva *et al.*, Nucl. Inst. and Meth. **A323** (1992) 109.

[31] A. Adam *et al.*, Nucl. Inst. and Meth. **A383** (1996) 342.

[32] I.C. Brock *et al.*, Nucl. Inst. and Meth. **A381** (1996) 236.

[33] P. Bagnaia *et al.*, Nucl. Inst. and Meth. **A317** (1992) 463;
P. Bagnaia *et al.*, Nucl. Inst. and Meth. **A324** (1993) 101.

[34] R. Bizzari *et al.*, Nucl. Inst. and Meth. **A283** (1989) 799;
P. Bagnaia *et al.*, Nucl. Inst. and Meth. **A324** (1993) 101;
P. Bagnaia *et al.*, Nucl. Inst. and Meth. **A344** (1994) 212.

[35] P. Béné *et al.*, Nucl. Inst. and Meth. **A306** (1991) 150.

[36] G. Carlino *et al.*, L3 Internal Note **1951**, (1997).

[37] Y. Bertsch *et al.*, Nucl. Inst. and Meth. **A340** (1994) 309;
S.P. Beingessner *et al.*, Nucl. Inst. and Meth. **A340** (1994) 322.

[38] C. Diobisi *et al.*, Nucl. Inst. and Meth. **A336** (1993) 78.

[39] S. Banerjee and F. Bruyant, L3 Internal Note **748**, 1989.

[40] M. Cacciari et al., Nucl. Phys. B **466**, (1996) 173.

[41] J.A.M. Vermaseren, Nucl. Phys. B **229**, (1983) 347.

[42] T. Sjöstrand, Comput. Phys. Commun. **39**, (1986) 347;
T. Sjöstrand and M. Bengtsson, Comput. Phys. Commun. **43**, (1987) 367.

[43] S. Jadach, B.F.L. Ward and Z. Was, Comput. Phys. Commun. **79**, (1994) 503.

[44] M. Skrzypek, S. Jadach, W. Placzek and Z. Was, Comput. Phys. Commun. **94**, (1996) 216.

[45] R. Burn *et al.*, GEANT3 *User Guide*, CERN-DD-EE/84-1.

[46] H. Fesefeldt, *The Simulation of Hadronic Showers: Physics and Applications*, RWTH, Aachen, PITHA 85/02 (1985).

[47] B. Adeva *et al.*, Nucl. Inst. and Meth. **A289** (1990) 35.

[48] B. Adeva *et al.*, Nucl. Inst. and Meth. **A309** (1991) 318.

[49] The LEP Experiments: ALEPH, DELPHI, L3 and OPAL, Nucl. Inst. Meth. **A 378** (1996) 101.

[50] M. Acciarri *et al.*, Phys. Lett. B **453**, (1999) 83.

[51] M. Cacciari *et al.*, in CERN 96-01 Physics at LEP2, edited by G. Altarelli, (1996), v.1, p. 334.

[52] A. Stone, Centennial Meeting of the American Physical Society, Atlanta, GA, USA, 20-26 March 1999.

[53] V. Andreev, DIS99 - The 7th International Workshop on Deep Inelastic Scattering and QCD, DESY Zeuthen, Germany, April 19-23 1999.

[54] R. McNeil, PHOTON 99 - International Conference on the Structure and Interactions of the Photon, Freiburg im Breisgau, Germany, May 23-26 1999.

[55] U. Uwer, L3 Internal Note **2003**, (1996).

APPENDIX

SCINTILLATORS

A.1 Introduction

Louisiana State University shares the responsiblity with the Physics Institute from Aachen, Germany in maintaining the performance of the scintillation subdetector. The counters measure the time of the particles passing through the detector with respect to the beam crossing time. This timing information is then used to select high multiplicity events and to reject cosmic muons. The electronics have aged over the years, and the beam energies have steadily increased with each run period. To correct for these effects, the timing for each scintillator must be calibrated at the beginning of each run period. In addition to the electronics, the cables and wires, the photo-multiplier tubes (PMT) and the plastic scintillators have also aged and degraded, so a check of the efficiency loss is also done.

A.2 Barrel and Endcap Counters

A detailed description can be found in [55]. The barrel system consists of 30 plastic scintillator paddles with a length of 2.9 m and a thickness of 1 cm. Each counter end is connected by a light-guide to a PMT. The barrel counters reside between the barrel part of BGO and HCAL (Figure A.1). In the *r-z* plane the counters follow the shape of the HCAL. The counters have a radial distance from the beam axis of 885 mm for $|z| < 800$ mm and 979 mm for $|z| < 1000$mm. The polar angle coverage of the barrel counters is $34° < \theta < 146°$ ($|\cos\theta| < 0.83$). In the $r - \phi$ plane, the barrel counters are

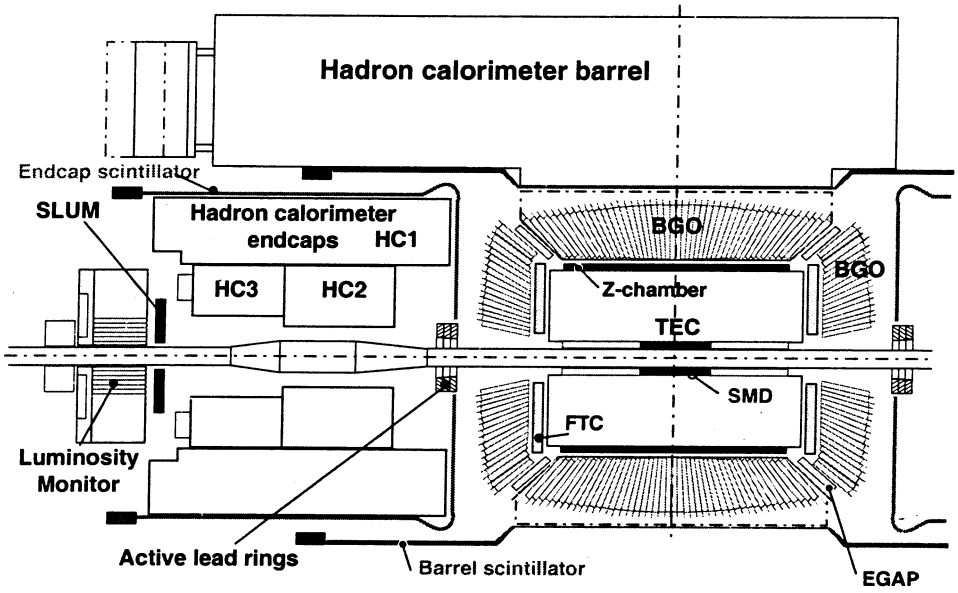

Figure A.1: A perspective view of the L3 detector with the relative position of the L3 scintillator system. The barrel counters reside between the BGO and the HCAL. Only one of the endcaps is fully shown.

grouped in pairs. They follow the 16-fold symmetry of the HCAL. Due to the horizontal support rails for the BGO, two counters, 17 and 32, are missing. The adjacent counters, 18 and 31, are about 50% larger in order to minimize the acceptance loss.

The endcap system consists of 16 counters located between the BGO and HCAL endcaps on either side of the interaction point. Each counter is made out of 3 plates of 5 mm thick plastic scintillator. The light of each plate is collected by 10 wavelength shifting fibers. A total of 30 fibers from the counter end into an optical connector. A flexible light guide connects the counters to the PMTs, which are situated outside the HCAL. The endcap PMTs are the only part of the L3 scintillator system readily accessible on-site. The counters have an inner (outer) radius of 230 (768) mm. They are screwed

against the outer shielding of the BGO endcaps. The middle of the second scintillator plate is at a distance of z = ±1132.5 mm from the interaction point. The polar angle coverage is $11.5° < \theta < 34.1°$ ($0.83 < |\cos\theta| < 0.98$).

A.3 Event Selection

Only two track events are used for the calibration and efficiency study. These events are mostly Bhabhas and di-muons with back-to-back tracks. The tracks must be energetic enough to completely pass through the BGO in order to make a scintillator hit. The selection of events paralleled my thesis analysis which used both the TEC and the BGO. Both tracks of the event were required to have:

- 5 or more hits in the TEC. This is very loose cut to allow for low angle tracks. A track with less than five hits has an unreliable momentum measurement and may be mismatched.
- The distance of closest approach of the track to the collision point in the r-ϕ plane must be less than 2 mm. This cut rejects cosmic muons.
- The charged particle should deposit at least 100 MeV in the BGO.
- |p| > 300 MeV. There should be enough energy in order to penetrate the BGO and fire the scintillator.
- $|\Delta\phi^{\text{TEC-BGO}}_{\text{matched}}| < 50$ mrad. The matching of the TEC track to the BGO cluster should be less than 50 mrad in the azimuthal angle, ϕ.

A.4 Barrel Calibration

The TDC records counts, N_{TDC}, which is translated to a time, t_{TDC}, by the following equation:

$$t_{TDC} = -C_{Conv}(N_{TDC} - N^0_{TDC}). \quad \text{(A.1)}$$

The count-to-time conversion constant C_{Conv} and the TDC offset N^0_{TDC} are channel dependent calibration constants. Both constants may differ significantly for the different TDC channels. The calibration procedure takes advantage of the multibunchlet mode of LEP. There are two bunchlets per beam crossing at $\sqrt{s} = 91$ GeV. Instead of a single equation (Eq. A.1), the TDC-to-time translation can be expressed for each bunchlet:

$$t^{(1)}_{TDC} = -C_{Conv}(N^{(1)}_{TDC} - N^0_{TDC}). \quad \text{(A.2)}$$

$$t^{(2)}_{TDC} = -C_{Conv}(N^{(2)}_{TDC} - N^0_{TDC}). \quad \text{(A.3)}$$

where the superscripts (1) and (2) refer to bunchlet 1 and bunchlet 2 for a given counter.

Assuming the calibration constants have been determined, the time can be calculated from the TDC counts according to Eqs. A.2 and A.3. A significant improvement to the timing resolution can be achieved by correcting for the ADC pulse-height dependence, which is referred to as the time-slew effect:

$$t_{CTR} = t_{TDC} + \delta t_{slew}. \quad \text{(A.4)}$$

The time-slew correction which depends on the recorded pulse-height, A, is well described by

$$\delta t_{slew} = a(\tfrac{A_0}{A-b} - 1) \quad \text{(A.5)}$$

where $a = 1.74$ ns, $A_0 = 1871$ ADC counts and $b = 629$ ADC counts. The TDC has only a single hit capacity, therefore the TDC input signals are

gated. Only hits in a time window of ±30 ns around the expected bunch crossing time are recorded. Signals with large ADC pulse-heights tend to be narrow and fit within the time window, and the time-slew correction will be small. Signals with smaller pulse-heights will be wider and part of the signal will be cut off as the gate closes. This adds an assymmetric tail to the timing resolution, but it can be minimized by the time-slew correction.

The time is measured by the PMTs on both ends of the barrel counters. A mean time is automatically calculated for the different transition times of the light inside the counter:

$$t_{Ctr,mean} = 0.5(t^P_{Ctr} + t^J_{Ctr}). \tag{A.6}$$

The notation is historic, where P and J refer to *PIT* and *JURA*, the positive and negative z side of the interation point.

The method of calibration is done such that $t_{Ctr,mean}$ measured for a muon generated by a beam interaction is equal to the time-of-flight, t_{FL}. The corrected time is defined by

$$t_{Cor} = t_{Ctr,mean} - t_{FL} \tag{A.7}$$

which is distributed around $t_{Cor} = 0$ ns. The width of the distribution is the time resolution of the counters. The corrected time is calculated automatically during event reconstruction for both bunchlet 1 and 2.

The purpose of the calibration is to center the mean of the corrected time distribution at zero. The process is iterative. At the beginning of a new run period, the L3 reconstruction package uses the calibration constants, C_{Conv} and N^0_{TDC}, from the previous run period. For each consecutive run

period since 1996, LEP has risen in center-of-mass energy from 130 GeV to 189 GeV in 1998. The method of calibration requires timing information from two bunchlets for each counter, but the two bunchlet mode is run only at $\sqrt{s} = 91$ GeV. There is only one bunchlet per beam crossing at higher energies. Fortunately, there is a Z calibration data run session before each high energy run begins, but, at best, there is no more than 2.5 pb^{-1} of luminosity available for calibration. This sets a statistical limit on the timing resolution for the second bunchlet. Using the calibration constants from the previous run period, the corrected time distributions are made for both bunchlets for each of the 30 barrel counters. Any offsets from a mean of zero are recorded. The corrected time offsets in combination with the measured TDC counts, $N_{TDC}^{(i)}$ (where i refers to bunchlet 1 or 2), are used to determine a new set of calibration constants. Two or three iterations may be necessary as typically the first iteration will over-correct.

Only the scintillator hits which are matched to a track in the TEC and to a cluster in the BGO are used for the calibration. There is no information stored for the azimuthal angle of the scintillator hit; only the counter number is known. Therefore, it is necessary to convert the ϕ of the BGO cluster to a "counter number":

$$CTR_{BGO,barrel} = \phi \, \frac{57.2958}{11.25} \; + \; 1. \qquad \text{(A.8)}$$

The BGO "counter number" should remain a real number, not an integer. The scintillator hit is matched to the BGO cluster. There may be several scintillator hits for each two track event. Only the scintillator hit with the smallest counter number difference is associated with a track:

$$\Delta\ CTR = |CTR_{BGO} - CTR_{SCINT}|. \qquad \text{(A.9)}$$

Only scintillator hits that match to the BGO cluster within ΔCTR < 1.5 are used for the calibration. In addition the BGO cluster must be in the barrel region, $|\cos\theta| < 0.83$.

The corrected time distribution is fitted to a Gaussian. There is always an observed time shift, but it is considered neglible for anything less than 100 ps because the current time resolution for the barrel scintillator counters is about 900 ps. A Gaussian fit is performed for both bunchlet 1 and 2 for each counter. The mean value of the Gaussian is taken as the observed time shift. A typical example of the corrected time distribution for a barrel counter for both bunchlets is shown in Figure A.2. The average time resolution measured for bunchlet 1 was about 950 ps. Bunchlet 2 is slightly better at 820 ps (Figure A.3).

A.5 Endcap Calibration

The time reconstruction for the endcap counters is done according to Eqs. A.2 and A.3. However, no time-slew correction is applied. Also, there is only one PMT for each counter, so there is no mean time calculation. The BGO cluster to which a scintillator hit is matched must be in the fiducial volume $|\cos\theta| > 0.83$. The choice of using the TEC to select two track events, in particular tracks with at least five hits, has the effect of neglecting scintillator hits at very small angles ($|\cos\theta| > 0.92$) although the BGO endcaps extend to $|\cos\theta| = 0.98$. This choice was considered reasonable because most physics events would be reconstructed to tracks and momentum measurements made by the TEC.

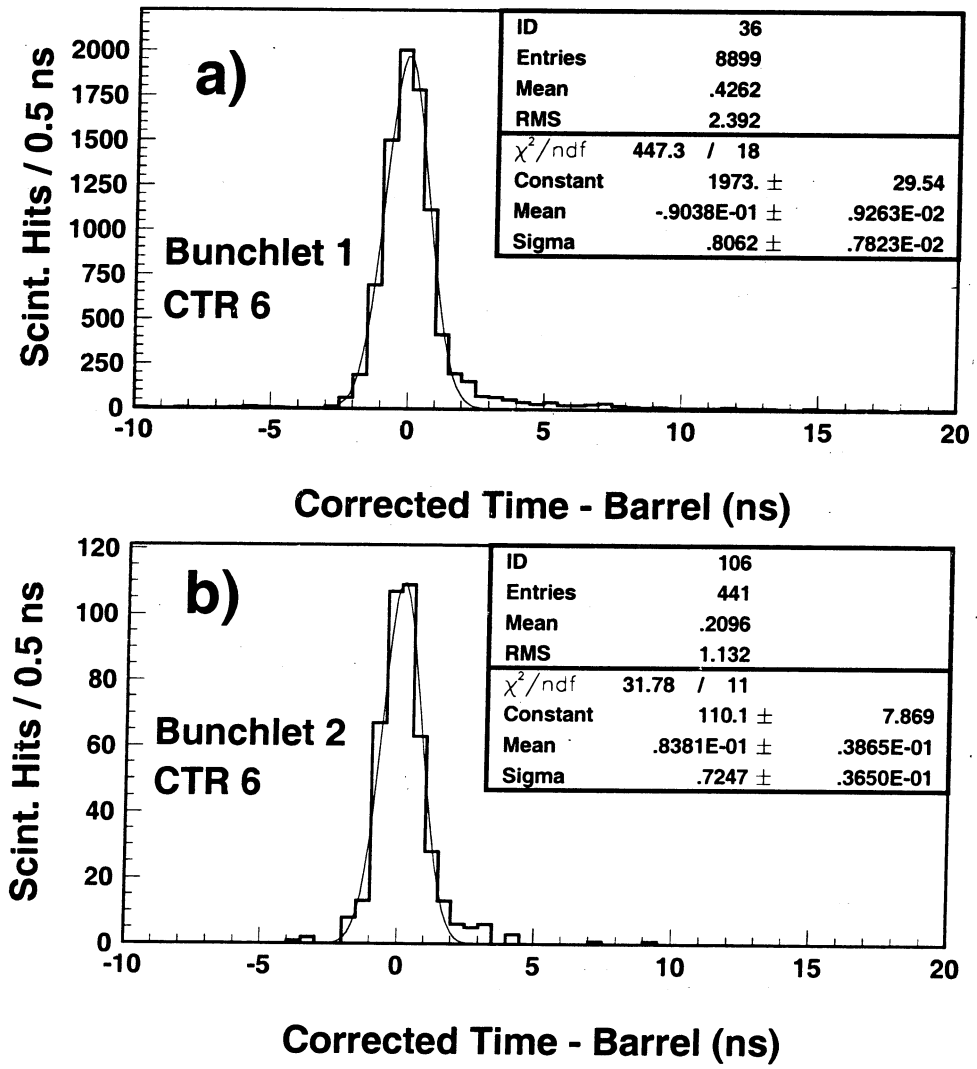

Figure A.2: The corrected time resolution for barrel counter 6 for (a) bunchlet 1 and (b) bunchlet 2 for the 1998 data period.

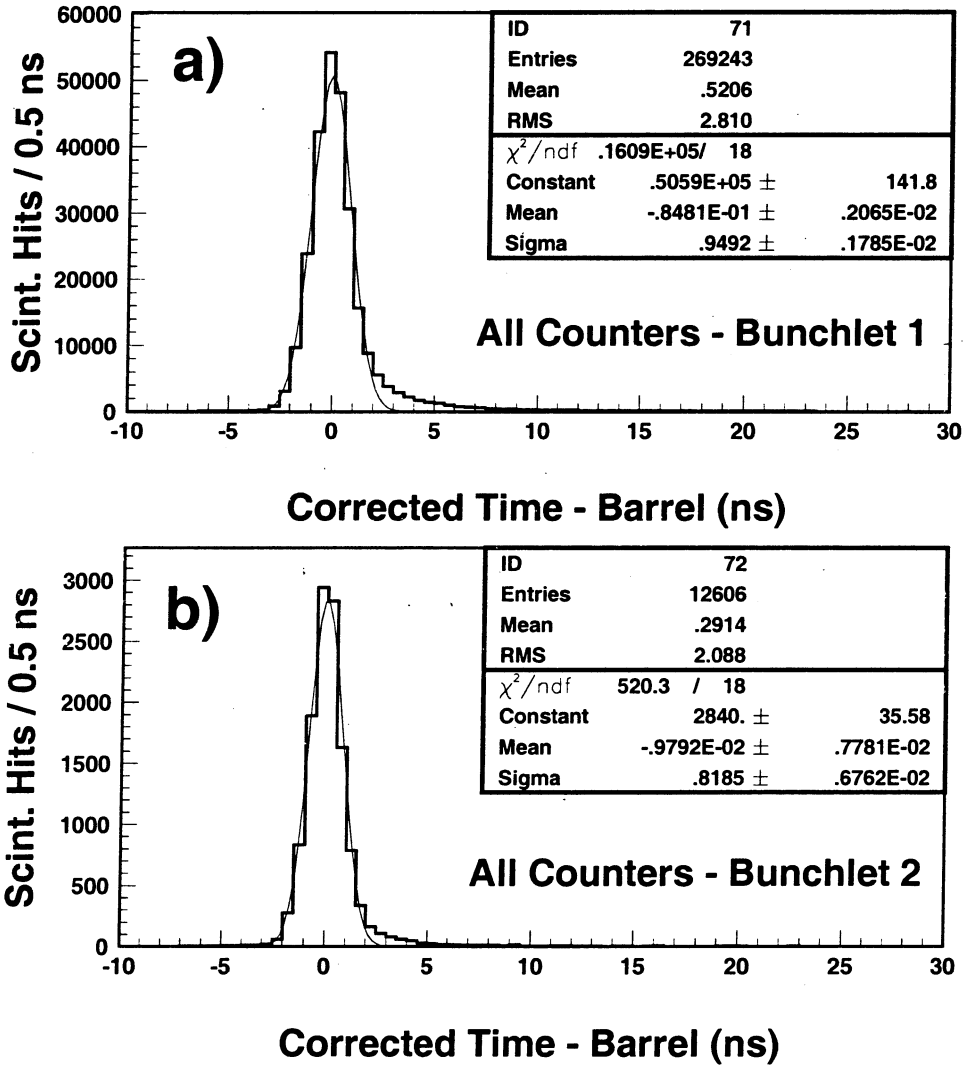

Figure A.3: Average corrected time resolution in the barrel counters for (a) bunchlet 1 and (b) bunchlet 2 for 1998 data period. Both figures represent the average of all 30 barrel counters after the calibration was performed. About 45 pb^{-1} (30%) of the full 1998 data set was used to make these figures, but only the first 2.5 pb^{-1} of data contributes to bunchlet 2.

The corrected time distributions for the endcap counters are not as clean as for the barrel, largely due to a lack of a time-slew correction. A significant tail falls off of the Gaussian distribution. Therefore, the distribution is fitted to a convolution of a Gaussian plus an exponential decay. A typical example of the corrected time distribution for an endcap counter for both bunchlets is shown in Figure A.4. The sum of parameters P1 and P2 is taken as the observed time shift. The available statistics is about a factor of two smaller than for the barrel calibration; for bunchlet 2 the statistical uncertainty can be significant. Any shifts less than 300 ps are considered negligible as the average time resolution for the endcap counters is about 2 ns (Figure A.5).

A.6 Efficiency

The data sample needs to be refined to keep only the particles that should have penetrated through the BGO into the HCAL. There are cracks between the scintillator counters, which line up with similar cracks between the HCAL sectors. Some inefficiency is actually due to this acceptance loss, but this may be partially corrected by requiring some minimum energy in the HCAL. Looking for muons in the muon chambers can be too restrictive. The following cuts are made:

- $|p| > 1.0$ GeV. There should be enough momentum so that a minimum ionizing particle (MIP) will penetrate through the BGO.

- $E_{bump} < 500$ MeV. A MIP should deposit an average of 250-300 MeV in the BGO. This cut also rejects the electrons which almost never penetrate the BGO.

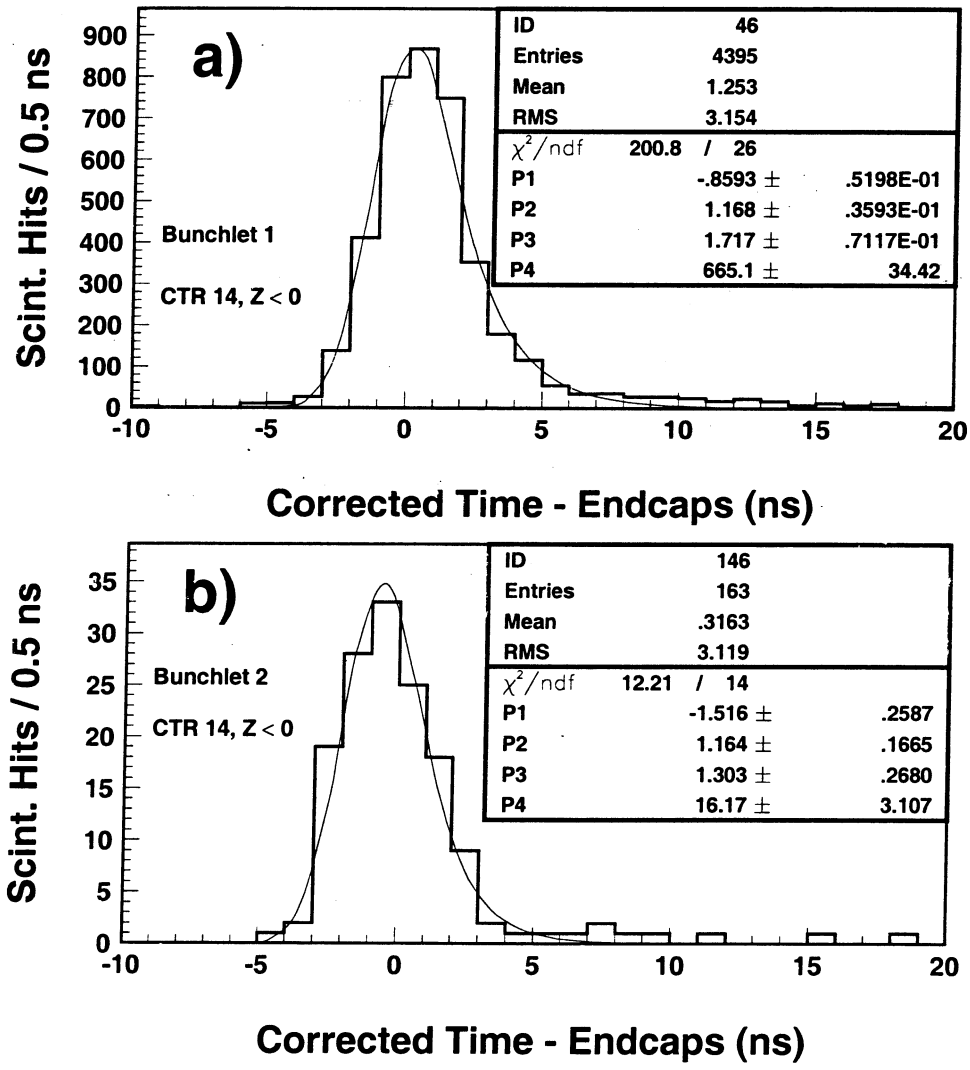

Figure A.4: The corrected time resolution for endcap counter 14 (Jura side) for (a) bunchlet 1 and (b) bunchlet 2 for the 1998 data period.

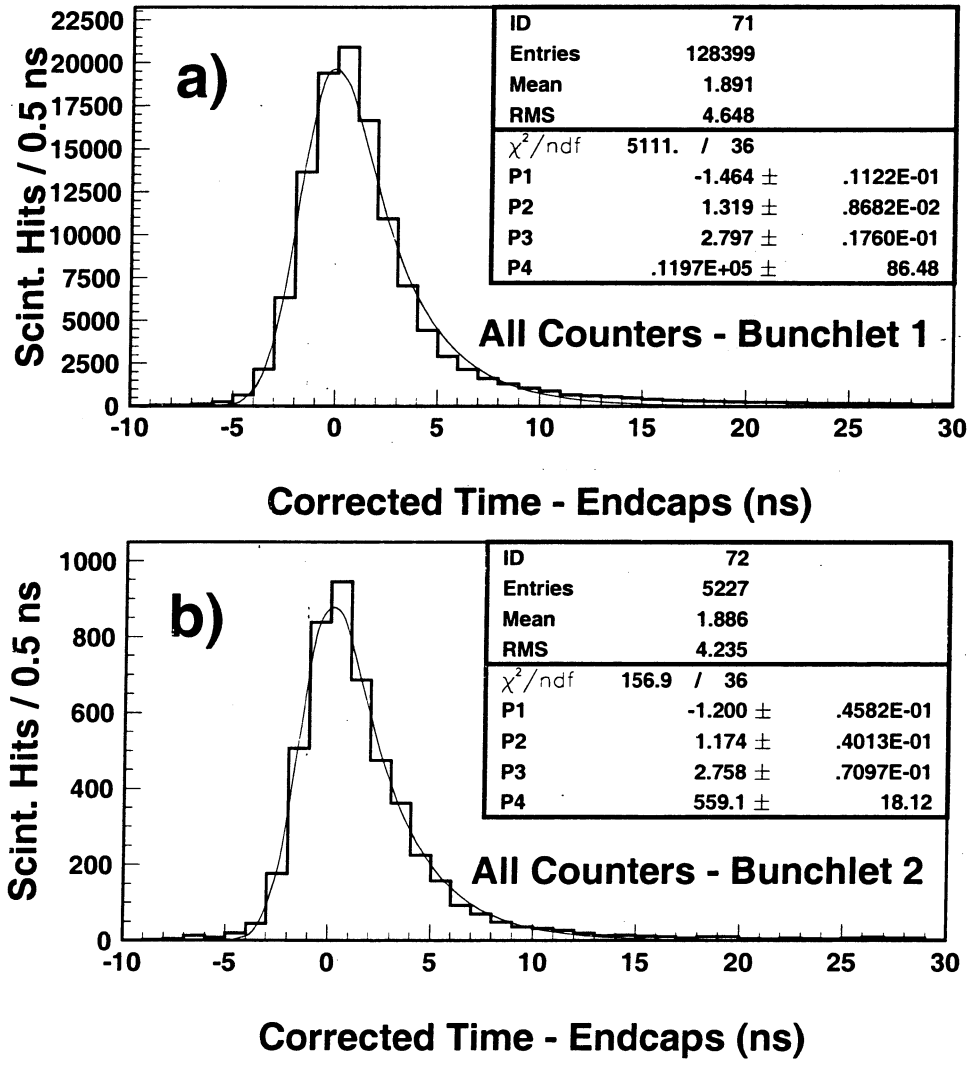

Figure A.5: Average corrected time resolution in the endcap counters for (a) bunchlet 1 and (b) bunchlet 2 for 1998 data period. Both figures represent the average of all 32 endcap counters after the calibration was performed. About 45 pb^{-1} (30%) of the full 1998 data set was used to make these figures, but only the first 2.5 pb^{-1} of data contributes to bunchlet 2.

- $E_{hcal} > 100$ MeV. The energy within a 7° cone about the particle deposited in the HCAL should be sufficient to exclude noise. Also, some energy needs to be detected to correct for some acceptance loss due to cracks between the counters.

The counter efficiency is the ratio of the number of hits detected in the counter to the number of clusters in the BGO. This is done counter by counter.

An average efficiency in the barrel was determined to be about 90% with a statistical error of 2.5% (Figure A.6). This does not include a correction for the acceptance loss due to the small cracks between the barrel scintillators. The exceptions are counters 24 and 25. In 1991, there was a leak of the BGO cooling liquid. The sillicon oil crept between the counter wrapping and the plastic scintillator, modifying the reflection index of the surface. A study of the efficiencies for counters 24 and 25 was done for the data period of 1995-98. There is a steady decrease in efficiency loss for counter 25, falling to about 55% in 1998 (Figure A.7). Counter 24 appears to be slightly more stable through 1997 at about 60%, and in fact increased slightly to about 65% in 1998 probably due to an increase in the high voltage. A similar study of the adjacent counters 23 and 26 was done, and both counters remained stable over the same period (Figure A.8). The efficiency loss is evident in the time resolution distribuions. In Figure A.9, the corrected time distributions for the barrel counters 23 and 24 are shown.

The endcap counters were not installed until 1995, so their performance is quite good. The average counter efficiency for tracks with momentum greater

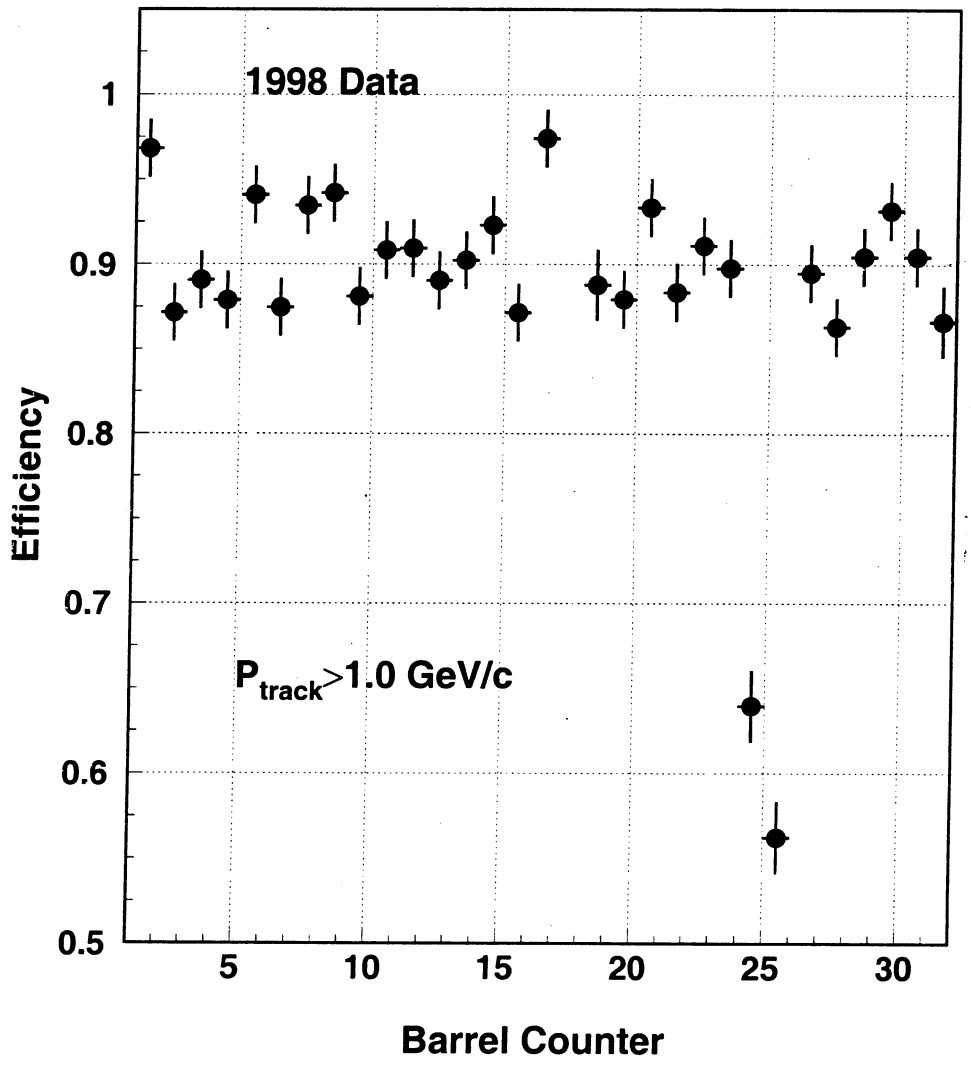

Figure A.6: Barrel counter efficiency for 1998 data.

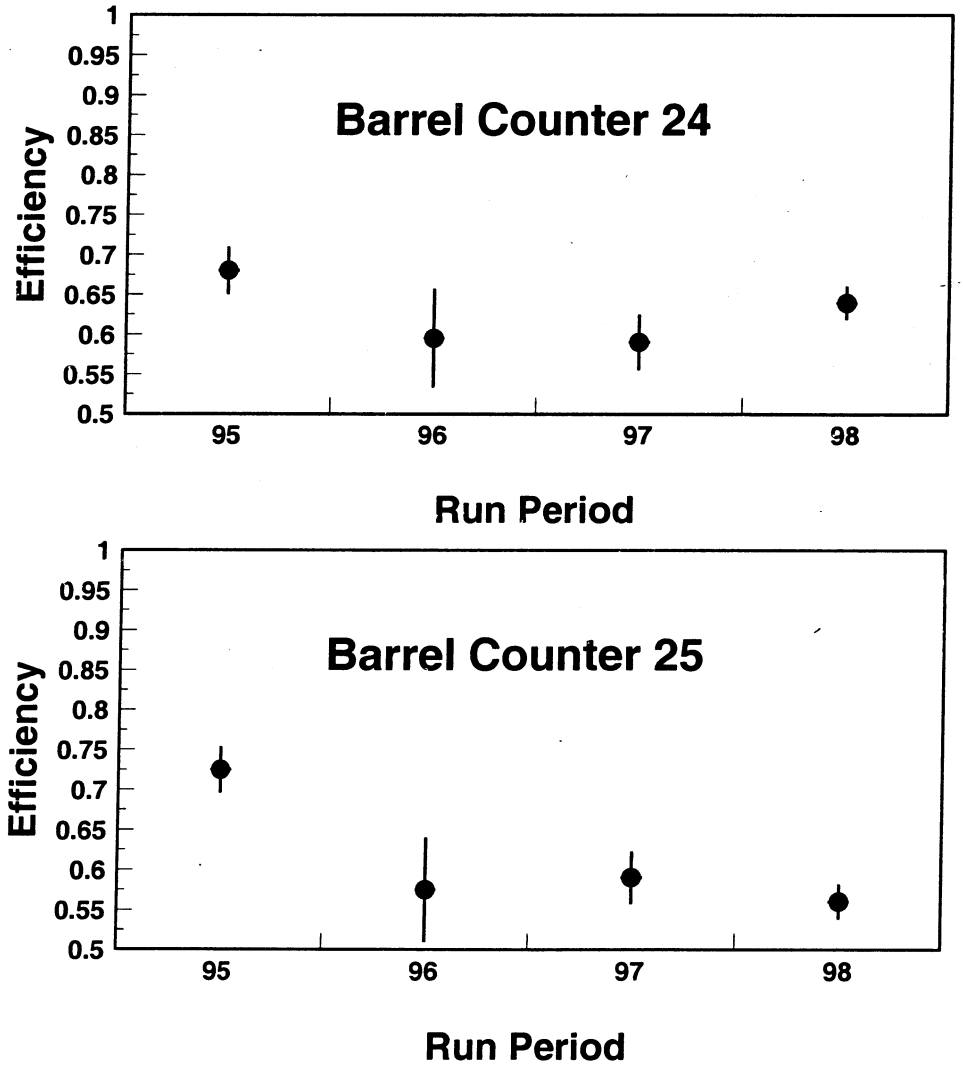

Figure A.7: Efficiency of barrel counters 24 and 25 from 1995 through 1998.

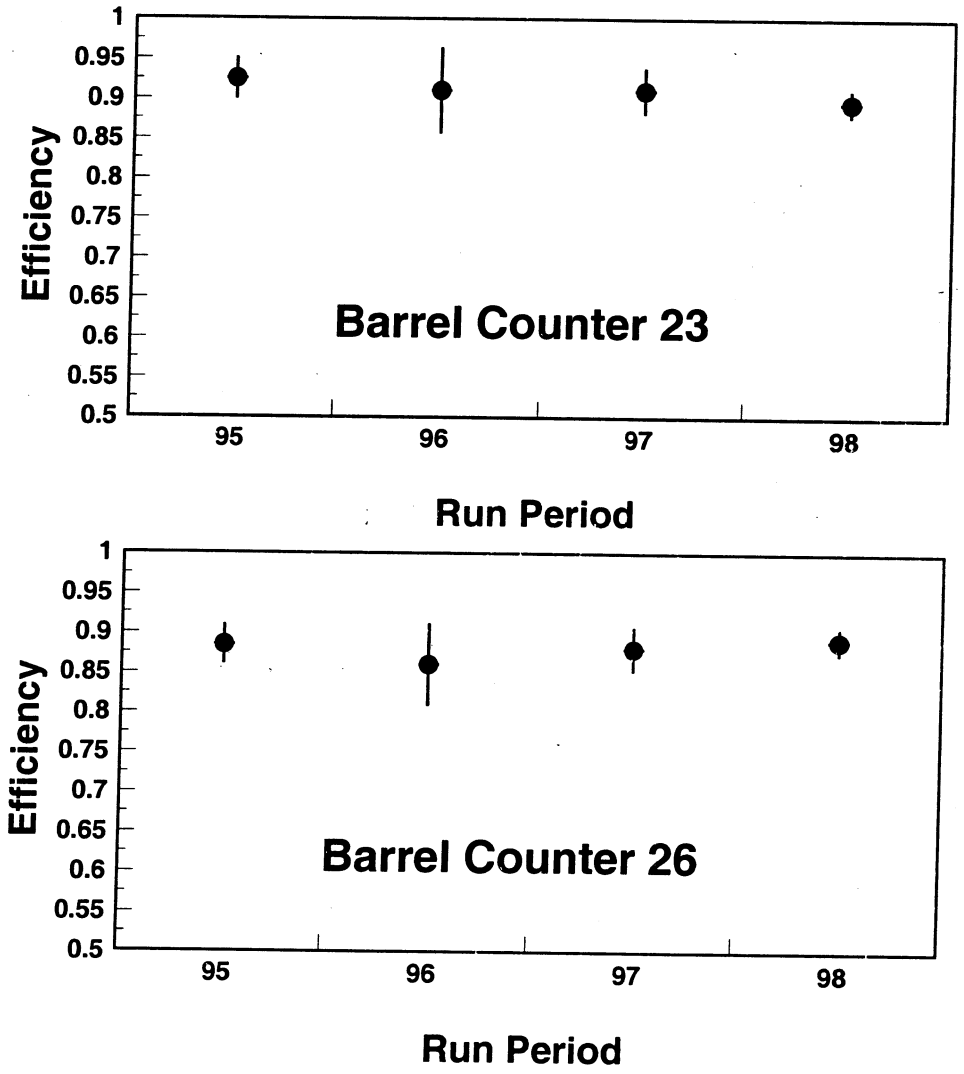

Figure A.8: Efficiency of barrel counters 23 and 26 from 1995 through 1998.

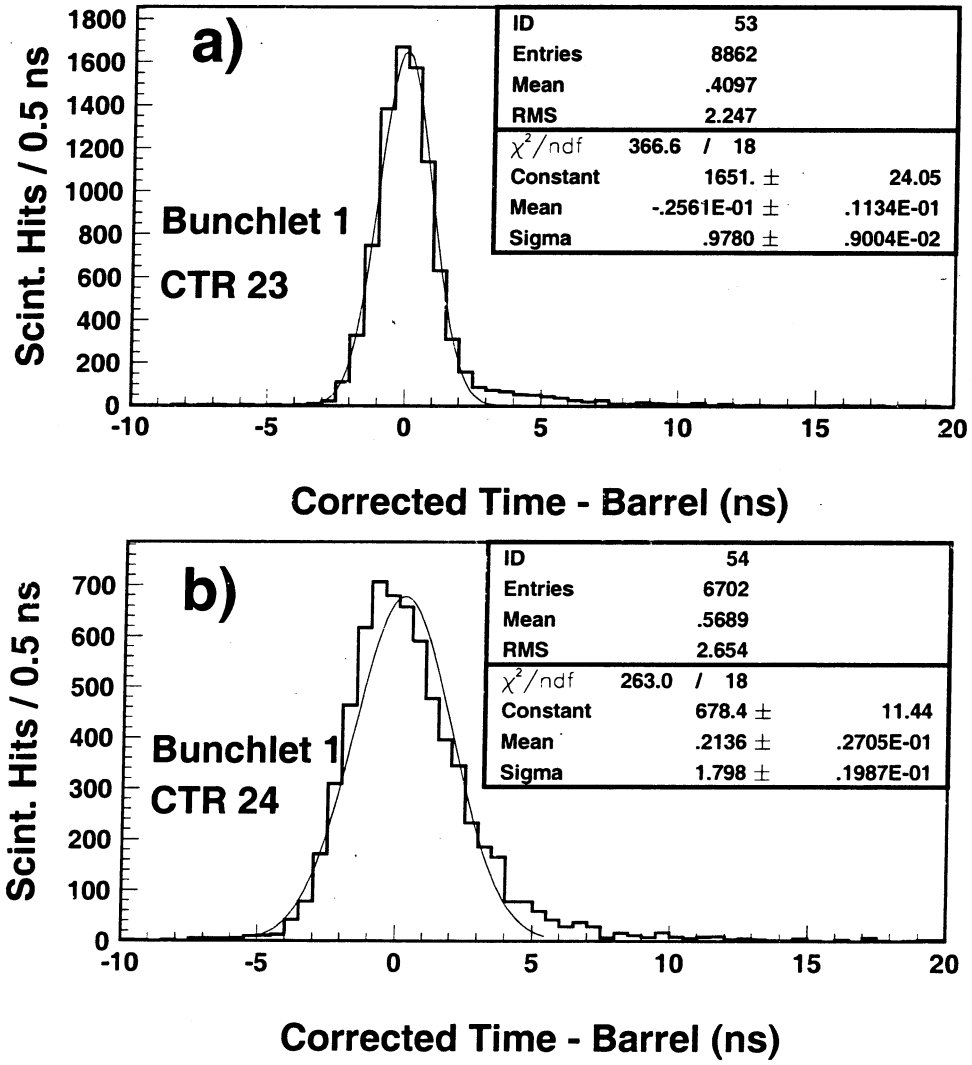

Figure A.9: Corrected time distributions for (a) barrel counter 23 and (b) barrel counter 24.

than 1 GeV is greater than 95%. In the plot of the endcap counter efficiency, the horizontal scale ranges from 1 to 32 (Figure A.10). Counters 1 through 16 correspond to the positive z-axis (Pit) of the detector, and counters 17 through 32 correspond to the negative z-axis (Jura). The efficiencies for counters 12, 13, 28 and 29 are underestimated because a small fraction of those counters is missing in order to fit around the BGO support structure.

A.7 Acknowlegdements

I would like to thank Stephan Wynhoff whose patience was above and beyond the call of duty. Much of the procedure for the scintillator calibration was passed on to me from him. Additional assistance was provided by Christoph Paus and Martin von der Mey.

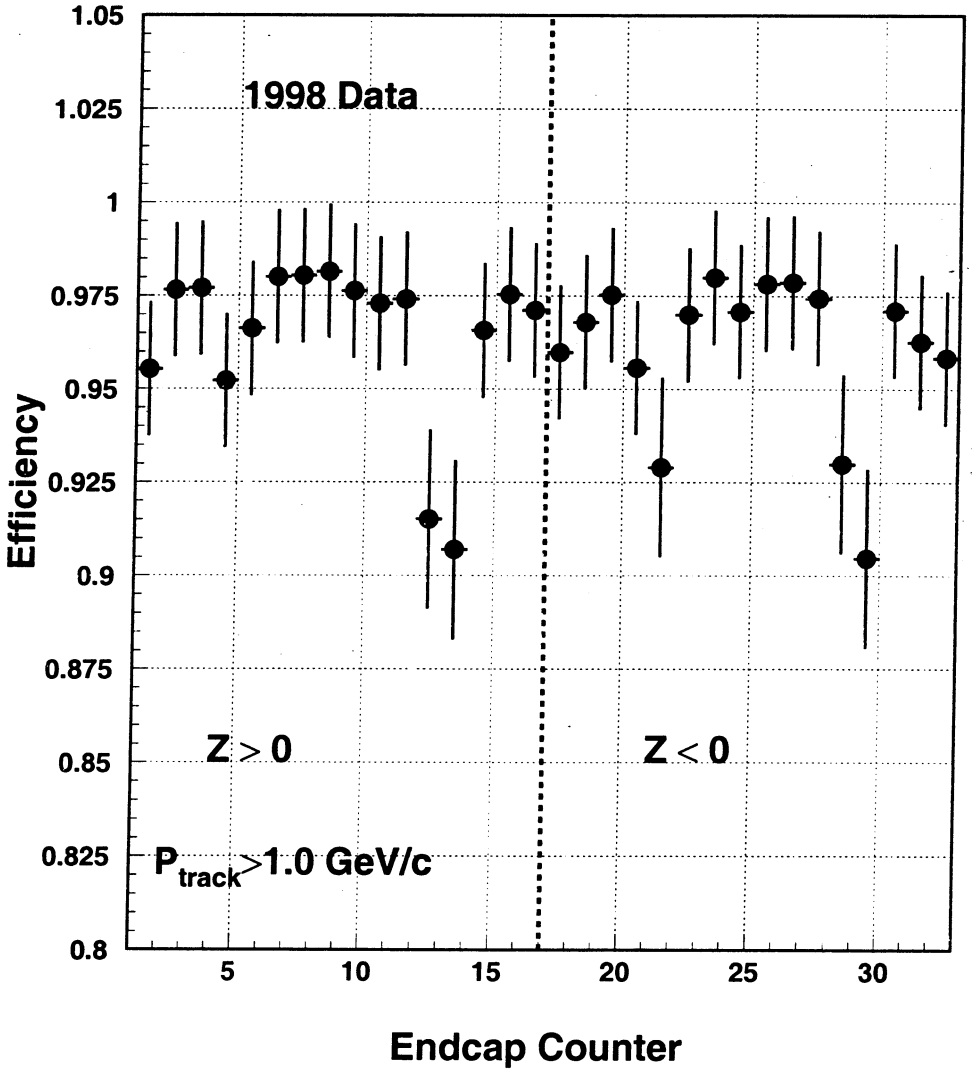

Figure A.10 Endcap counter efficiency for 1998 data.

THE L3 COLLABORATION

M.Acciarri[26], P.Achard[18], O.Adriani[15], M.Aguilar-Benitez[25],
J.Alcaraz[25], G.Alemanni[21], J.Allaby[16], A.Aloisio[28],
M.G.Alviggi[28], G.Ambrosi[18], H.Anderhub[47], V.P.Andreev[6,36],
T.Angelescu[12], F.Anselmo[9], A.Arefiev[27], T.Azemoon[3],
T.Aziz[10], P.Bagnaia[35], L.Baksay[42], A.Balandras[4],
R.C.Ball[3], S.Banerjee[10], Sw.Banerjee[10], K.Banicz[44],
A.Barczyk[47,45], R.Barillère[16], L.Barone[35], P.Bartalini[21],
M.Basile[9], R.Battiston[32], A.Bay[21], F.Becattini[15],
U.Becker[14], F.Behner[47], J.Berdugo[25], P.Berges[14],
B.Bertucci[32], B.L.Betev[47], S.Bhattacharya[10], M.Biasini[32],
A.Biland[47], J.J.Blaising[4], S.C.Blyth[33], G.J.Bobbink[2],
R.Bock[1], A.Böhm[1], L.Boldizsar[13], B.Borgia[16,35],
D.Bourilkov[47], M.Bourquin[18], S.Braccini[18], J.G.Branson[38],
V.Brigljevic[47], F.Brochu[4], A.Buffini[15], A.Buijs[43],
J.D.Burger[14], W.J.Burger[32], J.Busenitz[42], A.Button[3],
X.D.Cai[14], M.Campanelli[47], M.Capell[14], G.Cara Romeo[9],
G.Carlino[28], A.M.Cartacci[15], J.Casaus[25], G.Castellini[15],
F.Cavallari[35], N.Cavallo[28], C.Cecchi[18], M.Cerrada[25],
F.Cesaroni[22], M.Chamizo[25], Y.H.Chang[49], U.K.Chaturvedi[17],
M.Chemarin[24], A.Chen[49], G.Chen[7], G.M.Chen[7],
H.F.Chen[19], H.S.Chen[19], X.Chereau[4], G.Chiefari[28],
L.Cifarelli[37], F.Cindolo[9], C.Civinini[15], I.Clare[14],

R.Clare[14], G.Coignet[4], A.P.Colijn[2], N.Colino[25],
S.Costantini[8], F.Cotorobai[12], B.de la Cruz[25], A.Csilling[13],
T.S.Dai[14], J.A.van Dalen[30], R.D'Alessandro[15], R.de Asmundis[28],
P.Deglon[18], A.Degré[4], K.Deiters[45], D.della Volpe[28],
P.Denes[34], F.DeNotaristefani[35], A.De Salvo[47], M.Diemoz[35],
D.van Dierendonck[2], F.Di Lodovico[47], C.Dionisi[16,35], M.Dittmar[47],
A.Dominguez[38], A.Doria[28], M.T.Dova[17], D.Duchesneau[4],
D.Dufournand[4], P.Duinker[2], I.Duran[39], H.El Mamouni[24],
A.Engler[33], F.J.Eppling[14], F.C.Erné[2], P.Extermann[18],
M.Fabre[45], R.Faccini[35], M.A.Falagan[25], S.Falciano[35],
A.Favara[15], J.Fay[24], O.Fedin[36], M.Felcini[47],
T.Ferguson[33], F.Ferroni[35], H.Fesefeldt[1], E.Fiandrini[32],
J.H.Field[18], F.Filthaut[16], P.H.Fisher[14], I.Fisk[38],
G.Forconi[14], L.Fredj[18], K.Freudenreich[47], C.Furetta[26],
Yu.Galaktionov[27,14], S.N.Ganguli[10], P.Garcia-Abia[5], M.Gataullin[31],
S.S.Gau[11], S.Gentile[35], N.Gheordanescu[12], S.Giagu[35],
S.Goldfarb[21], Z.F.Gong[19], M.W.Gruenewald[8], R.van Gulik[2],
V.K.Gupta[34], A.Gurtu[10], L.J.Gutay[44], D.Haas[5],
B.Hartmann[1], A.Hasan[29], D.Hatzifotiadou[9], T.Hebbeker[8],
A.Hervé[16], P.Hidas[13], J.Hirschfelder[33], H.Hofer[47],
G. Holzner[47], H.Hoorani[33], S.R.Hou[49], I.Iashvili[46],
B.N.Jin[7], L.W.Jones[3], P.de Jong[16], I.Josa-Mutuberría[25],
R.A.Khan[17], D.Kamrad[46], J.S.Kapustinsky[23], M.Kaur[17],
M.N.Kienzle-Focacci[18], D.Kim[35], D.H.Kim[41], J.K.Kim[41],

S.C.Kim[41], W.W.Kinnison[23], J.Kirkby[16], D.Kiss[13],
W.Kittel[30], A.Klimentov[14,27], A.C.König[30], A.Kopp[46],
I.Korolko[27], V.Koutsenko[14,27], R.W.Kraemer[33], W.Krenz[1],
A.Kunin[14,27], P.Lacentre[46], P.Ladron de Guevara[25], I.Laktineh[24],
G.Landi[15], C.Lapoint[14], K.Lassila-Perini[47], P.Laurikainen[20],
A.Lavorato[37], M.Lebeau[16], A.Lebedev[14], P.Lebrun[24],
P.Lecomte[47], P.Lecoq[16], P.Le Coultre[47], H.J.Lee[8],
J.M.Le Goff[16], R.Leiste[46], E.Leonardi[35], P.Levtchenko[36],
C.Li[19], C.H.Lin[49], W.T.Lin[49], F.L.Linde[2,16],
L.Lista[28], Z.A.Liu[7], W.Lohmann[46], E.Longo[35],
Y.S.Lu[7], K.Lübelsmeyer[1], C.Luci[16,35], D.Luckey[14],
L.Luminari[35], W.Lustermann[47], W.G.Ma[19], M.Maity[10],
G.Majumder[10], L.Malgeri[16], A.Malinin[27], C.Maña[25],
D.Mangeol[30], P.Marchesini[47], G.Marian[42], J.P.Martin[24],
F.Marzano[35], G.G.G.Massaro[2], K.Mazumdar[10], R.R.McNeil[6],
S.Mele[16], L.Merola[28], M.Meschini[15], W.J.Metzger[30],
M.von der Mey[1], D.Migani[9], A.Mihul[12], H.Milcent[16],
G.Mirabelli[35], J.Mnich[16], P.Molnar[8], B.Monteleoni[15],
T.Moulik[10], G.S.Muanza[24], F.Muheim[18], A.J.M.Muijs[2],
S.Nahn[14], M.Napolitano[28], F.Nessi-Tedaldi[47], H.Newman[31],
T.Niessen[1], A.Nippe[21], A.Nisati[35], H.Nowak[46],
Y.D.Oh[41], G.Organtini[35], R.Ostonen[20], C.Palomares[25],
D.Pandoulas[1], S.Paoletti[35,16], P.Paolucci[28], H.K.Park[33],
I.H.Park[41], G.Pascale[35], G.Passaleva[16], S.Patricelli[28],

T.Paul[11], M.Pauluzzi[32], C.Paus[16], F.Pauss[47],
D.Peach[16], M.Pedace[35], Y.J.Pei[1], S.Pensotti[26],
D.Perret-Gallix[4], B.Petersen[30], S.Petrak[8], D.Piccolo[28],
M.Pieri[15], P.A.Piroué[34], E.Pistolesi[26], V.Plyaskin[27],
M.Pohl[47], V.Pojidaev[27,15], H.Postema[14], J.Pothier[16],
N.Produit[18], D.Prokofiev[36], J.Quartieri[37], G.Rahal-Callot[47],
N.Raja[10], P.G.Rancoita[26], G.Raven[38], P.Razis[29],
D.Ren[47], M.Rescigno[35], S.Reucroft[11], T.van Rhee[43],
S.Riemann[46], K.Riles[3], A.Robohm[47], J.Rodin[42],
B.P.Roe[3], L.Romero[25], S.Rosier-Lees[4], S.Roth[1],
J.A.Rubio[16], D.Ruschmeier[8], H.Rykaczewski[47], S.Sakar[35],
J.Salicio[16], E.Sanchez[25], M.P.Sanders[30], M.E.Sarakinos[20],
C.Schäfer[1], V.Schegelsky[36], S.Schmidt-Kaerst[1], D.Schmitz[1],
N.Scholz[47], H.Schopper[48], D.J.Schotanus[30], J.Schwenke[1],
G.Schwering[1], C.Sciacca[28], D.Sciarrino[18], L.Servoli[32],
S.Shevchenko[31], N.Shivarov[40], V.Shoutko[27], J.Shukla[23],
E.Shumilov[27], A.Shvorob[31], T.Siedenburg[1], D.Son[41],
B.Smith[33], P.Spillantini[15], M.Steuer[14], D.P.Stickland[34],
A.Stone[6], H.Stone[34], B.Stoyanov[40], A.Straessner[1],
K.Sudhakar[10], G.Sultanov[17], L.Z.Sun[19], H.Suter[47],
J.D.Swain[17], Z.Szillasi[42], X.W.Tang[7], L.Tauscher[5],
L.Taylor[11], C.Timmermans[30], Samuel C.C.Ting[14], S.M.Ting[14],
S.C.Tonwar[10], J.Tóth[13], C.Tully[34], K.L.Tung[7],
Y.Uchida[14], J.Ulbricht[47], E.Valente[35], G.Vesztergombi[13],

I.Vetlitsky[27], G.Viertel[47], S.Villa[11], M.Vivargent[4],
S.Vlachos[5], H.Vogel[33], H.Vogt[46], I.Vorobiev[16,27],
A.A.Vorobyov[36], A.Vorvolakos[29], M.Wadhwa[5], W.Wallraff[1],
J.C.Wang[14], X.L.Wang[19], Z.M.Wang[19], A.Weber[1],
H.Wilkens[30], S.X.Wu[14], S.Wynhoff[1], L.Xia[31],
Z.Z.Xu[19], B.Z.Yang[19], C.G.Yang[7], H.J.Yang[7],
M.Yang[7], J.B.Ye[19], S.C.Yeh[19], J.M.You[50],
An.Zalite[36], Yu.Zalite[36], P.Zemp[47], Y.Zeng[1],
Z.P.Zhang[19], G.Y.Zhu[7], R.Y.Zhu[31], A.Zichichi[9,16,17],
F.Ziegler[46], G.Zilizi[42]

1. I. Physikalisches Institut, RWTH, D-52056 Aachen, FRG
III. Physikalisches Institut, RWTH, D-52056 Aachen, FRG

2. National Institute for High Energy Physics, NIKHEF, and University of Amsterdam, NL-1009 DB Amsterdam, The Netherlands

3. University of Michigan, Ann Arbor, MI 48109, USA

4. Laboratoire d'Annecy-le-Vieux de Physique des Particules, LAPP, IN2P3-CNRS, BP 110, F-74941 Annecy-le-Vieux CEDEX, France

5. Institute of Physics, University of Basel, CH-4056 Basel, Switzerland

6. Louisiana State University, Baton Rouge, LA 70803, USA

7. Institute of High Energy Physics, IHEP, 100039 Beijing, China

8. Humboldt University, D-10099 Berlin, FRG

9. University of Bologna and INFN-Sezione di Bologna, I-40126 Bologna, Italy

10. Tata Institute of Fundamental Research, Bombay 400 005, India

11. Northeastern University, Boston, MA 02115, USA

12. Institute of Atomic Physics and University of Bucharest, R-76900 Bucharest, Romania

13. Central Research Institute for Physics of the Hungarian Academy of Sciences, H-1525 Budapest 114, Hungary

14. Massachusetts Institute of Technology, Cambridge, MA 02139, USA

15. INFN Sezione di Firenze and University of Florence, I-50125 Florence, Italy

16. European Laboratory for Particle Physics, CERN, CH-1211 Geneva 23, Switzerland

17. World Laboratory, FBLJA Project, CH-1211 Geneva 23, Switzerland

18. University of Geneva, CH-1211 Geneva 4, Switzerland

19. Chinese University of Science and Technology, USTC, Hefei, Anhui 230 029, China

20. SEFT, Research Institute for High Energy Physics, P.O. Box 9, SF-00014 Helsinki, Finland

21. University of Lausanne, CH-1015 Lausanne, Switzerland

22. INFN-Sezione di Lecce and Universitá Degli Studi di Lecce, I-73100 Lecce, Italy

23. Los Alamos National Laboratory, Los Alamos, NM 87544, USA

24. Institut de Physique Nucléaire de Lyon, IN2P3-CNRS,Université Claude Bernard, F-69622 Villeurbanne, France

25. Centro de Investigaciones Energéticas, Medioambientales y Tecnologícas, CIEMAT, E-28040 Madrid, Spain

26. INFN-Sezione di Milano, I-20133 Milan, Italy

27. Institute of Theoretical and Experimental Physics, ITEP, Moscow, Russia

28. INFN-Sezione di Napoli and University of Naples, I-80125 Naples, Italy

29. Department of Natural Sciences, University of Cyprus, Nicosia, Cyprus

30. University of Nijmegen and NIKHEF, NL-6525 ED Nijmegen, The Netherlands

31. California Institute of Technology, Pasadena, CA 91125, USA

32. INFN-Sezione di Perugia and Universitá Degli Studi di Perugia, I-06100 Perugia, Italy

33. Carnegie Mellon University, Pittsburgh, PA 15213, USA

34. Princeton University, Princeton, NJ 08544, USA

35. INFN-Sezione di Roma and University of Rome, "La Sapienza", I-00185 Rome, Italy

36. Nuclear Physics Institute, St. Petersburg, Russia

37. University and INFN, Salerno, I-84100 Salerno, Italy

38. University of California, San Diego, CA 92093, USA

39. Dept. de Fisica de Particulas Elementales, Univ. de Santiago, E-15706 Santiago de Compostela, Spain

40. Bulgarian Academy of Sciences, Central Lab. of Mechatronics and Instrumentation, BU-1113 Sofia, Bulgaria

41. Center for High Energy Physics, Adv. Inst. of Sciences and Technology, 305-701 Taejon, Republic of Korea

42. University of Alabama, Tuscaloosa, AL 35486, USA

43. Utrecht University and NIKHEF, NL-3584 CB Utrecht, The Netherlands

44. Purdue University, West Lafayette, IN 47907, USA

45. Paul Scherrer Institut, PSI, CH-5232 Villigen, Switzerland

46. DESY-Institut für Hochenergiephysik, D-15738 Zeuthen, FRG

47. Eidgenössische Technische Hochschule, ETH Zürich, CH-8093 Zürich, Switzerland

48. University of Hamburg, D-22761 Hamburg, FRG

49. National Central University, Chung-Li, Taiwan, China

50. Department of Physics, National Tsing Hua University, Taiwan, China

PUBLICATIONS

1. *Production of e, μ and τ Pairs in Untagged Two-Photon Collisions at LEP.*

   L3 Collab., M. Acciarri *et al.* Physics Letters B **407** (1997) 341.

2. *Inclusive J/Ψ and χ_c Production in Hadronic Z Decays.*

   L3 Collab., M. Acciarri *et al.* Physics Letters B **407** (1997) 351.

3. *QCD Studies and Determination of α_s in e^+e^- Collisions at $\sqrt{s}$ = 161 GeV and 172 GeV.*

   L3 Collab., M. Acciarri *et al.* Physics Letters B **404** (1997) 390.

4. *Cross Section of Hadron Production in $\gamma\gamma$ Collisions at LEP.*

   L3 Collab., M. Acciarri *et al.* Physics Letters B **408** (1997) 450.

5. *Measurement of Hadron and Lepton-Pair Production at 161 GeV $< \sqrt{s} <$ 172 GeV at LEP.*

   L3 Collab., M. Acciarri *et al.* Physics Letters B **407** (1997) 361.

6. *Search for Anomalous Four-Jet Events in e^+e^- Annihilation at $\sqrt{s}$ = 130-172 GeV.*

   L3 Collab., M. Acciarri *et al.* Physics Letters B **411** (1997) 330.

7. *Measurement of W-Pair Cross Sections in e^+e^- Interactions at $\sqrt{s}$ = 172 GeV and W-Decay Branching Fractions.*

   L3 Collab., M. Acciarri *et al.* Physics Letters B **407** (1997) 419.

8. *Search for Heavy Neutral and Charged Leptons in* e^+e^- *Annihilation at* $\sqrt{s}$ *= 161 and* $\sqrt{s}$ *= 172 GeV.*

   L3 Collab., M. Acciarri *et al.* Physics Letters B **412** (1997) 189.

9. *Single and Multi-Photon Events with Missing Energy in* e^+e^- *Collisions at 161 GeV <* $\sqrt{s}$ *< 172 GeV.*

   L3 Collab., M. Acciarri *et al.* Physics Letters B **415** (1997) 299.

10. *Hard-Photon Production at* $\sqrt{s}$ *= 161 GeV and 172 GeV at LEP.*

    L3 Collab., M. Acciarri *et al.* Physics Letters B **413** (1997) 159.

11. *Search for the Standard Model Higgs Boson in* e^+e^- *Interactions at 161 GeV <* $\sqrt{s}$ *< 172 GeV.*

    L3 Collab., M. Acciarri *et al.* Physics Letters B **411** (1997) 373.

12. *Measurements of Mass, Width and Gauge Couplings of the W Boson at LEP.*

    L3 Collab., M. Acciarri *et al.* Physics Letters B **413** (1997) 176.

13. *Search for R-Parity Breaking Sneutrino Exchange at LEP.*

    L3 Collab., M. Acciarri *et al.* Physics Letters B **414** (1997) 373.

14. *Neutral-Current Four-Fermion Production in* e^+e^- *Interactions at 130 GeV* $\leq \sqrt{s} \leq$ *172 GeV.*

    L3 Collab., M. Acciarri *et al.* Physics Letters B **413** (1997) 191.

15. *Search for Scalar Leptons, Charginos and Neutralinos* e^+e^- *Collisions at* $\sqrt{s}$ *= 161 - 172 GeV.*

L3 Collab., M. Acciarri *et al.* European Physics Journal C **4** (1997) 207.

16. *Search for New Physics Phenomena in Fermion-Pair Production at LEP.*
L3 Collab., M. Acciarri *et al.* Physics Letters B **433** (1998) 163.

17. *Search for the Standard Model Higgs Boson in* e^+e^- *Interactions at* $\sqrt{s}$ *= 183 GeV.*
L3 Collab., M. Acciarri *et al.* Physics Letters B **431** (1998) 437.

18. *Search for Neutral Higgs Bosons of the Minimal Supersymmetric Standard Model in* e^+e^- *Interactions at* $\sqrt{s}$ *= 130-183 GeV.*
L3 Collab., M. Acciarri *et al.* Physics Letters B **436** (1998) 389.

19. *Study of Anomalous* $ZZ\gamma$ *and* $Z\gamma\gamma$ *Couplings at LEP.*
L3 Collab., M. Acciarri *et al.* Physics Letters B **436** (1998) 187.

20. *Production of Single W Bosons in* e^+e^- *Interactions at* $130\ GeV \leq \sqrt{s} \leq 183\ GeV$ *and Limits on Anomalous* $WW\gamma$ *Couplings.*
L3 Collab., M. Acciarri *et al.* Physics Letters B **436** (1998) 417.

21. *Measurement of Radiative Bhabha and Quasi-Real Compton Scattering.*
L3 Collab., M. Acciarri *et al.* Physics Letters B **439** (1998) 183.

22. *Measurement of W-Pair Cross Sections in* e^+e^- *Interactions at* $\sqrt{s}$ *= 183 GeV and W-Decay Branching Fractions.*
L3 Collab., M. Acciarri *et al.* Physics Letters B **436** (1998) 437.

23. *Searches for Scalar Top and Scalar Bottom Quarks in* e^+e^- *Interactions at 161 GeV* $\leq \sqrt{s} \leq$ *183 GeV.*

L3 Collab., M. Acciarri *et al.* Physics Letters B **445** (1998) 428.

24. *QCD Results from Studies of Hadronic Events Produced in* e^+e^- *Annihilations at* $\sqrt{s}$ = *183 GeV.*

L3 Collab., M. Acciarri *et al.* Physics Letters B **444** (1998) 569.

25. *Search for Charged Higgs Bosons in* e^+e^- *Collisions at Centre-of-Mass Energies between 130 and 183 GeV.*

L3 Collab., M. Acciarri *et al.* Physics Letters B **446** (1999) 368.

26. *Single and Multi-Photon Events with Missing Energy in* e^+e^- *Collisions at* $\sqrt{s}$ = *183 GeV.*

L3 Collab., M. Acciarri *et al.* Physics Letters B **444** (1998) 503.

27. *Measurement of the* $e^+e^- \rightarrow Z \rightarrow b\bar{b}$ *Forward-Backward Asymmetry and the* $B^0\bar{B}^0$ *Mixing Parameter Using Prompt Leptons.*

L3 Collab., M. Acciarri *et al.* Physics Letters B **448** (1999) 152.

28. *The* Q^2 *Evolution of the Hadronic Photon Structure Function* F_2^γ *at LEP.*

L3 Collab., M. Acciarri *et al.* Physics Letters B **447** (1999) 147.

29. *Study of Neutral-Current Four-Fermion and ZZ Production in* e^+e^- *Collisions at* $\sqrt{s}$ = *183 GeV.*

L3 Collab., M. Acciarri *et al.* Physics Letters B **450** (1999) 281.

30. χ_{c2} *Formation in Two-Photon Collisions at LEP.*

L3 Collab., M. Acciarri *et al.* Physics Letters B **453** (1999) 73.

31. *Inclusive Charm Production in Two-Photon Collisions at LEP.*

L3 Collab., M. Acciarri *et al.* Physics Letters B **453** (1999) 83.

32. *Heavy Quarkonium Production in* Z *Decays.*

L3 Collab., M. Acciarri *et al.* Physics Letters B **453** (1999) 94.

33. *Measurement of the Cross-Section for the Process* $\gamma^*\gamma^* \rightarrow$ hadrons *at LEP.*

L3 Collab., M. Acciarri *et al.* Physics Letters B **453** (1999) 333.

34. *Measurement of Mass and Width of the* W *Boson at LEP.*

L3 Collab., M. Acciarri *et al.* Physics Letters B **454** (1999) 386.

35. *Search for Scalar Leptons in* e^+e^- *collisions at* $\sqrt{s} = 183$ *GeV.*

L3 Collab., M. Acciarri *et al.* Physics Letters B **456** (1999) 283.

36. *Search for R-parity Violating Chargino and Neutralino Decays in* e^+e^- *Collisions up to* $\sqrt{s} = 183$ *GeV.*

L3 Collab., M. Acciarri *et al.* Accepted by Physics Letters B .

37. *Measurement of an Elongation of the Pion Source in* Z *Decays.*

L3 Collab., M. Acciarri *et al.* Accepted by Physics Letters B .

38. *Formation of the* η_c *in Two-Photon Collisions at LEP.*

L3 Collab., M. Acciarri *et al.* Submitted to Physics Letters B .

39. *Search for Heavy Neutral and Charged Leptons in* e^+e^- *Annihilation at* $\sqrt{s}$ *= 183 and 189 GeV.*

L3 Collab., M. Acciarri *et al.* Submitted to Physics Letters B .

40. *Search for the Standard Model Higgs Boson in* e^+e^- *Interactions at* $\sqrt{s}$ *= 189 GeV.*

L3 Collab., M. Acciarri *et al.* Submitted to Physics Letters B .

41. *Search for Heavy Isosinglet Neutrinos in* e^+e^- *Annihilation at* $130 < \sqrt{s} < 189$ *GeV.*

L3 Collab., M. Acciarri *et al.* Submitted to Physics Letters B .

VITA

Alan L. Stone Jr. was born on August 27th, 1970 in Claridon, Ohio, a small town thirty miles from Cleveland. After graduating from high school, Alan left for Boston to attend college at Boston University. Taking a break from math and physics for a year in 1990-91, he studied French in Grenoble, France, where he met his future wife, Isabel. Alan graduated from Boston University in 1993, receiving a bachelor of arts in physics and astronomy with a minor in French.

In June, 1993, Alan began graduate school at Louisiana State University to study physics. He joined the L3 collaboration in the fall of 1996 working under the guidance of Prof. Roger McNeil and Dr. Valery Andreev. Alan moved to Geneva, Switzerland, for two years in order to work onsite at the European Center for Nuclear and Particle Physics (CERN). In the summer of 1999, Alan was awarded the degree of doctor of philosophy in physics.